December 1992   THESIS~~XXXXXXXXXXX~~

Evolution of Area-Averaged Vertical Velocity in the Convective Region of a Midlatitude Squall Line

Dennis A. Hobson, Captain

AFIT Student Attending: Texas A & M University   AFIT/CI/CIA-92-122

AFIt/CI
Wright-Patterson AFB OH 45433-6583

DTIC
ELECTE
S B D
JUN 0 4 1993

93-12508

||||||||||||||||||||||

93 6 00 019

131

EVOLUTION OF AREA-AVERAGED VERTICAL VELOCITY
IN THE CONVECTIVE REGION OF A MIDLATITUDE SQUALL LINE

A Thesis

by

DENNIS ALLEN HOBSON

Submitted to the Office of Graduate Studies of
Texas A&M University
in partial fulfillment of the requirements for the degree of

MASTER OF SCIENCE

December 1992

Major Subject: Meteorology

EVOLUTION OF AREA-AVERAGED VERTICAL VELOCITY

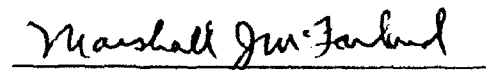# IN THE CONVECTIVE REGION OF A MIDLATITUDE SQUALL LINE

A Thesis

by

DENNIS ALLEN HOBSON

Approved as to style and content by:

Michael I. Biggerstaff
Michael I. Biggerstaff
(Chair of Committee)

Edward J. Zipser
Edward J. Zipser
(Member)

Marshall J. McFarland
Marshall J. McFarland
(Member)

Edward J. Zipser
Edward J. Zipser
(Head of Department)

December 1992

ABSTRACT

Evolution of Area-Averaged Vertical Velocity in the Convective Region
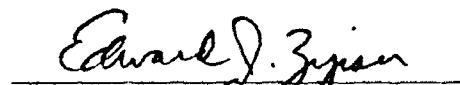
of a Midlatitude Squall Line. (December 1992)

Dennis Allen Hobson, B.S., University of Iowa

Chair of Advisory Committee: Dr. Michael I. Biggerstaff

The evolution of area-averaged vertical velocity over a 50 km length segment of the convective region of the 10 - 11 June 1985 squall line system observed during PRE-STORM (Preliminary Regional Experiment for Stormscale Operational and Research Meteorology - Central Phase) was examined over a period of 43 minutes during the storm's mature stage. Seven dual-Doppler analyses with a temporal resolution of 6 - 10 minutes were used to determine vertical velocity. The vertical velocity was then sampled within the boundaries of an objectively defined convective region; delineated by low and mid-level thresholds of reflectivity and reflectivity gradient. Variations in area-averaged vertical velocity profiles suggested significant mesoscale evolution of the convective region over the period of analysis. This notion was supported by examination of area-averaged reflectivity profiles, and the distribution of vertical velocity magnitudes as a function of height, as well as cross-sections of vertical velocity, reflectivity, and storm-relative flow fields. Comparison of the observed changes in the convective drafts, reflectivity structure, and storm-relative flow, with those of numerical simulations of squall line evolution suggested that the convective region had undergone a rather quick transition from a stronger, developing state to a much weaker, mature state. The developing state was characterized by strong area-averaged upward motion with a high variance in the vertical velocity distributions. The mature state was characterized by much weaker area-averaged ascent and much lower variance in the vertical velocity distribution.

DEDICATION

To my wife Amy, my daughters Erin and Kari, and to my son Matthew. Your support, patience , and encouragement over the past 2 years have made this project possible.

ACKNOWLEDGEMENTS

I would like to express my sincere appreciation to my committee members, Drs. Michael Biggerstaff, Edward Zipser, and Marshall McFarland for their guidance during the course of this thesis and for their thorough reviews of this thesis. Special thanks go to my committee chairman, Dr. Biggerstaff for providing me the opportunity to become involved in his research on mesoscale convective systems, and for all of his help with the various software packages and DM2CM/CM2DM code.

I would also like to thank those persons who made other important contributions to this effort: Mr. Jerry Guynes and Mr. Morey Fazli for their help with various departmental computers; Ms. Sandy Yuter for her help with the DM2CM code; Mr. Tim Thornton for getting RDSS up and running; Ms. Svetla Veleva, Mr. Rusty Billingsly, and Capt. Kevin Mattison for their help in unfolding the raw Doppler-velocity fields; Mr. Robert Barritt for handling changes to the thesis, and to all my fellow graduate students for their companionship and encouragement. Many thanks also to the US Air Force for providing me with the opportunity to participate in the AFIT program and pursue a Masters degree.

Finally, the biggest thanks go to my wife Amy, and my children Erin, Kari, and Matthew, who suffered through and endured the by-products of this effort: my absence from home and my preoccupation with the research.

TABLE OF CONTENTS

LIST OF TABLES

LIST OF FIGURES

CHAPTER I

INTRODUCTION

Squall lines composed of a line of intense convective clouds and an associated region of stratiform precipitation are a mode of mesoscale storm organization frequently observed in midlatitudes as well as the tropics and have been studied for quite some time (e.g., Hamilton and Archibold 1945; Newton 1950; Fujita 1955; Pedgley 1962). Numerous observational studies in the past two decades have greatly expanded our understanding of the general structure and evolution of this important class of mesoscale convective system (MCS) (e.g., Zipser 1969, 1977; Houze 1977; LeMone and Zipser 1980; Ogura and Liou 1980; Zipser and LeMone 1980; Gamache and Houze 1982, 1985; Houze and Rappaport 1984; Heymsfield and Schotz 1985; Smull and Houze 1985, 1987a,b; Leary and Rappaport 1987; Biggerstaff et al. 1988; Biggerstaff and Houze 1991a,b). Based on these earlier studies, a conceptual model of a mature squall line with a trailing region of stratiform precipitation viewed in a vertical cross-section oriented perpendicular to the convective line has been constructed (Fig. 1).

Figure 1 indicates that the general front-to-rear air flow through the storm is found in the low levels near the gust front, extends nearly vertically in the convective region, then slopes more gently rearward into the stratiform region at higher levels. Superimposed on the general air flow within the convective region are strong, localized updrafts and downdrafts associated with the individual intense convective cells (Houze et al. 1989). Also indicated is the layer of air which often enters the storm from the rear of the stratiform region and descends to the rear of the convective line, a portion of which returns toward the rear of the storm in the low-level outflow, and some of which typically flows around the convective towers to augment the gust front.

Various recent numerical modeling studies have also furthered our knowledge of the structure and evolution of this type of MCS (e.g. Thorpe et al. 1982; Fovell and Ogura 1988, 1989; Rotunno et al. 1988; Weisman et al. 1988; Lafore and Moncrieff 1989; Zhang and Gao 1989; Zhang et al. 1989). By manipulating the internal dynamics and microphysical processes of the squall line as well as the characteristics of its environment, these simulations have helped explain and verify much of the observational knowledge about the three-dimensional airflow through these storms. However, explicit knowledge

---

The style is that of the *Monthly Weather Review.*
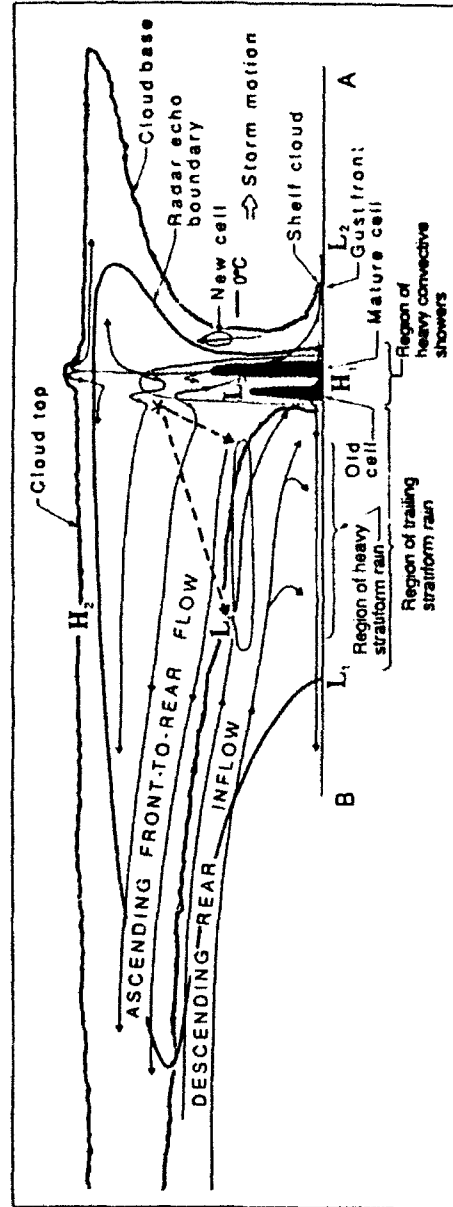
Figure 1. Conceptual model of a squall line with a trailing stratiform area, viewed in a vertical cross-section oriented perpendicular to the convective line (i.e. parallel to its motion). From Houze et al. (1989).

of the vertical motion fields within these storms remains incomplete.

Houze (1989) noted that previous observational studies which showed a "snapshot" of the kinematic structure of the mature stage of squall lines, suggested that area-averaged vertical velocity profiles within the stratiform region agreed fairly well from storm to storm (Fig. 2). However, area-averaged vertical velocity profiles over the convective region of different squall lines demonstrated a high degree of dissimilarity (Fig. 3). It is uncertain whether the mean vertical motion over the convective region of these MCSs is highly variable as a result of physical differences between the convective region from storm to storm, or as a result of the evolution of the convective regions over a meso (~1 hr) time-scale, or as a result of meso-beta scale (~40 km) variability in the basic structure of the convective regions over different parts of each storm. If the mesoscale temporal or spatial variability of the structure of the convective region is important, then a single profile of area-averaged vertical velocity would be unrepresentative of the large-scale character of the convective region.

The degree to which these mean profiles of vertical velocity are representative for the entire convective region has significant impact on diagnostic studies of heat, momentum, moisture, and vorticity that attempt to determine the effect of MCSs on the large-scale environment, as well as the parameterization of convection in mesoscale and regional numerical models (e.g., Hartman et al. 1984). The net heating of the large-scale environment is greatly affected by both the convective and stratiform regions of MCSs. However, variability in net heating estimates appears to be primarily due to variability in the convective region component. Although processes such as melting and radiation are important, the net heating by a storm is dominated by condensation and evaporation associated with vertical air motions (Houze 1989). The intense vertical motions within the convective region thus play a large part in determining the net heating profile of MCSs.

Figure 4 shows component heating profiles derived from an idealized MCS by Houze (1982). A significant portion of the total heating of the large-scale environment by the MCS is done by deep convection (Fig. 5). Although some evidence exists which supports the component heating profiles estimated by Houze (1982), additional study is required to determine the representativeness of vertical velocity profiles within the convective regions of MCSs and to determine what factors may affect these profiles (Houze 1989).

From previous numerical and observational studies of squall line evolution we might expect that the vertical motion profile over the convective region of an individual squall line would exhibit significant variation as the storm progresses through the stages of its lifecycle. For example, Fig. 6 shows vertical cross-sections of radar reflectivity
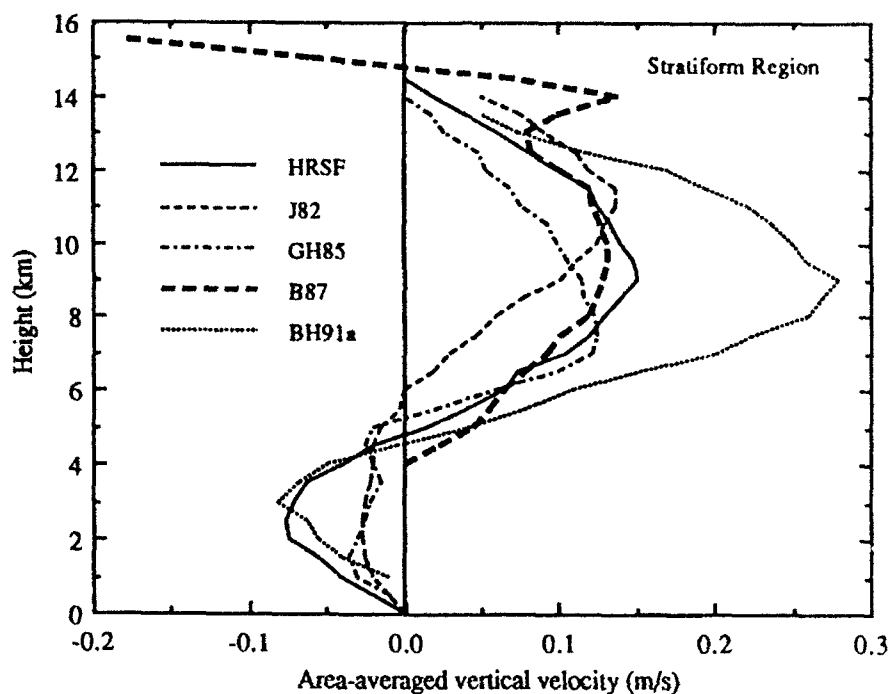
Figure 2. Vertical profiles of area-averaged vertical velocity over the stratiform region of several MCSs. HRSF is from Houze and Rappaport (1984), J82 from Johnson (1982), GH85 from Gamache and Houze (1985), B87 from Balsley et al. (1988), and BH91a from Biggerstaff and Houze (1991a). Adapted from Houze (1989) and Biggerstaff and Houze (1991a).
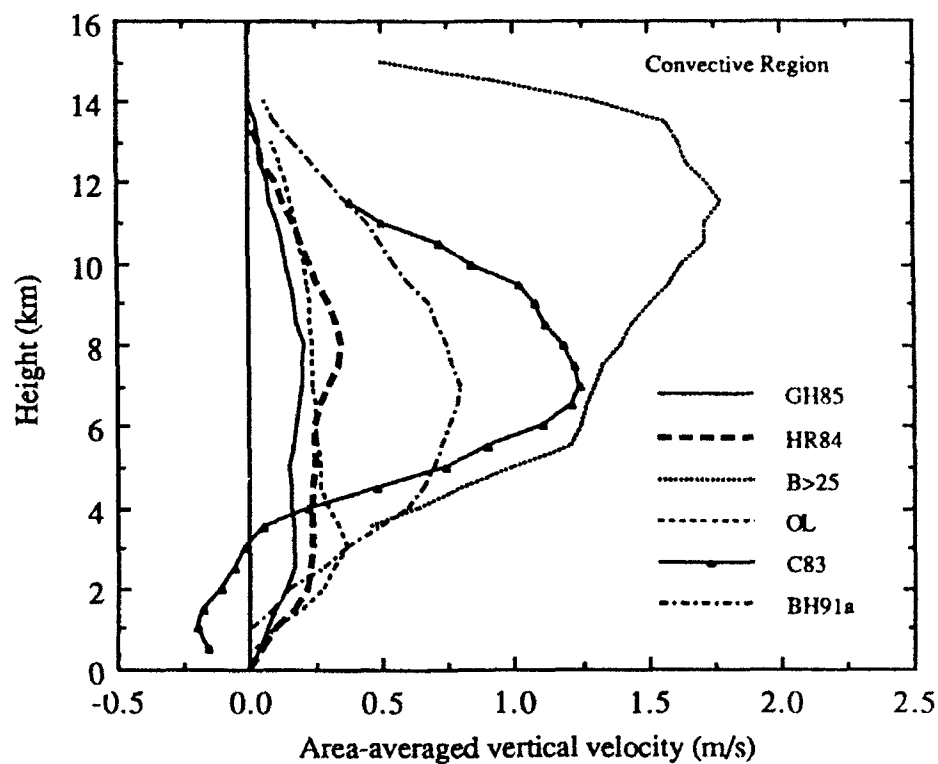
Figure 3. Vertical profiles of area-averaged vertical velocity over the convective region of several MCSs. GH85 is from Gamache and Houze (1985), HR84 from Houze and Rappaport (1984), B>25 from Balsley et al. (1988), OL from Ogura and Liou (1980), C83 from Chong (1983), and BH91a from Biggerstaff and Houze (1991a). Adapted from Houze (1989) and Biggerstaff and Houze (1991a).
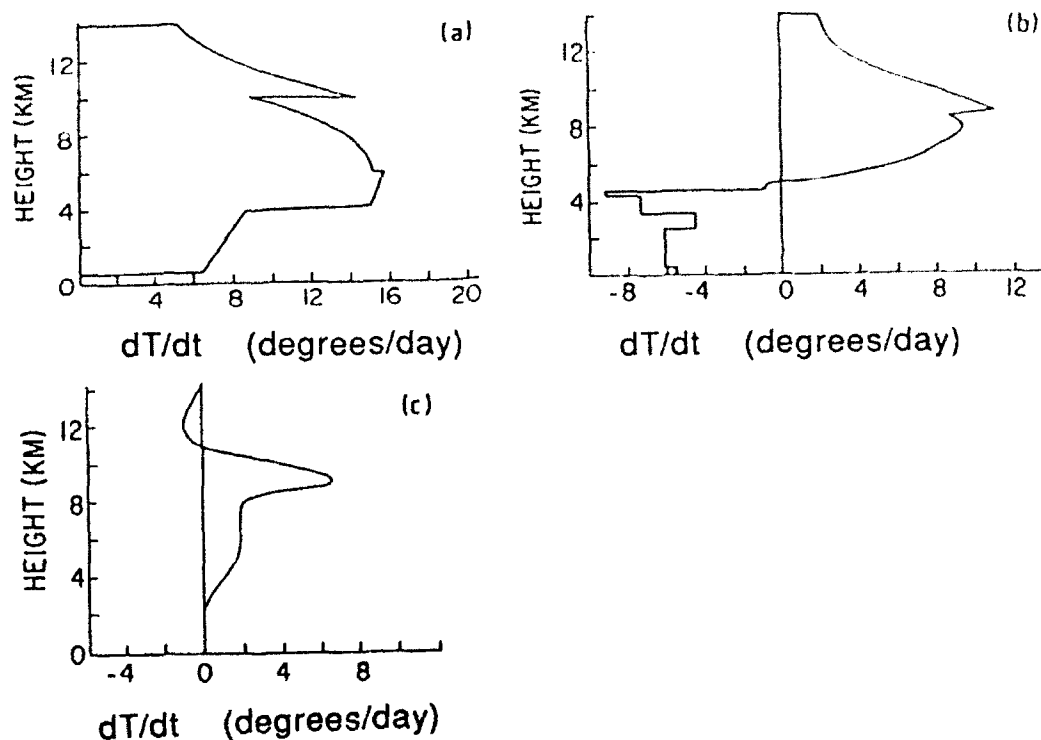
Figure 4. Component vertical heating profiles of an arbitrary large-scale area by an idealized cloud cluster: (a) by deep convection, (b) by non-radiative processes in the stratiform region, (c) by radiative processes. From Houze (1982).
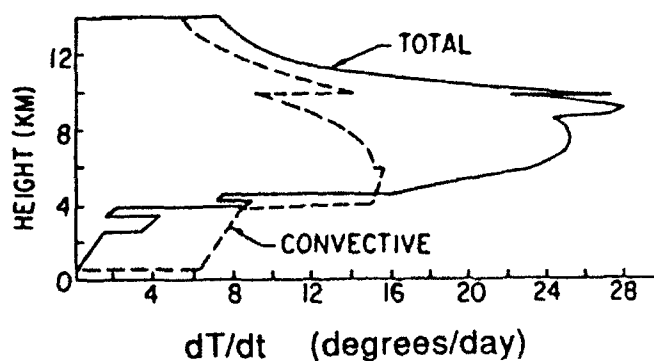
Figure 5. Total vertical heating profile of an arbitrary large-scale area by an idealized cloud cluster. The component due to deep convection alone (from Fig. 4a) is shown as a dashed curve for comparison. From Houze (1982).
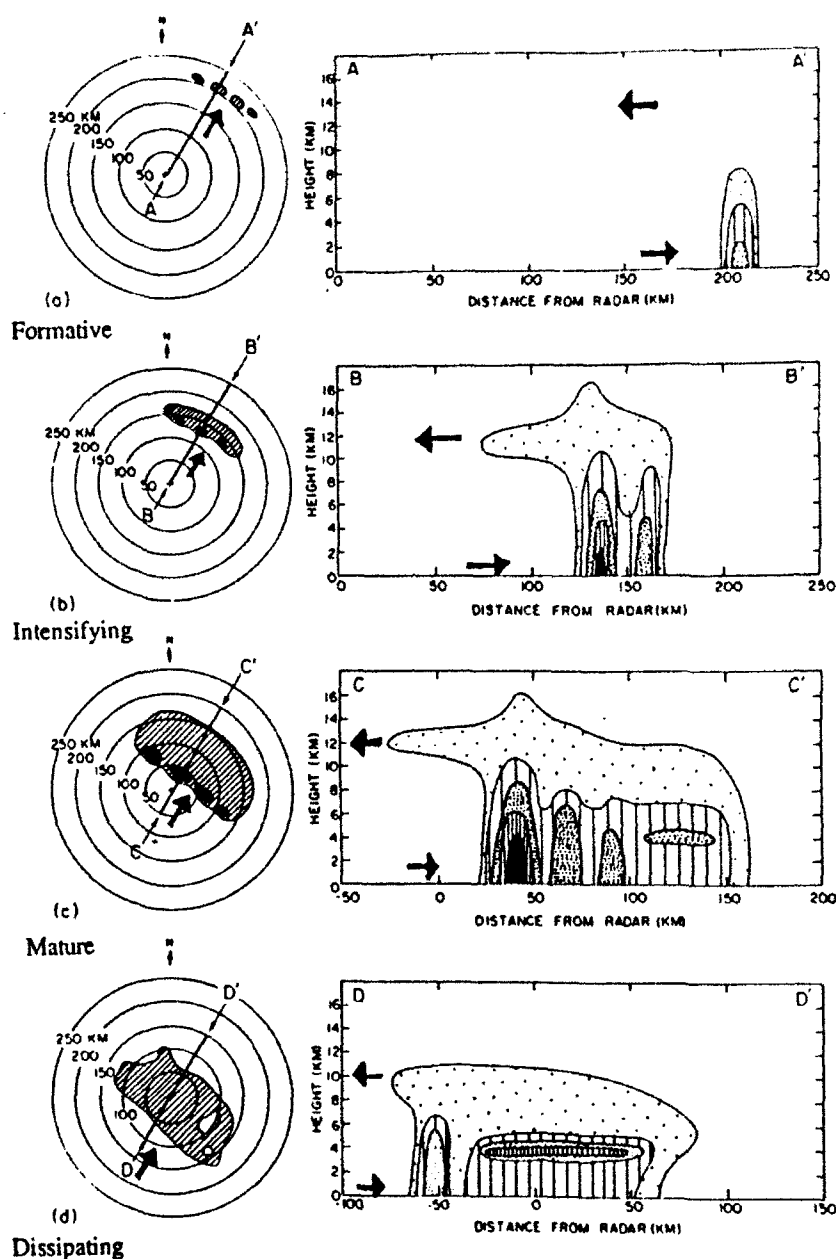
Figure 6. Schematic of the structure of a mesoscale precipitation feature as viewed by radar in horizontal and vertical cross-sections during the (a) formative, (b) intensifying, (c) mature, and (d) dissipating stages of its lifecycle. The outside contour of reflectivity is the weakest detectable echo, and the inner contours are for successively higher reflectivity values. Heavy arrows on the horizontal cross-sections indicate direction of the low-level winds. Arrows on vertical cross-sections indicate direction of the low-level and upper-level winds. From Leary and Houze (1979).

through a squall line in the four basic stages of development (Leary and Houze 1979). If the strengths of convective region updrafts are related to the height and intensity of convective region echo as shown in the cross-sections, the vertical velocity field would be expected to increase as the storm evolved from the formative stage, through the intensifying stage, and into the developing stage before finally weakening in the dissipating stage.

Moreover, several numerical modeling studies of squall line evolution have indicated that the mean vertical motion field of the convective region could possibly exhibit temporal variations related to mesoscale evolution within the storm. The two-dimensional anelastic cloud model used by Fovell and Ogura (1988) was shown to have a pseudo-periodic oscillation of the maximum vertical velocity over the analysis domain, which persisted throughout the model run (Fig. 7). An apparent transition of the model behavior to a more stable "mature" phase approximately five hours into the simulation was marked by the firm establishment of an upshear tilt of the convective updrafts and the rearward expansion of the trailing stratiform precipitation area.

Similar results were reported by Rotunno et al. (1988) in two-dimensional and Weisman et al. (1988) in three-dimensional simulations of squall line evolution. Large-amplitude quasi-periodic oscillation of the maximum updraft velocity in their models (Fig. 8) was noted over the first five hours of simulation before a transition was made to a less-oscillatory, weaker state. Again, the fundamental change in the temporal behavior of the maximum updraft velocity was accompanied by the establishment of pronounced upshear tilt of the convective updrafts and rearward transport of precipitation, suggesting that the convective region vertical velocity field may be significantly altered as a result of a mesoscale storm evolution.

The goal of this study was to determine if the variation of convective region vertical velocity profiles may be related to the evolution of the convective region over a meso (~1 hr) time-scale, and to examine the correlation between the variations in the convective region vertical velocity field and changes within the mesoscale circulation of the storm. To achieve this goal, the variation in area-averaged vertical motion over a mesoscale portion of the convective region of the 10 - 11 June 1985 squall line system observed during PRE-STORM (Preliminary Regional Experiment for Stormscale Operational and Research Meteorology - Central Phase) was examined. Particular emphasis was given to the temporal changes within a 50 km along-line segment of the convective line, at seven analysis times over a nearly one hour period. To better understand the changes in the mean vertical motion profiles, the population distributions of upward and downward
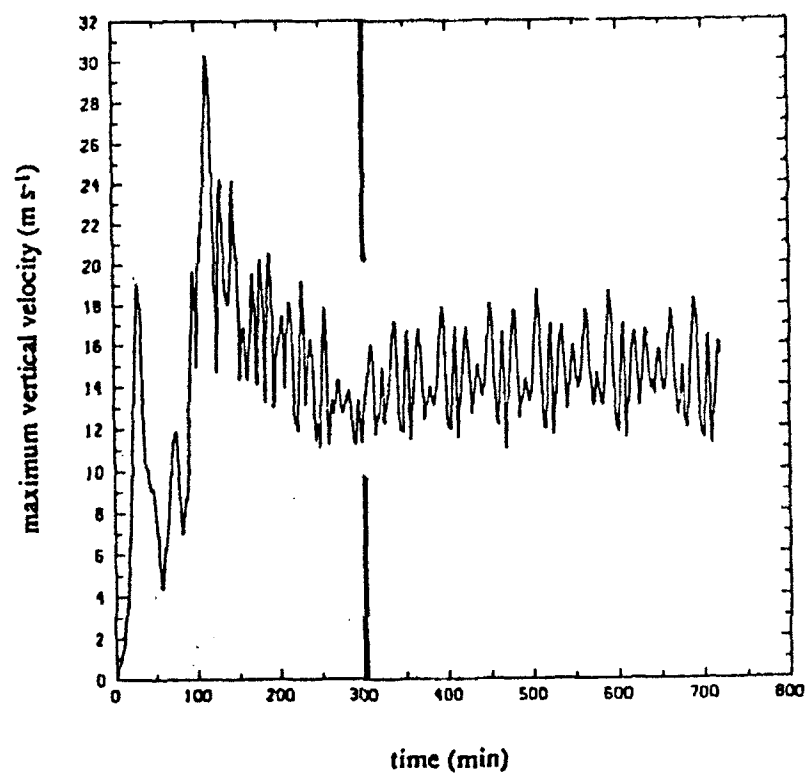
Figure 7. Time series of maximum vertical velocity for a two-dimensional anelastic cloud model with full ice parameterization. From Fovell and Ogura (1988).
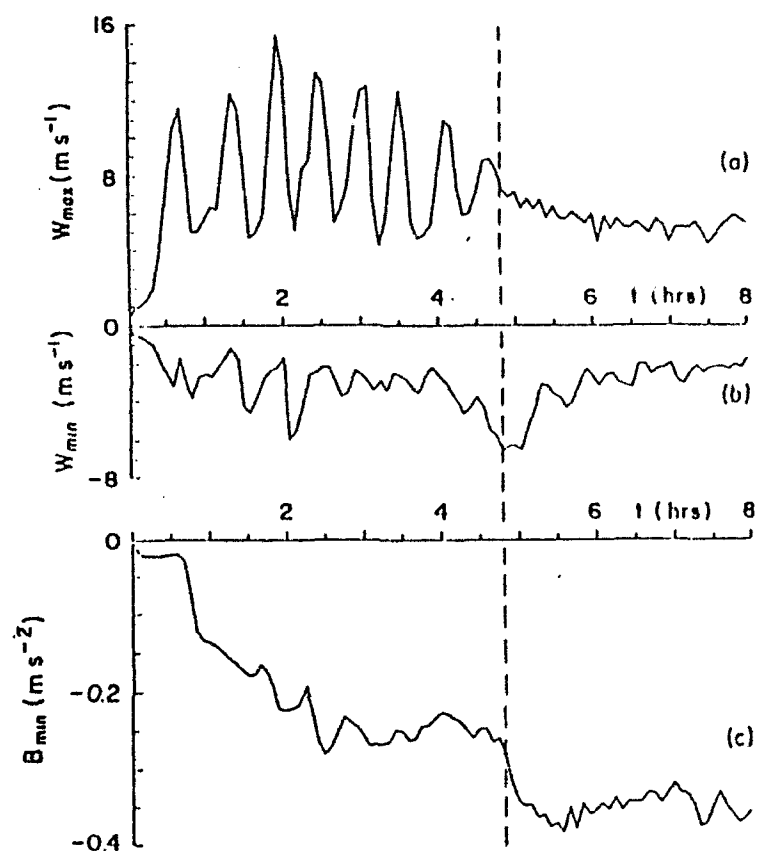
Figure 8. Time series for the two-dimensional simulation of (a) the maximum vertical velocity, w_{max}, (b) the most intense rainy downdraft, w_{min}, and (c) the minimum bouyancy of the cold pool. Note that the quasi-periodic behavior in w_{max} ends abruptly after the intense downdraft near t = 5 h makes the cold pool significantly colder. Adapted from Rotunno et al. (1988).

vertical motion at each analysis time were examined. The coherency of the variations in mean convective vertical motion were then examined and related to changes in the internal circulation of the storm system.

The squall line that occurred on 10 - 11 June 1985 over the Kansas - Oklahoma region during the PRE-STORM field program has provided perhaps one of the best opportunities to date from which to conduct a study of the vertical velocities within the convective region of a squall line. Not only was there a wide array of complementary instrumentation systems in-place with which to sample the storm, but the storm developed and moved through the observing network in such a manner that a fairly significant portion of its lifecycle could be measured by these instruments.

CHAPTER II

PREVIOUS STUDIES

Previous observational studies of the vertical motion fields within tropical and midlatitude squall line systems have employed various methods of analysis; however, the results are not as consistent for convective regions of these storms as for their stratiform regions. One difficulty in diagnosing the convective region is the relatively small scale of the individual updrafts and downdrafts and the problems associated with sampling them, either individually or as a group (Houze 1989).

LeMone and Zipser (1980) used aircraft data collected during GATE (Global Atmospheric Research Program's Atlantic Tropical Experiment) to examine the scales and intensities of vertical drafts associated with oceanic tropical cumulonimbus clouds. Using data collected over 10^4 km of flight legs over six days they derived statistics of vertical velocity (w) "drafts" and "cores." Drafts were defined to exist where |w| exceeded 0.5 ms^{-1} continuously over at least 500 m of flight leg. Cores were defined to exist where |w| exceeded 1.0 ms^{-1} continuously over at least 500 m of flight leg (without changing sign).

Using these definitions, Zipser and LeMone compiled distributions of mean, maximum, and minimum vertical velocity, diameter, and mass flux for drafts and cores as a function of height. As the flight legs were chosen without reference to individual convective towers, but rather, through and around cloud clusters, they believe the resulting dataset resembles a random sample of mesoscale disturbed areas, which necessarily includes clouds in various stages of development. While their results are at present the best available indicator of the scales and intensities of the individual drafts (Houze 1989), the fact that the data are presented without reference to the type of storm organization or the storm's stage of development, makes them difficult to compare with the convective region of specific storms.

Ogura and Liou (1980) used data from a special rawinsonde network to examine the structure of the 22 May 1976 Oklahoma squall line. Due to limitations in the availability of data, they used a time-to-space composite to derive the mean structure of the squall line during its mature stage. All sounding data for a six hour period were interpolated onto a grid with 45 km horizontal spacing and 50 mb vertical spacing. Computed horizontal divergence values were then used kinematically to derive vertical velocities which were then averaged in the along-line direction. While Ogura and Liou

were able to estimate the magnitude of mean vertical drafts on the mesoscale, their compositing scheme was unable to resolve convective-scale motions.

Gamache and Houze (1982) constructed profiles of mean vertical velocity for the convective and stratiform regions of the 12 September 1974 GATE squall line using a technique to composite aircraft and rawindsonde wind observations in relation to radar echo patterns. Isochrones of the leading edge of radar echo were used to locate the origin of a moving coordinate system attached to the squall line, over a nine hour period. Observed wind data were then placed into the traveling coordinate system, interpolated to a grid with 50 km horizontal spacing, and used to derive horizontal divergence values. Vertical velocities were then computed kinematically and mean profiles were derived for the convective and stratiform regions. Gamache and Houze delineated the convective region as that area encompassed by the leading edge and ends of the squall line as depicted by low-level reflectivity, and a rear boundary defined to exist where reflectivity fell to less than 38 dbZ and the horizontal gradient of reflectivity fell to less than 1 dB km^{-1}. While this was the first study to derive the mean vertical velocity profile for specific regions of a squall line, it was still unable to resolve convective-scale motions or spatial variations within the profile.

Houze and Rappaport (1984) constructed mean vertical velocity profiles for the pre-line, convective, transition, and stratiform regions of the 28 June 1974 GATE squall line using a technique similar to Gamache and Houze (1982) to composite aircraft and rawindsonde data in relation to temporal radar echo patterns, but were still unable to resolve convective scale motions.

Heymsfield and Schotz (1985) used dual and triple-Doppler analyses to examine the three-dimensional structure of the 2 May 1979 Oklahoma squall line during its mature stage. Paired radar scans from four times during a 45 minute period were interpolated to a grid with 1.2 km horizontal and 1.0 km vertical spacing. After retrieving the horizontal wind field, the vertical velocity field was then computed from vertical integration of the anelastic continuity equation. While not the first to use multiple-Doppler techniques, Heymsfield and Schotz's analyses were perhaps the first to resolve the multi-cell structure of a squall line system. However, as the storm was relatively far from the radars for multiple-Doppler techniques, their discussion of convective structure was primarily qualitative in nature.

Smull and Houze (1987) used a dual-Doppler analysis to construct area-averaged vertical velocity profiles of the convective, transition, and stratiform regions of the 22 May 1976 Oklahoma squall line during its mature stage. Radar scans from a single three minute

period were combined and interpolated to a grid with 1.0 km horizontal and 0.8 km vertical resolution, and vertical velocities were derived from anelastic continuity. From their analysis, Smull and Houze were able to compute area-averaged mean vertical velocity profiles and were also able to show that the convective line exhibited organized multicellular structure resulting from discrete propagation, in which new cells develop along the leading edge of a line of mature cells, while older cells dissipate towards the rear. However, data were not available to determine along-line variations in the mean vertical velocity profiles and only one radar scan time was available so the detection of any temporal variations in the profiles was not possible.

Chong et al. (1987) described the airflow within the 22 June 1981 West Africa squall line during the COPT 81 (Convection Profonde Tropicale) field experiment. Five consecutive coplanar dual-Doppler radar scans of a 35 km segment of the convective line were collected over a 27 minute period during the mature stage of the storm. Three-dimensional wind fields were then derived by integration of mass continuity in a method adapted for coplanar Doppler radar scans. While their investigation described and characterized the vertical motions within the analysis region, they did not elaborate on temporal or spatial variations.

Biggerstaff et al. (1988) also used dual-Doppler techniques to examine the convective-scale motions within three MCSs observed during PRE-STORM. Their investigation of the 28 May, 3 - 4 June, and 10 - 11 June 1985 squall lines focused specifically on the spatial arrangement and intensity of the individual updrafts and downdrafts within the convective regions of these storms. In each case, their analyses suggested the existence of three basic types of vertical drafts within the convective region: a somewhat continuous tilting updraft, a low-level downdraft, and an upper-level downdraft. They also noted that the strengths and sizes of the vertical drafts varied from case to case and were three-dimensional in character. While their results summarized the basic character of the individual convective drafts within three separate storms, they did not address along-line or temporal variability, nor area-averaged vertical motions.

Balsley et al. (1988) used a 50 MHz wind profiler on the tropical island of Pohnpei to construct long-term mean vertical wind profiles under various atmospheric conditions, one of which was heavy rainfall. The average profile was constructed to correspond, in so far as possible, to conditions similar to those present in the convective regions of tropical MCSs. While the high resolution of the profiler was able to elucidate additional features of the mean vertical motion profiles which are not apparent in more conventional analyses, the profiles are long-term composites of features that passed through the relatively small

sampling region directly above the profiler site and are not correlated with the spatial and temporal evolution of a squall line. Furthermore, rawinsonde observations taken for comparison were not coincident with the profiler location nor was any radar imagery available in conjunction with the profiler measurements. Additionally, limitations in profiler technology precluded observations below 3 - 4 km.

As new observational tools have recently become available, our ability to resolve convective scale aspects of squall line systems has improved several-fold. Analyses of various rawinsonde datasets collected over special networks provided our first estimates of mesoscale atmospheric motions but their resolution is too coarse to resolve convective-scale structure. Aircraft have provided *in-situ* observations of the strengths and scales of individual drafts encountered within MCSs but their spatial and temporal sampling limitations make it difficult to use their data to study convective evolution. The high resolution capability of wind profilers has been used to accurately measure vertical atmospheric motions during convective precipitation events. However, their limitation of sampling only those phenomena that pass directly overhead has prohibited their use in the spatial and temporal examination of discrete convective structures. The use of multiple-Doppler analyses has for the first time provided the ability to resolve and examine the convective scale motions of squall line systems. While studies to this date have used this ability to characterize the vertical motions within the convective region of several squall lines, none have examined the spatial and temporal variations of these area-averaged vertical velocity profiles.

CHAPTER III

OVERVIEW OF THE 10 - 11 JUNE 1985 SQUALL LINE

The synoptic conditions over the central United States nearly 9 hours prior to the development of the 10-11 June 1985 squall line are depicted by the 1200 UTC 500 mb, 850 mb, and surface analyses charts shown in Figs. 9, 10, and 11, respectively. A weak shortwave trough at 500 mb lay over the central Rockies while a high pressure ridge with weak flow lay over Oklahoma and northern Texas (Fig. 9). In addition to the trough, the 850 mb analyses (Fig. 10) depicts a tongue of moisture with dewpoints in excess of 15 °C extending from east Texas into central Oklahoma and Kansas. The shortwave trough also supported a surface cold front anchored to a low pressure center in northeast Colorado at this time (Fig. 11).

By 2100 UTC this cold front was entering central Nebraska and western Kansas, and the squall line developed in a weak baroclinic zone ahead it (Johnson and Hamilton 1988). As the storm developed to the west of the primary PRE-STORM mesonetwork, between the standard synoptic-data collection periods, details of the environment immediately preceeding the storm are not available. However, the 2100 UTC Woodward, Oklahoma (WWR) sounding (Fig. 12) is probably representative of tne pre-squall environment (Biggerstaff and Houze 1991a).

The lifting condensation level (LCL) and level of free convection (LFC) of the WWR sounding were 790 and 640 mb, respectively, for a parcel whose temperature and mixing ratio are the density-weighted average over the lowest 500 m. Evidently, deep lifting would have been required to bring the parcel to its LFC; the convective inhibition (CIN: Bluestein and Jain 1985) was 77 J kg^{-1}. Thus, lifting in the vicinity of the surface front may have helped initiate the squall line (Biggerstaff and Houze 1991a). The convective available potential energy (CAPE: Moncrieff and Miller 1976; Weisman and Klemp 1982) of the sounding was 1660 J kg^{-1}, which corresponds well with the typical CAPE associated with non-severe, broken-line developing (Bluestein et al. 1987) squall lines (Biggerstaff and Houze 1991a). The magnitude of the density-weighted wind-shear in the lowest 2.5 km was about 5.0 ms^{-1}km^{-1}, directed from 290° (Biggerstaff and Houze 1991a).

Also at around 2100 UTC, the developing convective line became evident in visible satellite imagery as an arc-shaped line of convection extending from western Kansas,
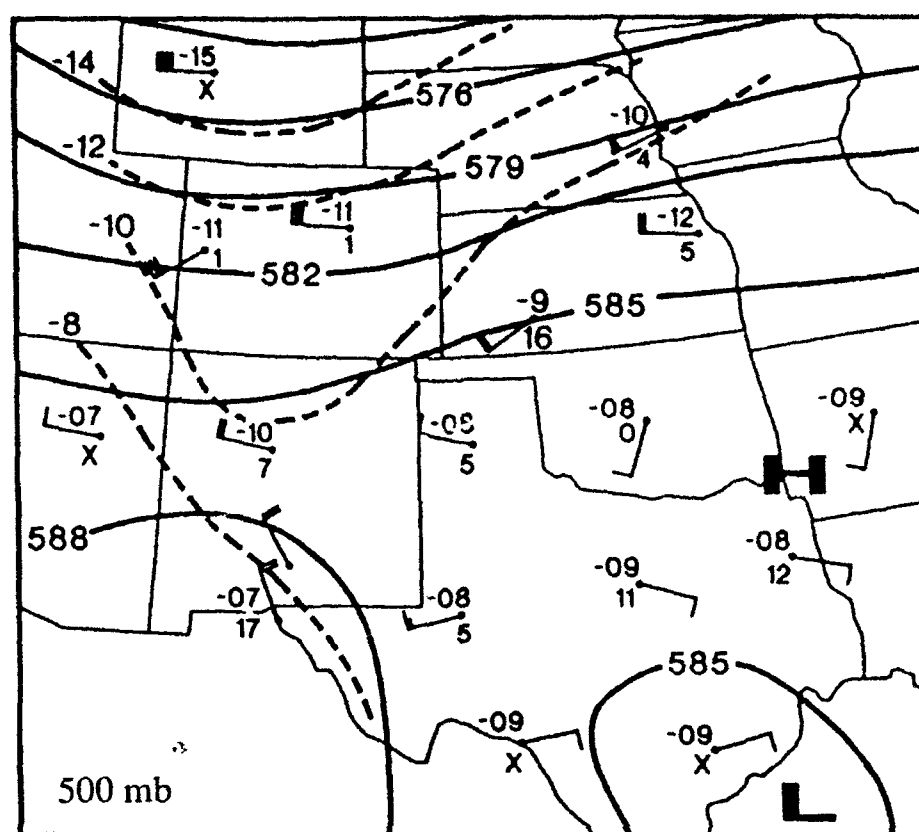
Figure 9. 500 mb analysis at 1200 UTC 10 June 1985. Solid contours are geopotential height at 30 decameter interval. Temperatures are contoured every 2^0C (dashed lines). The typical station model has been used; a full flag on the wind barb is 5 ms^{-1}, a half flag is 2.5 ms^{-1}; temperature and dewpoint depression are plotted in °C. From Vasiloff (1989).
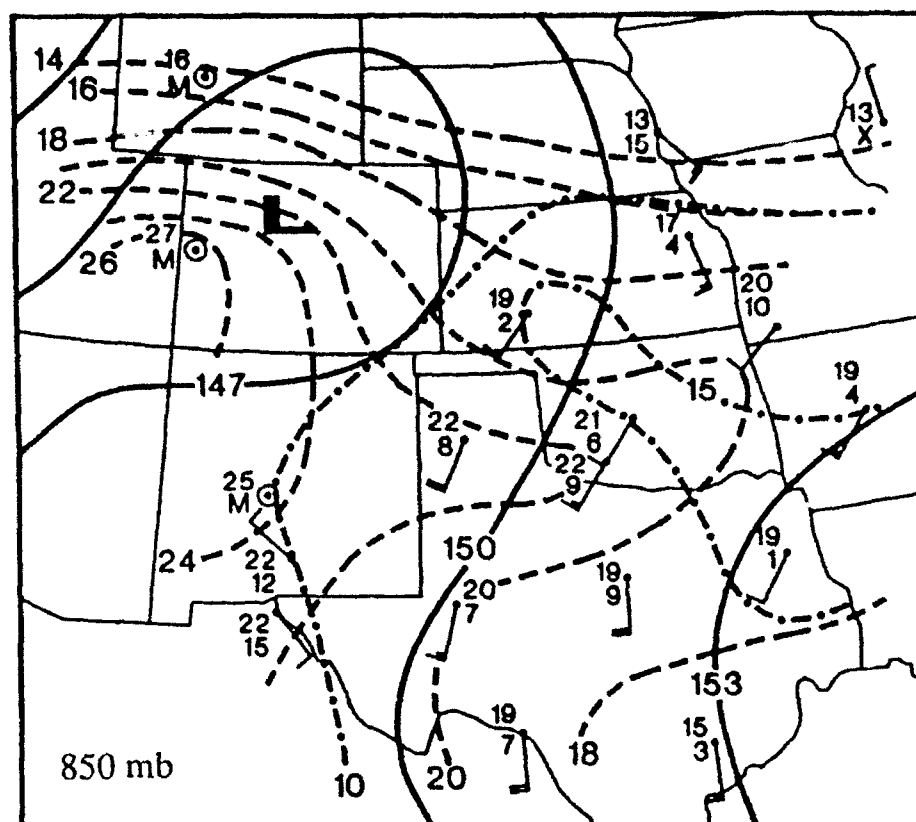
Figure 10. 850 mb analysis at 1200 UTC 10 June 1985. Solid contours indicate geopotential height at 3 decameter intervals. Isotherms are drawn as dashed contours at 2 °C interval. Isodrosotherms are drawn as dash-dot contours at 5 °C interval. The station plotting model is as in Fig. 8. From Vasiloff (1989).
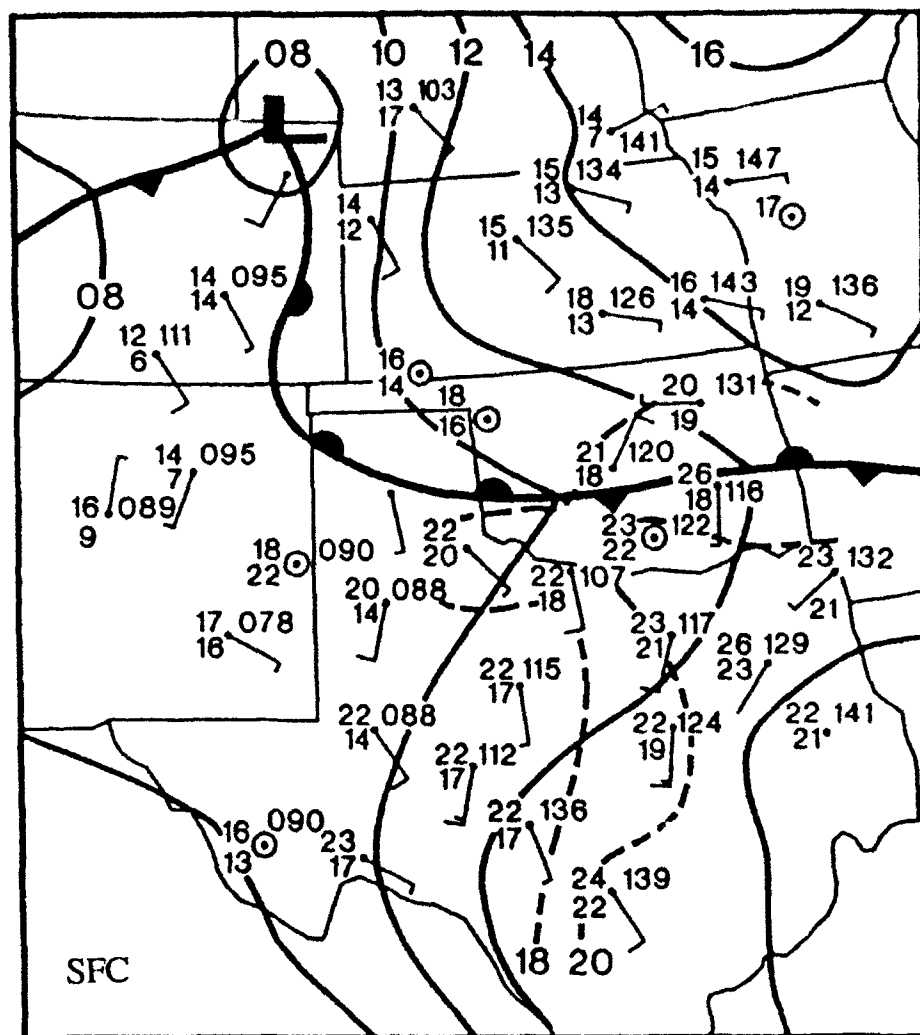
Figure 11. Surface analysis at 1200 UTC 10 June 1985. Isobars are drawn every 2 mb with the leading 10 omitted. The typical station plotting model is used; temperature (°C), dewpoint temperature (°C), pressure (mb; multiplied by 10 with the leading 10 omitted), and winds (a full flag on the wind barb is 5 ms⁻¹, a half flag is 2.5 ms⁻¹). The 18 and 20 °C isodrosotherms are shown as dashed lines. From Vasiloff (1989).
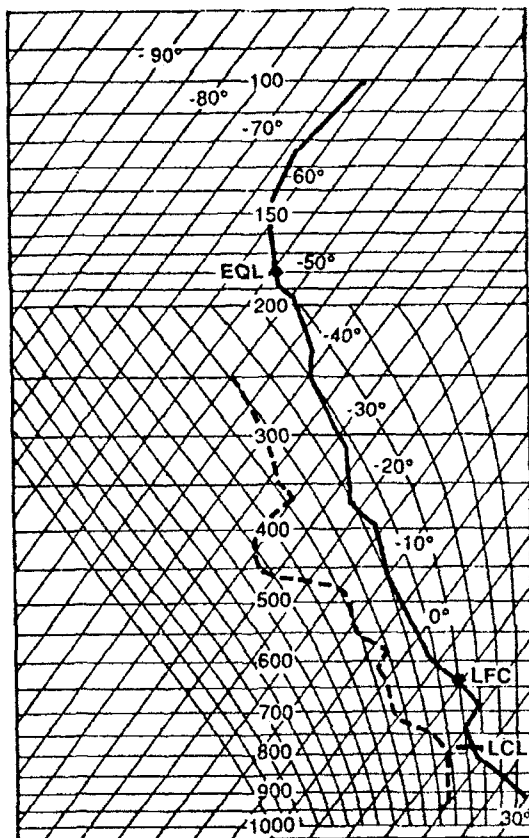
Figure 12. Woodward, Oklahoma (WWR) 2100 UTC 10 June 1985 skew T-log p profile of temperature (solid line) and dewpoint temperature (dashed line). The lifting condensation level (LCL), level of free convection (LFC), and equilibrium level (EQL) are shown. Pressure is indicated in mb, temperature in °C. From Biggerstaff and Houze (1991a).

southwestward through the Oklahoma and Texas panhandles (Johnson and Hamilton 1988).

By 2200 UTC the well-developed convective line entered the range of the National Weather Service (NWS) WSR-57 storm surveillance radar at Wichita, Kansas (Rutledge et al. 1988). The subsequent movement of the storm through the region between 2320 - 0301 UTC can be seen in the composite WSR-57 plan-position indicator (PPI) patterns in Fig. 13. The convective line was also within range of the National Center for Atmospheric Research (NCAR) CP-3 and CP-4 5-cm Doppler radars from about 01 to 04 UTC. However, the combination of storm movement, width of the convective line, and scan geometry limits the period of exceptional dual-Doppler coverage of the convective line to about 0120 - 0208 UTC.

By 2300 UTC enhanced IR (infra-red) satellite imagery (not shown here; see Rutledge et al. 1988) indicated a cold cloud shield developing over western Kansas in association with developing convection. Intense convection was also noted west of Wichita, Kansas, in the 2320 UTC PPI radar display (Fig. 13a) and extended soutwestward into the Texas panhandle. Significant echoes are also seen to the east of Wichita in association with a separate area of dissipating convection.

By 0100 UTC, IR satellite imagery indicated a cold cloud shield covered much of Kansas and an area of cloud top temperatures < -70 °C were noted over south-central Kansas in association with the strongest convection. Although a very strong line of convection is apparent in the 0103 UTC PPI radar display (Fig. 13b) with numerous cells in excess of 50 dBZ, the echo to the rear of the convective line was still weak, indicating that the storm was still in the intensifying stage of evolution.

At 0200 UTC the cold cloud shield continued to expand on the IR satellite imagery and covered much of Kansas. The 0200 UTC PPI radar display (Fig. 13c) shows that the well-defined convective line had nearly moved through the western portion of the Doppler radar coverage. Additionally, the area of light precipitation behind the line had begun to expand rapidly and increase in intensity, indicating that the storm was now in the mature stage of evolution as defined by Leary and Houze (1979).

By 0300 UTC the area of cold cloud shield had reached its maximum areal extent with < -70 °C temperatures covering some 30,000 km^2. Both the convective line and trailing stratiform area are well-defined in the 0300 UTC PPI radar display (Fig. 13d). A large area of reflectivity in excess of 25 dBZ is now noted in the stratiform region. Additionally, the number of convective cells in excess of 50 dBZ had decreased significantly (Rutledge et al. 1988).
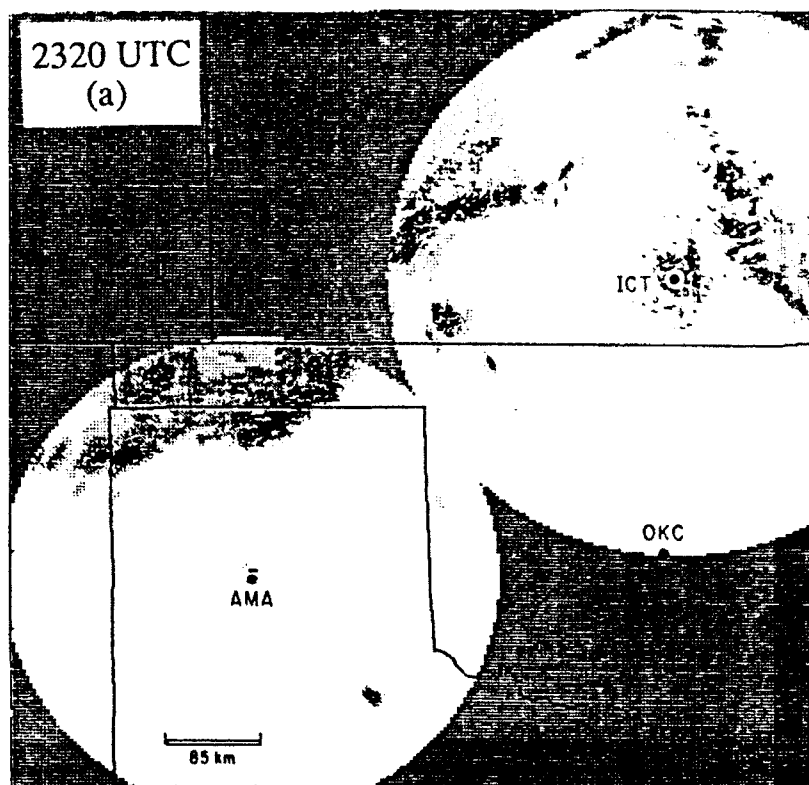
Figure 13. Composite low-level echo patterns from the Amarillo (AMA), Texas, Wichita (ICT), Kansas, and Oklahoma City (OKC), Oklahoma WSR-57 10-cm storm surveillance radars on 10 - 11 June 1985 for (a) 2320 UTC, (b) 0103 UTC, (c) 0200 UTC, and (d) 0301 UTC. Data from each of the three sites was not available at all times shown. Reflectivity values are: 15 - 25 dBZ, light stippling; 25 - 35 dBZ, heavy stippling; 35 - 50 dBZ, hatching; > 50 dBZ, solid. Range circles (130 km) in (c) denote coverage of CP-3 and CP-4 Doppler radars. From Rutledge et al. (1988).
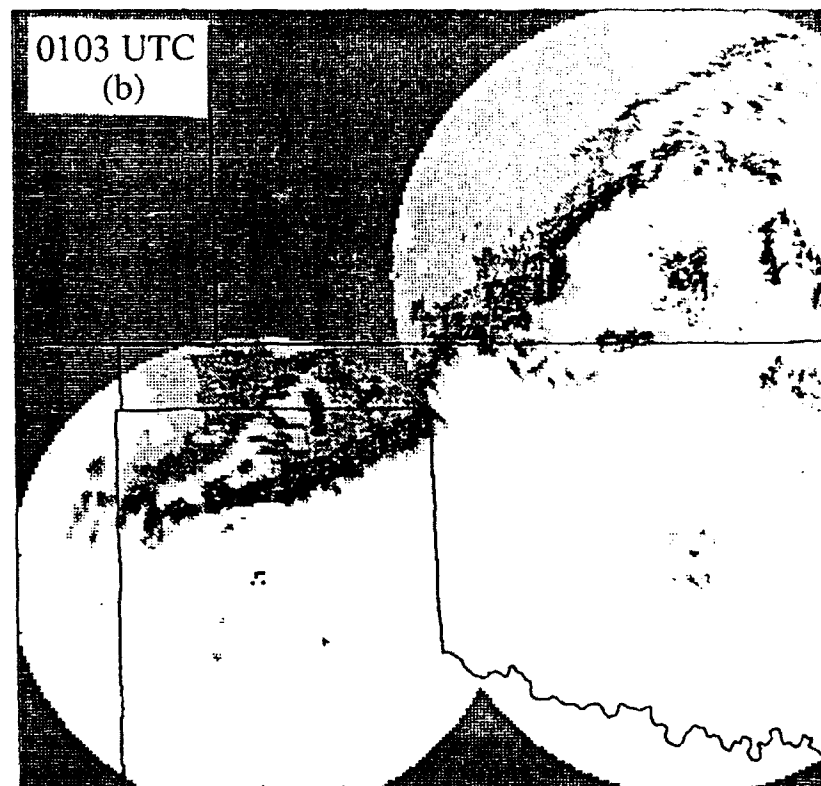
Figure 13. (*Continued*)
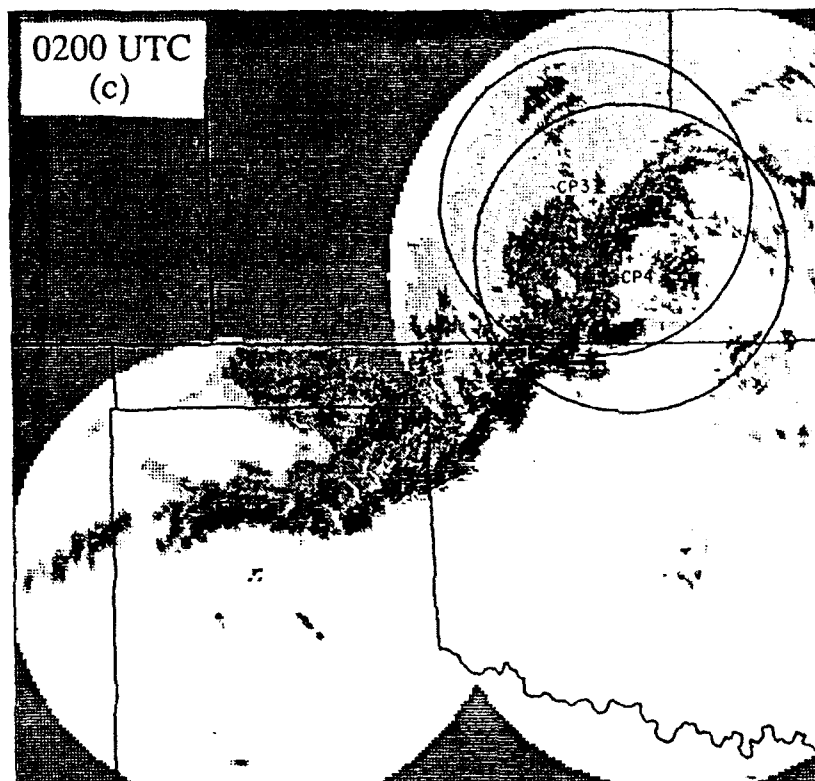
Figure 13. (*Continued*)
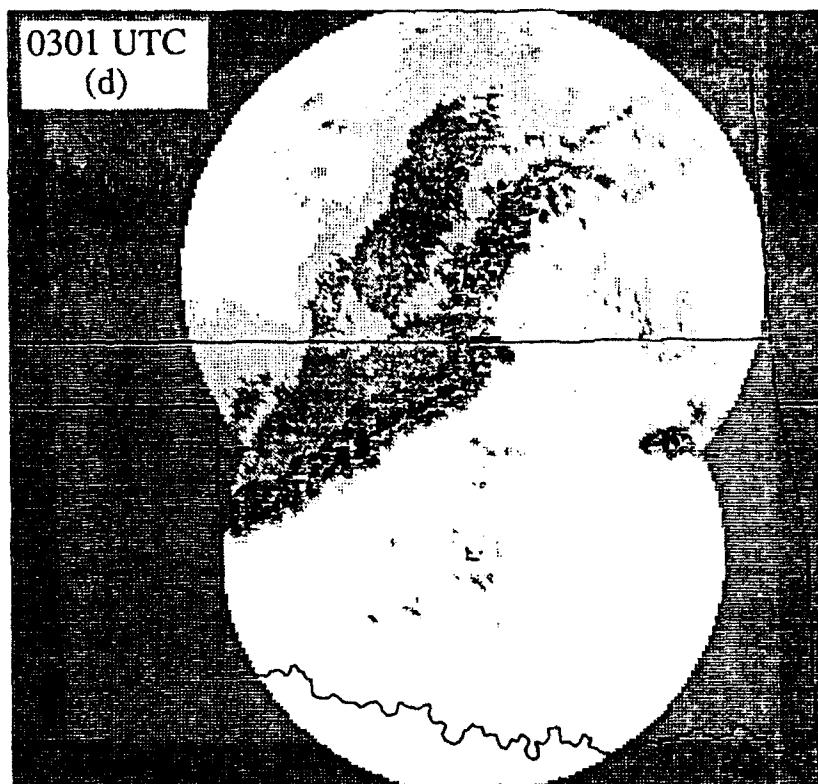
Figure 13. *(Continued)*

The storm then continued to weaken and by 0600 UTC nearly all the deep convection had dissipated, although two areas of stratiform precipitation persisted over much of the region for several additional hours.

CHAPTER IV

DATA AND METHOD OF ANALYSIS

Instrumentation and Data

The primary data for this study consists of seven dual-Doppler radar analyses, each covering approximately a 120 km x 120 km area of the 10 - 11 June 1985 Oklahoma - Kansas squall line during the early part of the mature stage of the storm. The reflectivity and radial velocity data for these analyses were collected by a pair of NCAR 5-cm Doppler radars deployed just northwest of Wichita, Kansas, on a 60 km north-northwest-south-southeast baseline during PRE-STORM. Within a range of 60 km of each radar, the horizontal and vertical resolution of the Doppler-derived wind field is no worse than 6 km and 3 km respectively (except along the baseline). A brief summary of the characteristics of the NCAR Doppler radars is given in Table 1. These radars were able to sample the northern end of the squall line system during the early mature phase of the storm. The southern end of the squall line system was sampled at a later time by two 10-cm Doppler radars operated by NSSL (National Severe Storms Laboratory) and positioned on a 40 km northwest-southeast baseline near Norman, Oklahoma. Vasiloff (1989) has examined these data, which represent the southern portion of the storm during the early part of its dissipating stage. Figure 14 shows the locations of the NCAR and NSSL Doppler radars as well as several of the NWS WSR-57 storm surveillance radars that provided digitized data in support of the PRE-STORM field program.

The NCAR Doppler radars were able to sample the northern portion of the convective line from approximately 0120 - 0219 UTC. Volume scans were generally taken by sweeping azimuthally over a conical surface at 32 various elevation angles between 0.2° and 58.0°. Volumes containing full 360° azimuthal scans were collected every half-hour, with sector volume scans (over a subset of aximuthal angles) collected between full 360° volume scans. This scanning strategy provided high-resolution data for dual-Doppler analyses in areas on both sides of the north-northwest-south-southeast baseline as indicated in Figure 14 (hereafter referred to as east and west lobes). Nearly continuous scanning from 0120 to 0219 UTC provided six sector-scans and two 360° scans from each radar, yielding a temporal resolution of 6 to 10 minutes between volume scans. All of these data have been analyzed as part of this study. A summary of radar scan parameters and Doppler analysis times are given in Table 2.

Table 1. Characteristics of the NCAR Doppler radars used during PRE-STORM.

	Radar	
	CP-3	CP-4
Wavelength (cm)	5.45	5.49
Maximum Range (km)	135	135
Nyquist Velocity (ms^{-1})	15.37	15.24
Peak Power (kW)	400	400
Pulse Width (μs)	1.0	1.0
Pulse Repetition Frequency (Hz)	1111	1111
Minimum Detectable Signal (dBm)	-113	-112
Number of Range Gates	512	512
Azimuthal Resolution (deg)	0.8	0.8
Gate Spacing (meters)	260	260
Number of Samples	64	64
Beamwidth (deg)	1.0	1.0
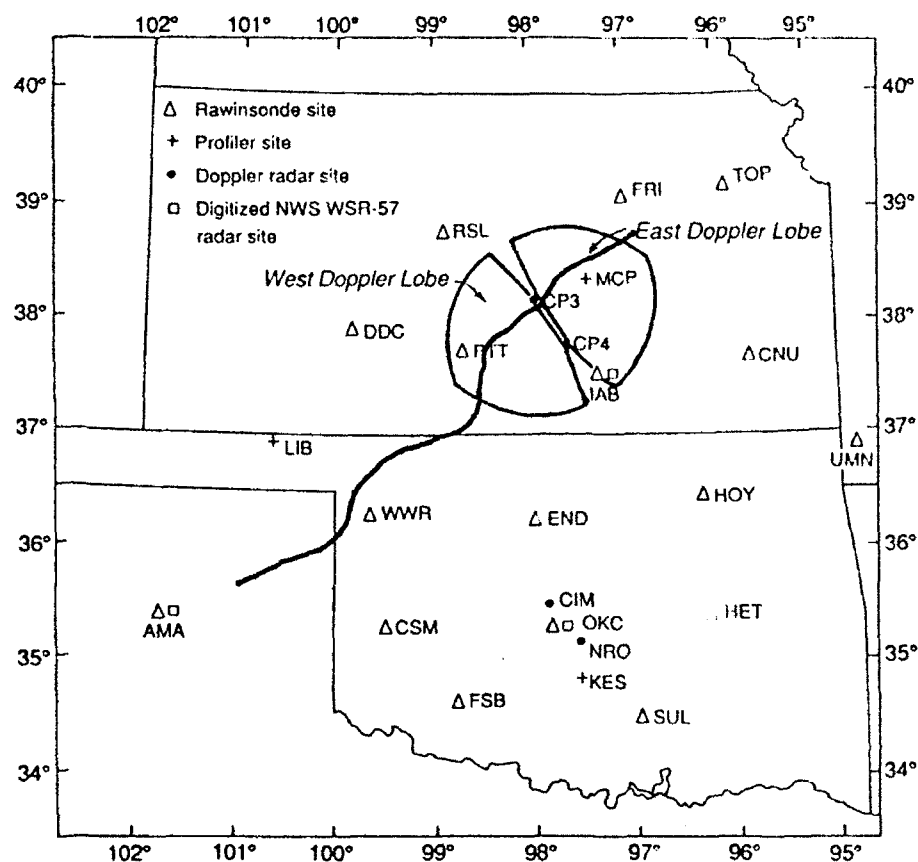
Figure 14. PRE-STORM radar and rawinsonde networks. Also shown is the position of the leading edge of the 10 11 June 1985 squall line at 0134 UTC. Adapted from Biggerstaff and Houze (1991a).

Table 2. Summary of the NCAR 5-cm Doppler-radar scanning strategy and dual-Doppler analysis times for 0119 - 0219 UTC during the 10 - 11 June 1985 storm.

Radar	Start Time (UTC)	Stop Time (UTC)	Azimuth Range (deg)	Elevation Range (deg)	Doppler Analysis Time (UTC)	Doppler Lobes
CP-3	01:19:55	01:25:46	153 - 310	0.2 - 58.0	01:22:00	West
CP-4	01:19:55	01:24:54	177 - 330	0.2 - 42.3		
CP-3	01:25:52	01:31:39	153 - 310	0.2 - 58.0	01:29:00	West
CP-4	01:26:43	01:32:35	218 - 012	0.2 - 58.0		
CP-3	01:31:45	01:37:34	153 - 310	0.2 - 58.0	01:34:00	West
CP-4	01:32:57	01:38:28	218 - 012	0.2 - 58.0		
CP-3	01:38:59	01:49:20	000 - 360	0.2 - 58.0	01:44:00	East/West
CP-4	01:39:00	01:49:22	000 - 360	0.2 - 58.0		
CP-3	01:50:02	01:55:47	155 - 310	0.2 - 58.0	01:53:00	West
CP-4	01:50:00	01:55:52	177 - 330	0.2 - 58.0		
CP-3	01:55:54	02:01:44	155 - 310	0.2 - 58.0	01:59:00	West
CP-4	01:56:00	02:01:49	177 - 330	0.2 - 58.0		
CP-3	02:01:50	02:07:39	156 - 310	0.2 - 58.0	02:05:00	West
CP-4	02:01:58	02:07:46	177 - 330	0.2 - 58.0		
CP-3	02:09:00	02:19:00	000 - 360	0.2 - 58.0	02:14:00	East/West
CP-4	02:08:59	02:19:00	000 - 360	0.2 - 58.0		

As the forward edge of the convective line was exiting the west lobe analysis domain during the 0209 - 0219 UTC radar volume scan, area-averaged vertical velocity profiles of the convective region at this time were biased towards the downdrafts typically located near the rear of the convective region. For this reason the west lobe Doppler analysis at 0214 UTC was eliminated from further consideration in this study. The east lobe analyses at 0144 and 0214 UTC were also eliminated in order to focus more on the time variations within the remaining west lobe analyses.

Derivation of the Vertical Motion Fields

A separate dual-Doppler analysis was performed on each of the lobes of Doppler radar data collected at the times in Table 2, following the technique of Biggerstaff and Houze (1991a). Before the analysis was initiated, the Doppler data were carefully edited and the radial velocities were unfolded using the RDSS (Research Data Support System) software (Oye and Carbone 1981). Noise in the velocity field was removed by thresholding out those points with returned power less than -110 dBM. Areas of suspected side-lobe contamination and ground-clutter, as well as second-trip echo were also edited from the data. The reflectivity and radial velocity fields from the two radars were then interpolated from their polar format to a 120 km x 120 km (horizontal) x 14.9 km (vertical) Cartesian grid with a 1.0 km horizontal spacing and 0.5 km vertical spacing using the SPRINT (Sorted Position Radar Interpolation) software (Mohr et al. 1979). The dual-Doppler analyses were then accomplished using the CEDRIC (Cartesian Editing and Display of Radar Data under Interactive Control) software (Mohr and Miller 1983).

Each of the dual-Doppler analyses were initiated by applying a time-space correction to the reflectivity and radial velocity data to account for horizontal translation of the storm during the 6 - 10 minute scan times. The data fields from both radars were advected to a time near the midpoint of each analysis period. The advection was performed using a storm motion vector of 14 ms^{-1} from 300° which is considered representative for that portion of the convective line at that time (Biggerstaff and Houze 1991a). The radial velocity fields from both radars were then combined to produce an estimate of the horizontal wind field, by initially assuming the vertical motion to be zero. The reflectivity fields were also combined such that the maximum available reflectivity estimate from either radar was kept at each grid point.

The first estimate of the vertical motion field was then assumed to be due entirely to precipitation particle fall-speeds which were calculated following Marks and Houze (1987), using the reflectivity-fall-speed relationship:

$$V_t = \left(\frac{\rho_o}{\rho}\right)^{0.4} [a(Z_e)^b]$$

where:

$$a = 2.600; \; b = 0.107 \text{ for water}$$
$$a = 0.817; \; b = 0.063 \text{ for ice}$$

The effective radar reflectivity factor Z_e in standard units ($mm^6 m^{-3}$) was taken to be the reflectivity value at each grid point from the combined radar reflectivity field. Particle fall-speeds were calculated in units of meters per second. Density (ρ) was assumed to follow an exponential profile with a scale height of 10 km. The particles were assumed to be ice at and above 3.8 km mean sea level (MSL) and water below 3.4 km MSL. For the grid-level at 3.4 km an average of the two fall-speeds was used. These fall-speeds were then used along with the original estimate of the radial velocities to compute a new estimate of the horizontal wind field.

The resulting horizontal wind component fields with fall-speeds removed were then decimated at grid points where the standard deviation of the horizontal wind speed estimate was large, or where scan geometry precluded a reliable estimate of the horizontal wind (e.g. along the baseline). The horizontal wind component fields were then patched to close any well-bounded small holes, and a two-step filter (Leise 1981) was applied to remove most of the energy associated with wavelengths less than 6 km. The filtered wind components were then used to calculate a horizontal divergence field. The divergence field was then decimated at grid points where estimates of either the u and v-wind components did not exist, and finally patched to fill any well-bounded small holes.

A vertical velocity field was then calculated by integrating the anelastic continuity equation downward from echo top:

$$\nabla \cdot (\rho V) = 0$$

where ∇ is the three-dimensional gradient operator, ρ is density which is assumed to be a function of height only, and V is the three-dimensional wind vector. The upper boundary condition for the downward integration was taken to be 0.25 ms^{-1} for grid points at 13.9 km and above where reflectivity was at least 10 dBZ, and zero at all other points. This choice of upper boundary condition reflects the suggestion that areas of high reflectivity aloft are associated with areas of enhanced upward motion at upper levels (Biggerstaff and Houze 1991a). Due to the large values of divergence at upper levels, the derived vertical velocity field is not sensitive to the slight changes in upper boundary condition. No lower

boundary condition was imposed. The resulting vertical velocity field was then decimated at grid columns where the downward integration began below 8 km MSL. Integration beginning below this level was assumed to be too far from the upper boundary for the boundary condition to be valid, thus yielding unreliable estimates of vertical motion. This threshold affected very few points in the convective region. The vertical velocity field was then patched to fill any well-bounded small holes, and used with the original estimates of the horizontal wind components to compute a new estimate of the horizontal wind field. This procedure was then iterated until the absolute value of the change in the mean horizontal wind components at each level were less than 0.1 ms^{-1} from one iteration to the next. Generally, 3 to 4 iterations were required for the horizontal wind field estimates to converge. A final estimate of the vertical velocities was then computed with the last (best) estimate of the horizontal winds to ensure mass continuity between the two fields.

Finally, so that cross-sections of the various fields could be made perpendicular to the convective line, the analysis domain was rotated clockwise 30° about the vertical axis such that the positive x-axis points to 120° clockwise from north. The u and v-wind components were then projected onto the rotated coordinate system. Cross-line storm-relative flow was then computed by subtracting the storm motion (14 ms^{-1}) from the rotated u-wind component.

Objective Analysis of the Convective Region

As the fundamental goal of this study was to expand our knowledge of the structure of the vertical motion field within the convective region of an MCS, a method was devised to objectively identify the convective region and sample only those grid points within that region. Most previous studies determined mean vertical velocities by arbitrarily placing linear boundaries around the high reflectivity features of a low-level PPI display, extending the boundaries vertically to create a volume, and sampling all points within the volume. This study uses a modified version of the same basic approach but employs features that attempt to improve the estimate of vertical velocities by including contributions from developing cells on the leading edge of the convective line, and limiting contributions from areas that may be better classified as being in the transition zone.

According to the squall line model of Houze et al. (1989) shown in Fig. 1, developing convective cells along the leading edge of the line would exhibit maximum reflectivity at mid-levels and may not yet have a low-level reflectivity signature. The vertical cross-section of reflectivity shown in Fig. 15 indicates such a developing cell along the leading edge of the convective line at 0ʹ44 UTC (near x = 25 km). The vertical
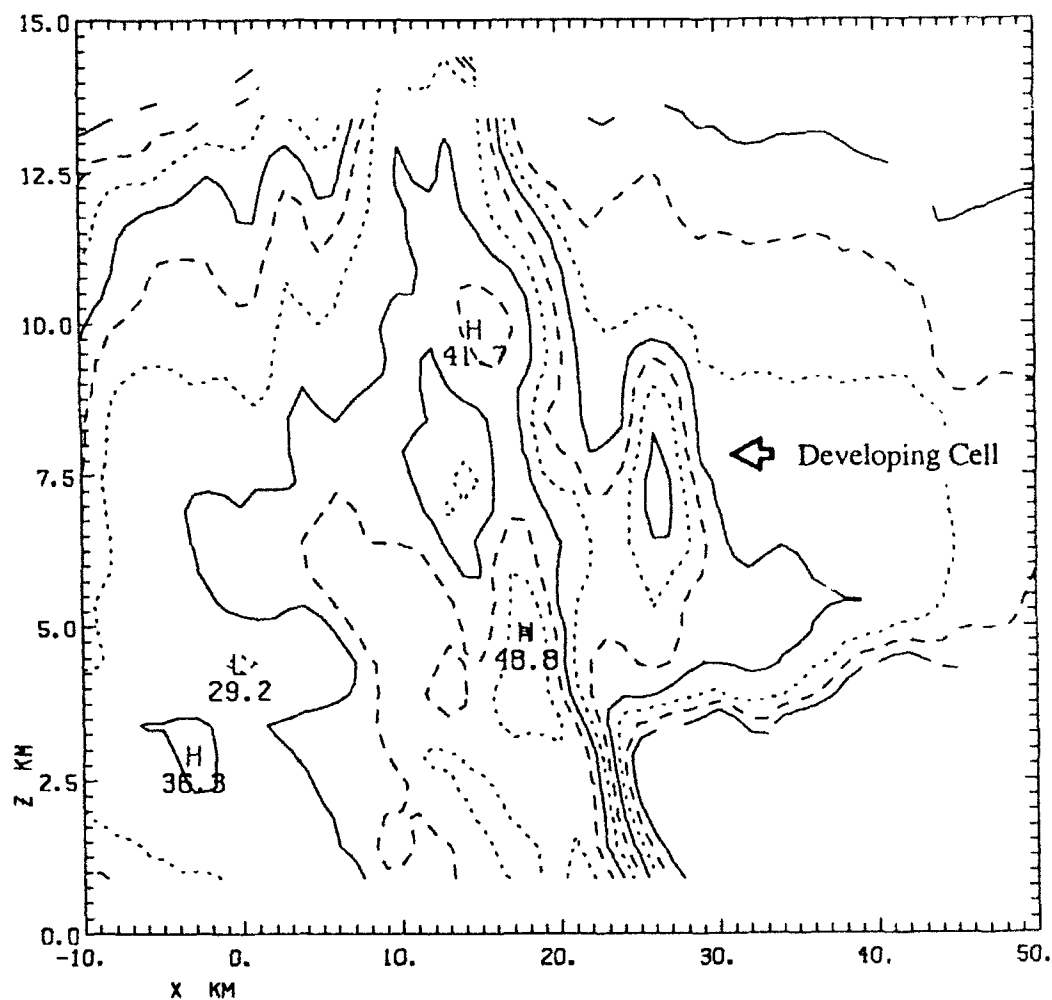
Figure 15. Vertical cross-section of radar reflectivity through the convective region along Y = 32 km at 0144 UTC. Reflectivity contours are: 5 dBZ (solid), 10 dBZ (long dashed), 15 dBZ (dotted), then repeating; 20 dBZ (solid), 25 dBZ (long dashed), 30 dBZ (dotted), 35 dBZ, (solid), 40 dBZ (long dashed), and 45 dBZ (dotted). Reflectivity maxima are indicated. Storm motion is left to right.

velocities associated with this reflectivity pattern are shown in Fig. 16 and the strong updraft corresponding to the developing cell can be clearly seen. Sampling methods which define boundaries using only the low-level reflectivity may exclude the grid columns containing these updrafts, which are an important component of the convective region. The technique used in this study attempts to include such grid columns by defining the forward edge of the sampling boundary from thresholds of reflectivity and reflectivity gradient associated with these cells at mid-levels.

The sampling boundary between the convective region and the transition zone also required objective definition as the extent of each is often somewhat ambigous in PPI displays, and may not be well represented as being linear. The rear sampling boundary of the convective region was thus defined through reflectivity thresholding at low-levels. This approach was chosen in an attempt to focus on the high-reflectivity signature of convective downdrafts at low-levels, while eliminating grid columns exhibiting lesser reflectivity which may be a part of the adjacent transition zone.

To facilitate this dual-level approach to defining the horizontal boundaries of the convective region, a mesoscale rectangular box was first drawn around the region of interest on horizontal plots of the reflectivity field. Care was taken to ensure the box was large enough to encompass the features of interest at both low and mid-levels, yet not to include cells ahead of or behind the convective region which were not an integral part of the line. The portion of the convective line within the box was then separated into forward and rear components by a linear boundary bisecting the area of high reflectivity at both low and mid-levels, in the along-line direction as indicated in Fig. 17 for the west lobe at 0144 UTC. The forward portion of this sampling template then included all points, at some mid-level, forward of this linear boundary, which met the specified thresholds of 30 dBZ reflectivity and/or 1.5 db km^{-1} reflectivity gradient. Sensitivity of the results to this choice of parameters is discussed in Chapter VI. The rear component of the sampling template then included all points, at low-level, rearward of the linear boundary, which met the specified threshold of 30 dBZ reflectivity. These two horizontal areas at different levels were then "merged" together along the linear boundary to create a single horizontal sampling template. Boundaries were then extended vertically from the edges of the merged template to enclose all grid points in the grid columns encompassed by the template. An example of the CEDRIC functions used to create the template and sample the vertical velocity field is given in Appendix A.

While preliminary sensitivity analyses were accomplished using 80 km and 100 km length sampling templates, the sampling templates used in the actual analyses of area-
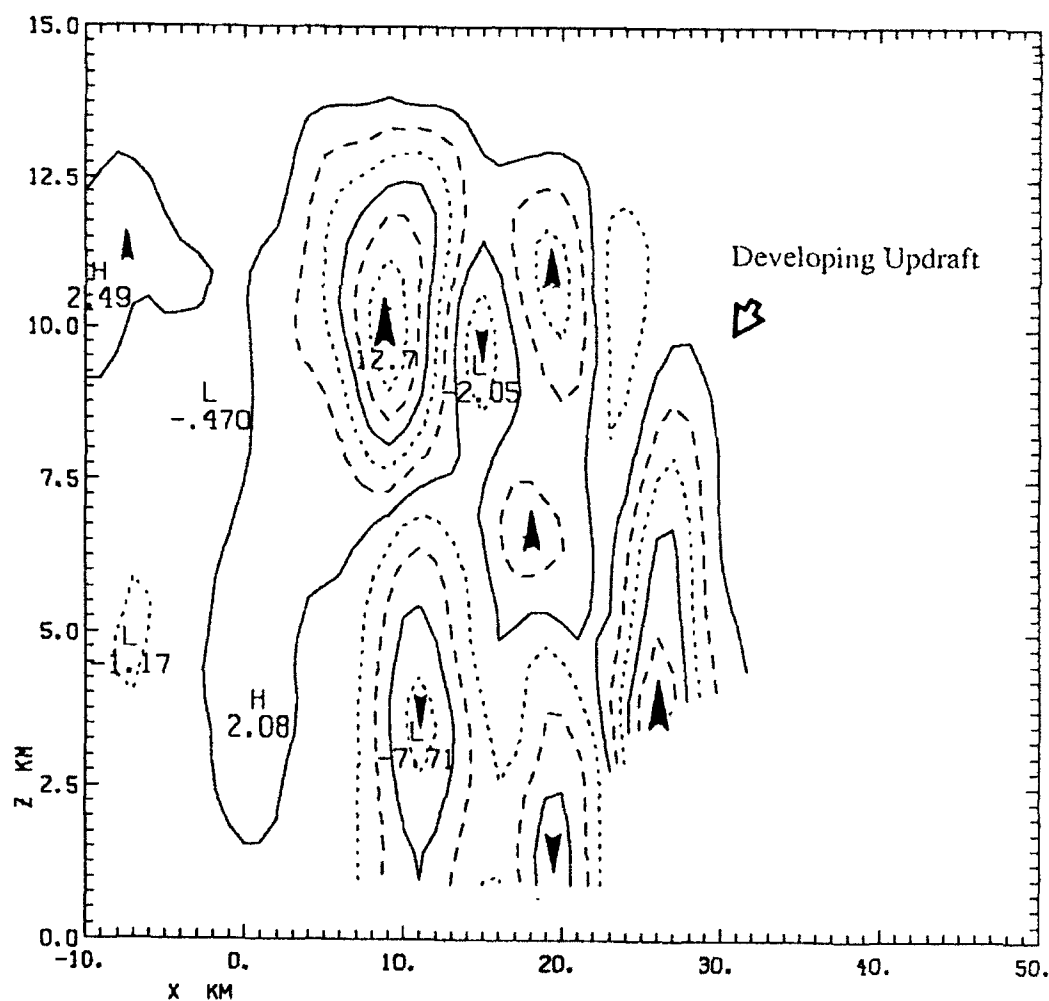
Figure 16. Vertical cross-section of vertical velocities through the convective region along Y = 32 km at 0144 UTC. Vertical velocity contours are: -11 ms^{-1} (solid), -9 ms^{-1} (long dashed), -7 ms^{-1} (dotted), then repeating; -5 ms^{-1} (solid), -3 ms^{-1} (long dashed), -1 ms^{-1} (dotted), +1 ms^{-1} (solid), +3 ms^{-1} (long dashed), +5 ms^{-1} (dotted), +7 ms^{-1} (solid), +9 ms^{-1} (long dashed), and +11 ms^{-1} (dotted). Velocity maxima are indicated. Storm motion is left to right.
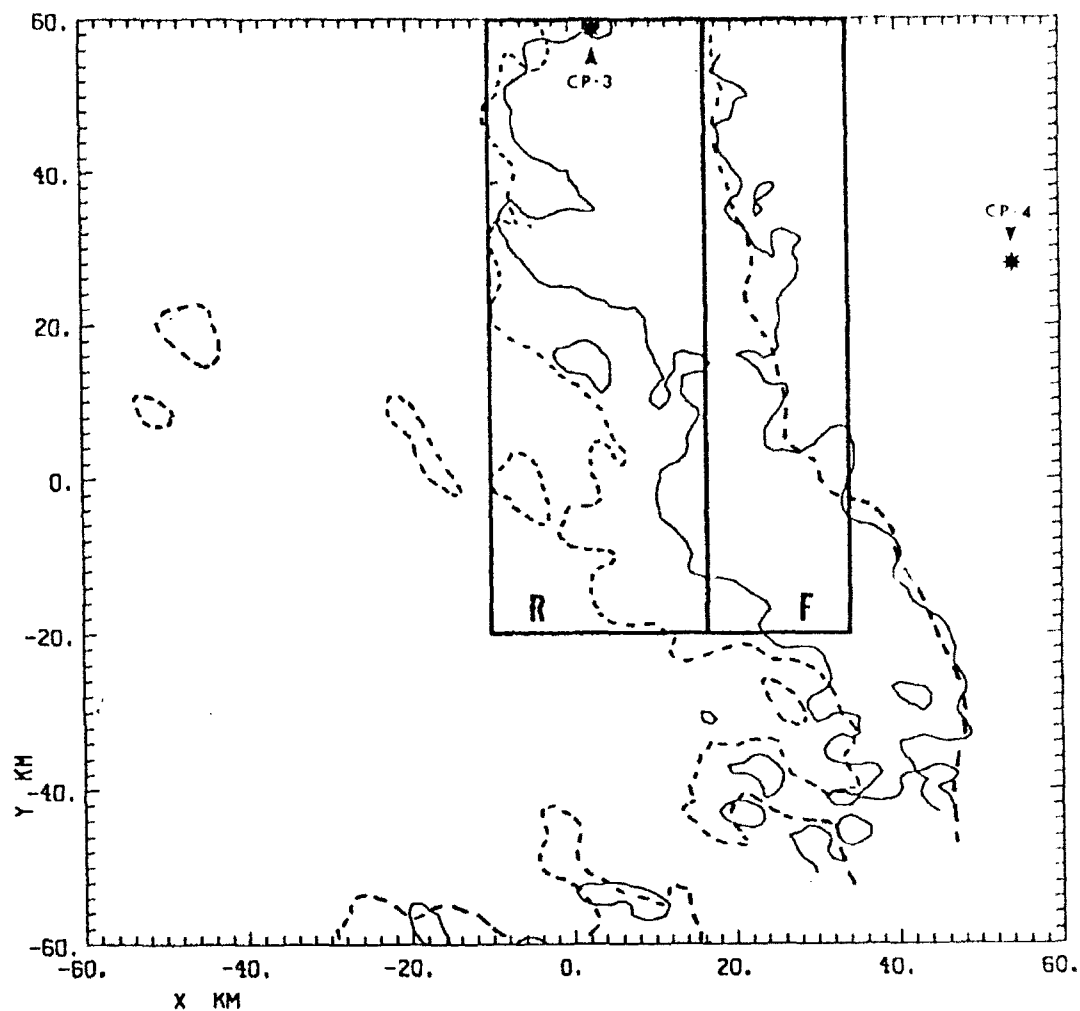
Figure 17. Plan view of radar reflectivity at 0144 UTC showing dual-level (5.9/1.9 km) horizontal sampling template. Solid contours indicate 30 dBZ reflectivity at 5.9 km. Dashed contours indicate 30 dBZ at 1.9 km. The forward component of the template is derived in area F and the rear component in area R (further explanation given in text). The locations of the 5-cm NCAR Doppler radars are shown. Storm motion is left to right.

averaged vertical velocities were subsequently reduced to a 50 km length along-line section of the convective line. This was done to avoid sampling bias caused by attenuation and radar geometry. A more thorough discussion of the sensitivity of the results to this restriction is contained in Chapter VI.

Once the dual-level (5.9/1.9 km) horizontal sampling templates were constructed, they were used to sample the vertical velocity fields at the respective analysis times. Mean vertical velocity and reflectivity values were calculated for the area defined by the sampling template at each grid level from 0.9 km to 14.9 km at 0.5 km vertical intervals. The resulting data are recorded in Appendix B. The means at each grid level were used to construct the vertical profiles of area-averaged vertical velocity and reflectivity discussed in Chapter V.

To gain further insight into the sources of variability in the profiles of area-averaged vertical velocity, histograms of the magnitudes of vertical velocity, across all grid points at each grid level, were computed for each analysis time. Separate histograms were computed for upward and downward velocities with 1 ms^{-1} resolution in order to better examine the relative variations in each. To filter out the effect of change in sign by those points with vertical velocities near zero, the histograms were computed in exclusion of those points with vertical velocity magnitudes less than 1 ms^{-1}. Histograms were constructed at 1 km vertical intervals from 0.9 km to 13.9 km. Those from 0.9 - 11.9 km are contained in Appendix C; those at higher levels begin to reflect the upper boundary condition used in the downward integration of the anelastic continuity equation and provide little useful information concerning the variation in convective vertical velocity.

Finally, vertical cross-sections of reflectivity, vertical velocity, and line-normal storm-relative flow were constructed to aid in determining if changes in the internal circulation of the squall line may be related to variations in the profiles of area-averaged vertical velocity. The cross-sections were oriented perpendicular to the convective line along the x and z-axes to examine the cross-line components of these fields. The cross-sections of all fields were taken at 3 km intervals (one-half of the wavelength with with which the wind fields were filtered) in the along-line (y) direction over the length of the sampling area (50 km).

CHAPTER V

RESULTS

Volume-Averaged Vertical Velocity

The volume-averaged vertical velocities sampled over the convective region are summarized in Table 3. The values of mean vertical velocity (w) indicated are those calculated over the three-dimensional spatial volume defined by the sampling template at each analysis time. The number of grid points used to define the convective region is also given in Table 3. While the number of grid points comprising the convective region did change slightly with time, the dual-level nature of the sampling template helped minimize the fluctuations. The greatest change in the volume covered by the convective region occurred between 0134 and 0144 UTC, with about a 25% increase in the sampling domain. The change in the sampling domain was also associated with an apparent change in the characteristics of the volume-averaged vertical velocity. A progression is apparent in the magnitude of mean vertical velocity as it increased steadily from 0122 UTC to the maximum of 1.64 ms^{-1} at 0134 UTC, then rapidly decreased to 1.06 ms^{-1} ten minutes later at 0144 UTC. A steady decrease is then noted to a minimum at 0159 UTC before rebounding slightly at 0205 UTC. This progression in mean vertical velocity was followed systematically by a progression in the standard deviation of vertical velocity. This pattern of an increase and then a rapid decrease in w and the standard deviation of w is highly suggestive of a period of development and then decay of the convection within the sampling box. To investigate this further, the evolution of the horizontal area-averaged vertical velocity was examined.

Evolution of Area-Averaged Vertical Velocity at Mid to Upper-Levels

The area-averaged vertical velocity at each grid level was plotted as a function of height for each analysis time to produce the profiles of area-averaged vertical velocity shown in Fig. 18. As noted with the mean vertical velocity over each of the analysis volumes (Table 3), the profiles suggest an evolution of the strength of convection over the analysis period. Both the magnitude and height of the peak in mean vertical velocity are observed to increase from 0122 UTC through the 0134 UTC analysis, decrease rapidly by 0144 UTC, continue decreasing through 0159 UTC, and finally increase slightly again by 0205 UTC. In addition to the progression of the height and magnitudes of the peak in mean vertical velocity, the vertical depth of the peak at mid to upper-levels is greatest at 0134 UTC.

Table 3. Summary of volume-averaged vertical velocity data for each analysis volume using the dual-level (5.9/1.9 km) horizontal sampling template.

Doppler Analysis Time (UTC)	Doppler Lobe	N (template)	Mean w (ms^{-1})	Std Dev (ms^{-1})	Min w (ms^{-1})	Max w (ms^{-1})	N (volume)
0122	West	1,903	1.17	3.46	-11.3	20.5	41,908
0129	West	1,710	1.58	3.63	-11.9	27.2	38,322
0134	West	1,595	1.64	3.67	-11.3	21.5	38,477
0144	West	2,046	1.06	2.81	-10.6	17.5	47,567
0153	West	2,020	0.84	2.63	-9.3	14.2	45,939
0159	West	1,952	0.59	2.27	-9.6	14.6	47,693
0205	West	1,865	0.72	2.59	-10.9	23.7	43,632

Template thresholding:
  Front component: > 30 dBZ reflectivity or 1.5 dB km^{-1} reflectivity gradient at 5.9 km
  Rear component: > 30 dBZ reflectivity at 1.9 km

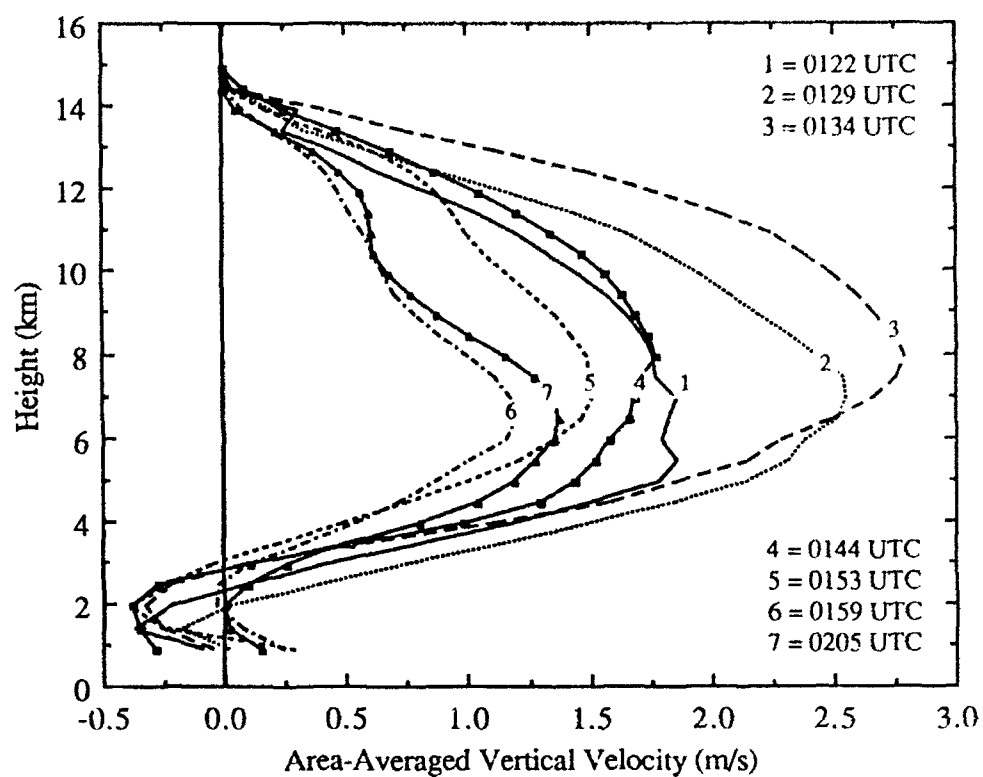N = number of grid points w = vertical velocity Std Dev = standard deviation of w

Figure 18. Profiles of area-averaged vertical velocity for 0122 - 0205 UTC.

indicating that the vertical drafts were deepest and strongest at that time. It is also interesting to note the high degree of similarity between the characteristics of the profiles from the first three analyses, and the similarity between the last three analyses.

A similar temporal progression is noted in the profiles of variance of the vertical velocity fields (Fig. 19). The peak in variance increases both in magnitude and height from 0122 UTC to 0134 UTC before dropping off sharply at 0144 UTC, indicating that the magnitudes of the mid and upper-level updrafts and downdrafts have weakened dramatically over this ten minute period. The profiles of variance also reflect the apparent strengthening of the vertical drafts by 0205 UTC as the profile peak again increases in height and magnitude over that at 0159 UTC. Again, as noted in the profiles of mean vertical velocity, a strong similarity exists between the profiles of the variance in vertical velocity from the first three analyses, and between those of the last three analyses.

Another interesting point is that the peak variance in vertical velocity is generally located at a slightly higher level than the peak in vertical velocity except at 0159 UTC, when convection appears weakest, the two peaks are both located near 6 km. Moreover, the highest variance in vertical velocity is located at mid to upper-levels instead of lower levels where it may be expected due to the coexistence of developing updrafts, and the downdrafts induced by evaporative cooling and water-loading. However, the low-level variance might also be affected by inability of the Doppler radars to sample the lower portions of the developing cells where precipitation-size hydrometeors would be absent.

To further elucidate the variations noted in the profiles of area-averaged vertical velocity, histograms of vertical velocity magnitudes were calculated (Appendix C). The histograms of the horizontal distribution of vertical velocity further corroborate what the profiles of area-averaged vertical velocity suggested: that there appears to be notable evolution of the convection within the sampling region. At all levels it is apparent that the spectral width of the area-averaged vertical velocity distribution narrows with time after 0134 UTC. Additionally, most of the variability of the vertical velocity spectrum can be attributed to upward velocities and not downward velocities. This seems to suggest that the strengths of the downdrafts do not depend so much on the strength of the updrafts (at least beyond some critical threshold at which enough condensate is produced to initiate a convective downdraft).

To more objectively describe the variations in vertical velocity, the magnitudes of both upward and downward velocities were categorized as "weak" ($1 - 3$ ms^{-1}), "moderate" ($3 - 6$ ms^{-1}), and "strong" (> 6 ms^{-1}). Grid points with |w| less than 1 ms^{-1} were eliminated from the histogram sampling to concentrate on the changes associated with
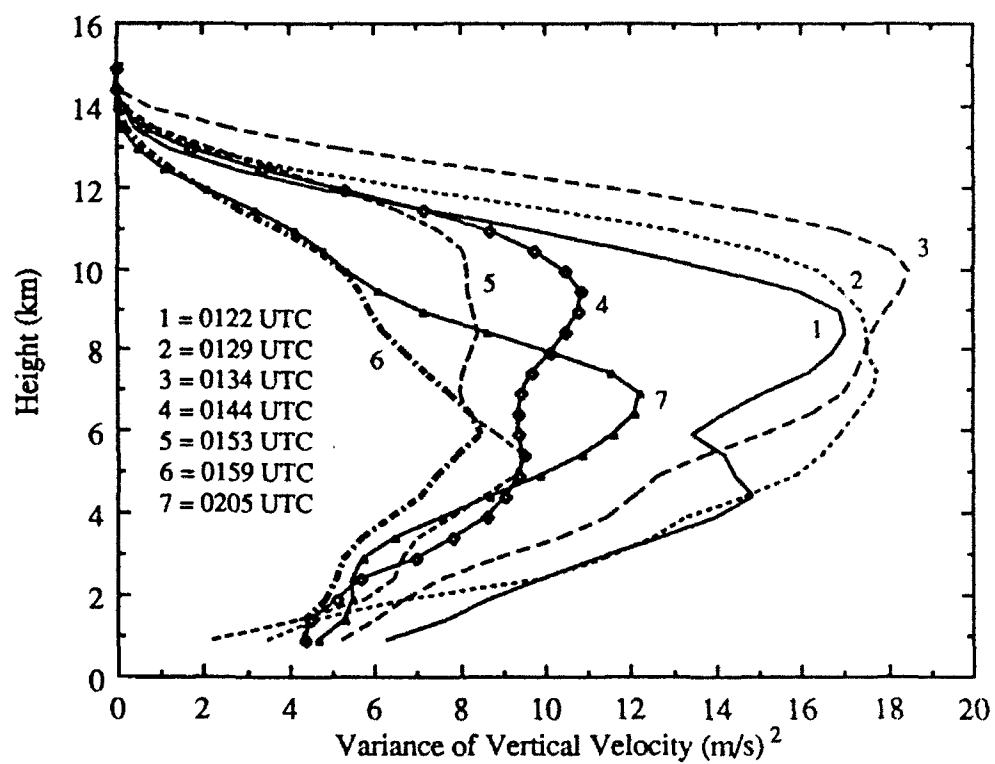
Figure 19. Profiles of variance of the vertical velocity fields for
0122 - 0205 UTC.

stronger vertical motions. However, these grid points were part of the area-averaged vertical motions shown in Fig. 18 and part of the calculated variances shown in Fig. 19.

While some moderate decrease in the distribution of downward vertical velocities is noted through time, the spectral width of this population is less than that of the updrafts at all times and altitudes. Relatively few strong downdrafts were found through the analyses. On the other hand, the variation in the distribution of upward velocities was much more dramatic than that of the downward velocities. A trend in the distribution of upward velocities was found with a strong, wide distribution in the first three analyses, a significantly narrowed distribution at 0144 UTC, and a slightly more narrowed distribution at 0153 and 0159 UTC. A slight resurgence in upward vertical velocity strength at was observed at 0205 UTC.

These trends at mid to upper-levels are illustrated by the histograms of vertical motion at the 7.9 km level. The first three analysis times are well represented by the 0134 UTC histogram shown in Fig. 20. The upward velocities are nearly equally distributed between the weak/moderate/strong categories with a distribution of 31/29/40%. The downward velocities were distributed with 82% weak, 18% moderate, and no grid points associated with downdrafts greater than 6 ms^{-1}. Ten minutes later at 0144 UTC (also Fig. 20) the fraction of strong upward velocities had dropped to 15% while the portions of moderate and weak upward velocities both increased. Additionally, slight increases in the populations of moderate and strong downward velocities were found. By 0159 UTC (Fig. 21) weak upward velocities comprised only 7% of the population as the fraction of weak upward velocities had grown to 60%. Little additional change had occurred in the distribution of downward velocities since 0144 UTC. At 0205 UTC (also Fig. 21) little additional change was noted in the 7.9 km histogram except for a slight increase in the number of strong upward vertical velocities as the convective activity appeared to slightly strengthen.

The population of strong updraft velocities was also found to follow a fairly orderly transition of height and magnitude with time. The maximum area covered by strong upward motion increased in size and was found at increasingly higher altitudes from 0122 to 0134 UTC. The largest proportion of area covered by strong vertical motion was 43% at 8.9 km in the 0134 UTC analysis.

An additional interesting feature noted in the histograms (computed in exclusion of grid points with |w| < 1 ms^{-1}) is the mean ratio of the number of grid points with upward velocities to the number of grid points with downward velocities, at each level. The ratio varied from 1.12 at 0.9 km, to 0.73 at 1.9 km, 1.00 at 2.9 km, 1.79 at 3.9 km, 2.59 at
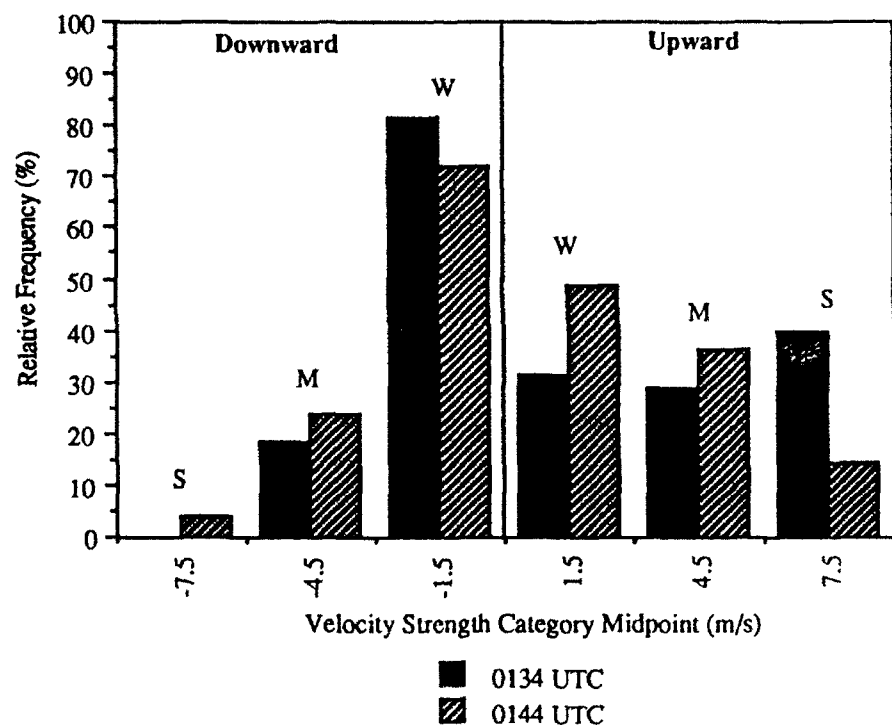
Figure 20. Histograms of vertical velocity distribution at 7.9 km height for 0134 and 0144 UTC. Relative frequency of upward and downward velocities are calculated separately. Velocities with magnitude < 1 m/s have been omitted. W = weak, M = moderate, and S = strong.
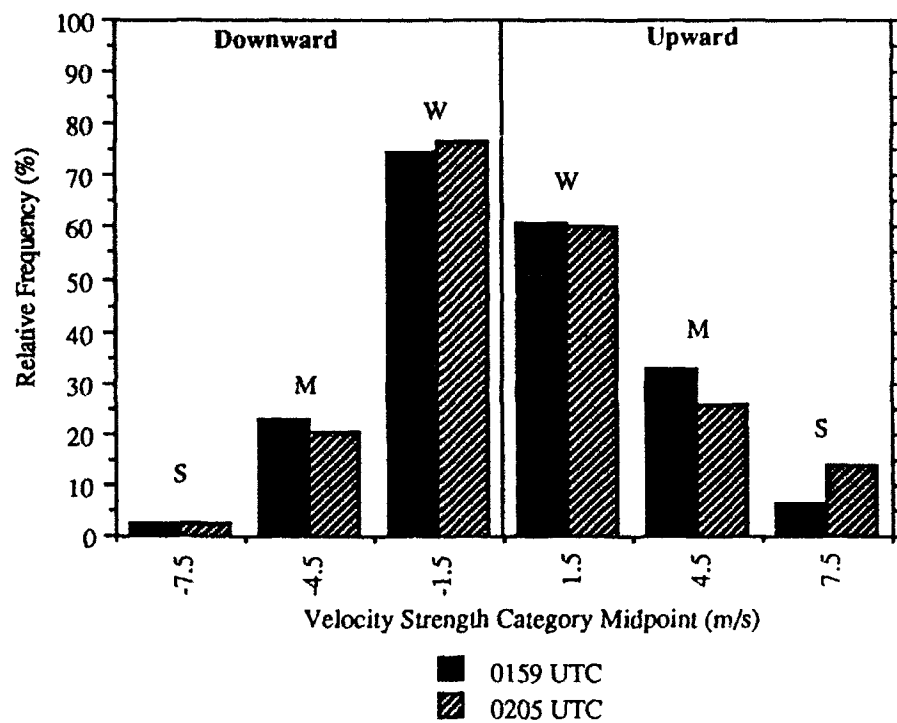
Figure 21. As in Fig. 20 except for 0159 and 0205 UTC.

4.9 km, 3.31 at 5.9 km, 3.50 at 6.9 km, 3.1 at 7.9 km, 2.63 at 8.9 km, 2.51 at 9.9 km, 2.49 at 10.9 km, 2.98 at 11.9 km, and 6.47 at 12.9 km. The ratio points out that the area covered by ascending air was approximately 2 - 3 times greater than descending air above 2.9 km altitude.

Finally, examination of the vertical cross-sections reflects what is evident in the profiles and histograms of vertical velocity. Figure 22 shows a cross-section of vertical velocity at 0134 UTC which is fairly typical of the first three analysis periods. The vertical velocity field at these times is characterized by very strong, deep updrafts accompanied by moderate, deep downdrafts at the mid to upper-levels. The well-developed updrafts frequently carry reflectivity maxima into the mid to upper troposphere as indicated in the accompanying cross-section of reflectivity (Fig. 23).

Ten minutes later, at 0144 UTC, the corresponding cross-section of vertical velocity (Fig. 24), taken 6 km up the convective line to partially compensate for along-line movement of the individual cells, indicates a dramatic weakening of the convective drafts. The drafts have become much more shallow with weaker vertical velocities, and have a lower cross-sectional profile of reflectivity (Fig. 25). It must be noted here that the 0144 UTC radar volume scan was the only one during the period of analysis which used a 360° scanning strategy (see Table 2). As a result, the resolution of the data are less than that at the other analysis times. Nevertheless, it remains apparent that a dramatic change has taken place in the convective region since 0134 UTC.

The continued weakening of the convection within the sampling box after 0144 UTC is apparent in the representative cross-sections from 0159 UTC, which had the same resolution as that at 0134 UTC. Weak to moderate updrafts still are prevalent in the vertical velocity field (Fig. 26). The drafts are not as deep or well-defined as in the first three analyses. The accompanying cross-section of reflectivity (Fig. 27) shows the profile of 30 dBZ reflectivity to be broader horizontally and lower in vertical extent than the previous analyses, indicating the weaker state of convection.

By 0205 UTC, the corresponding cross-section of vertical velocity (Fig. 28) indicates a strengthening of the updrafts, particularly at mid-levels as was noted in the histograms at the 7.9 km level. The depth of the convective cells is also increasing as a slight resurgence appears to be occurring. The increasing strength of the updrafts is also apparent in the accompanying cross-section of reflectivity (Fig. 29) which shows the height of the 30 dBZ contour increasing while a reflectivity maxima along the leading edge of the line has been carried aloft by a 15 ms^{-1} updraft.

Figure 22. As in Fig. 16 except for Y = -3 km at 0134 UTC.

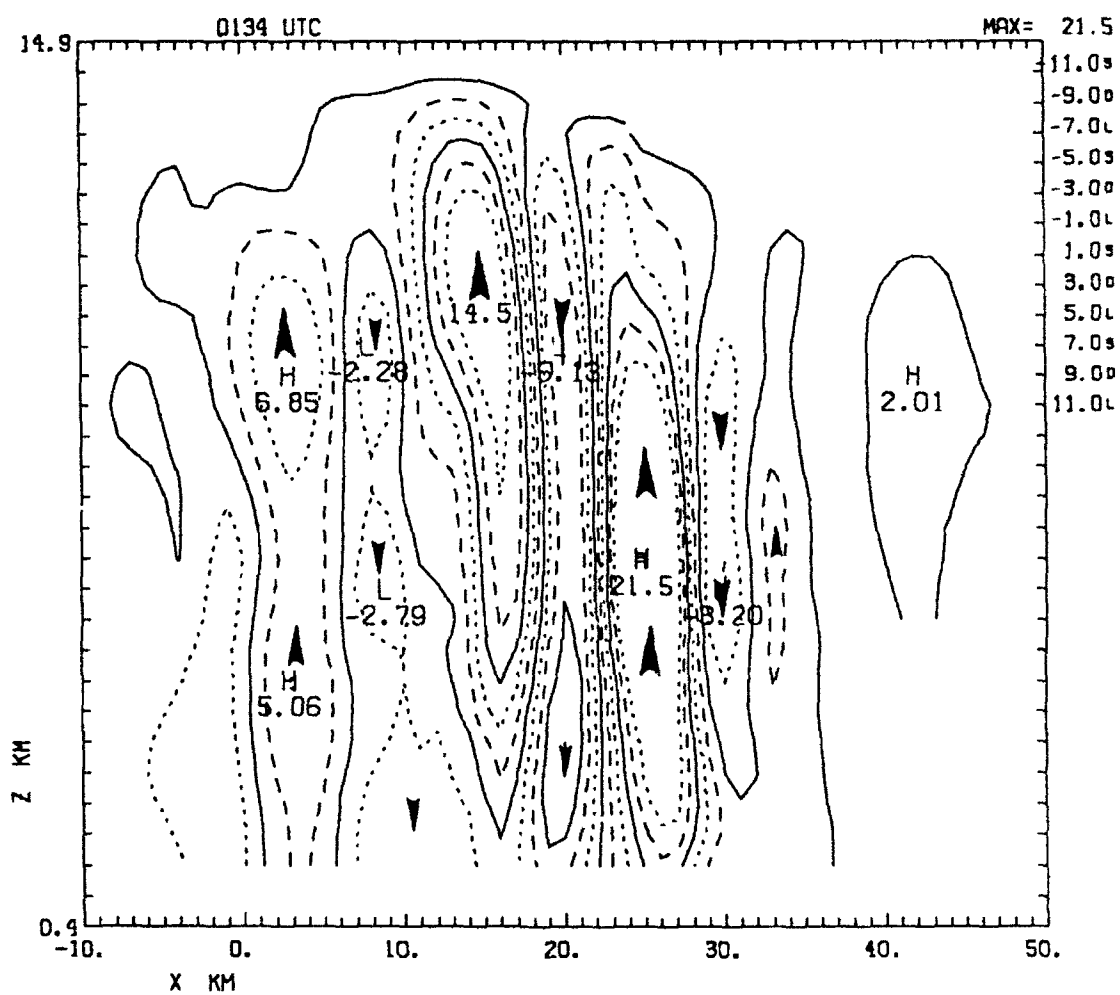Figure 23. As in Fig. 15 except for Y = -3 km at 0134 UTC.

Figure 24. As in Fig. 16 except for Y = 3 km at 0144 UTC.

Figure 25. As in Fig. 15 except for Y = 3 km at 0144 UTC.

Figure 26. As in Fig. 16 except for Y = 3 km at 0159 UTC.
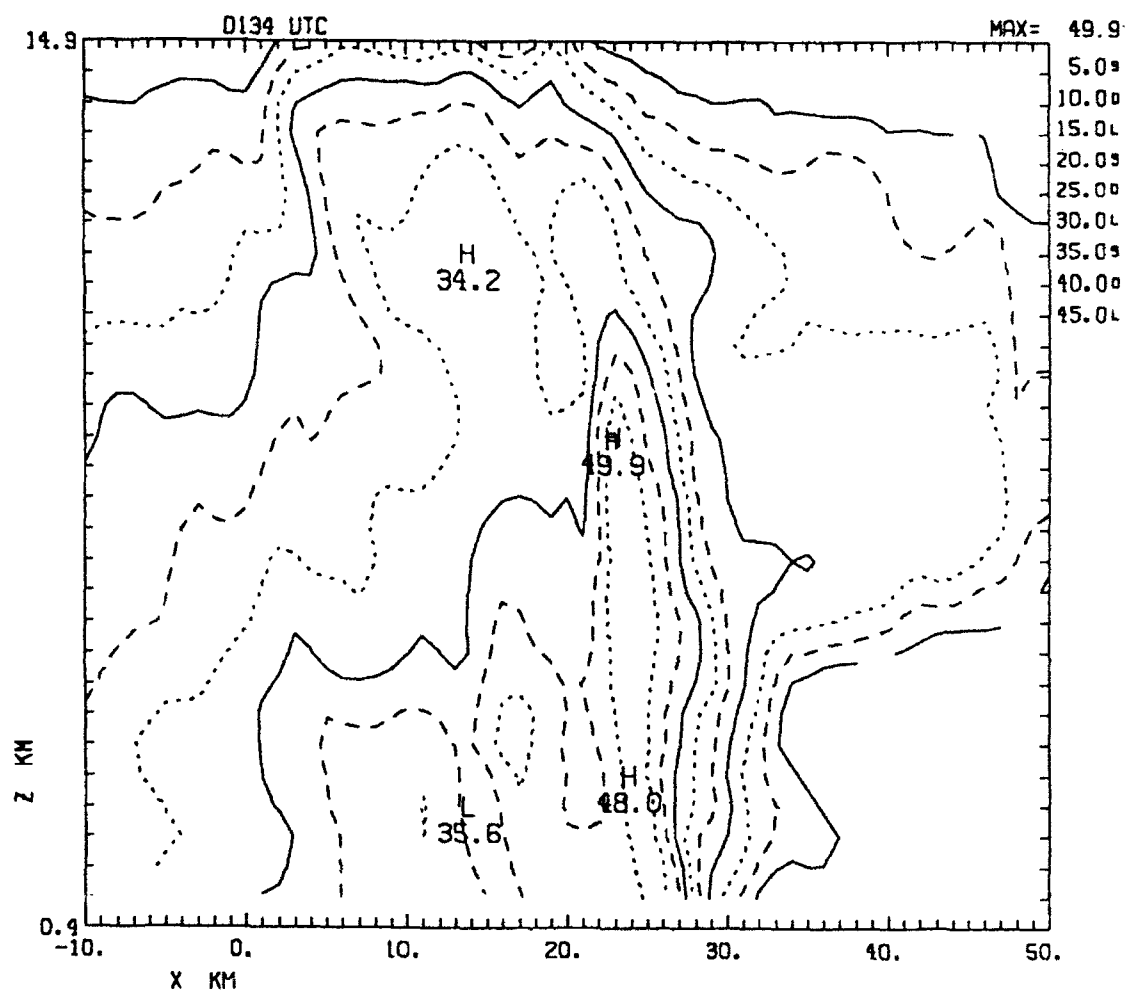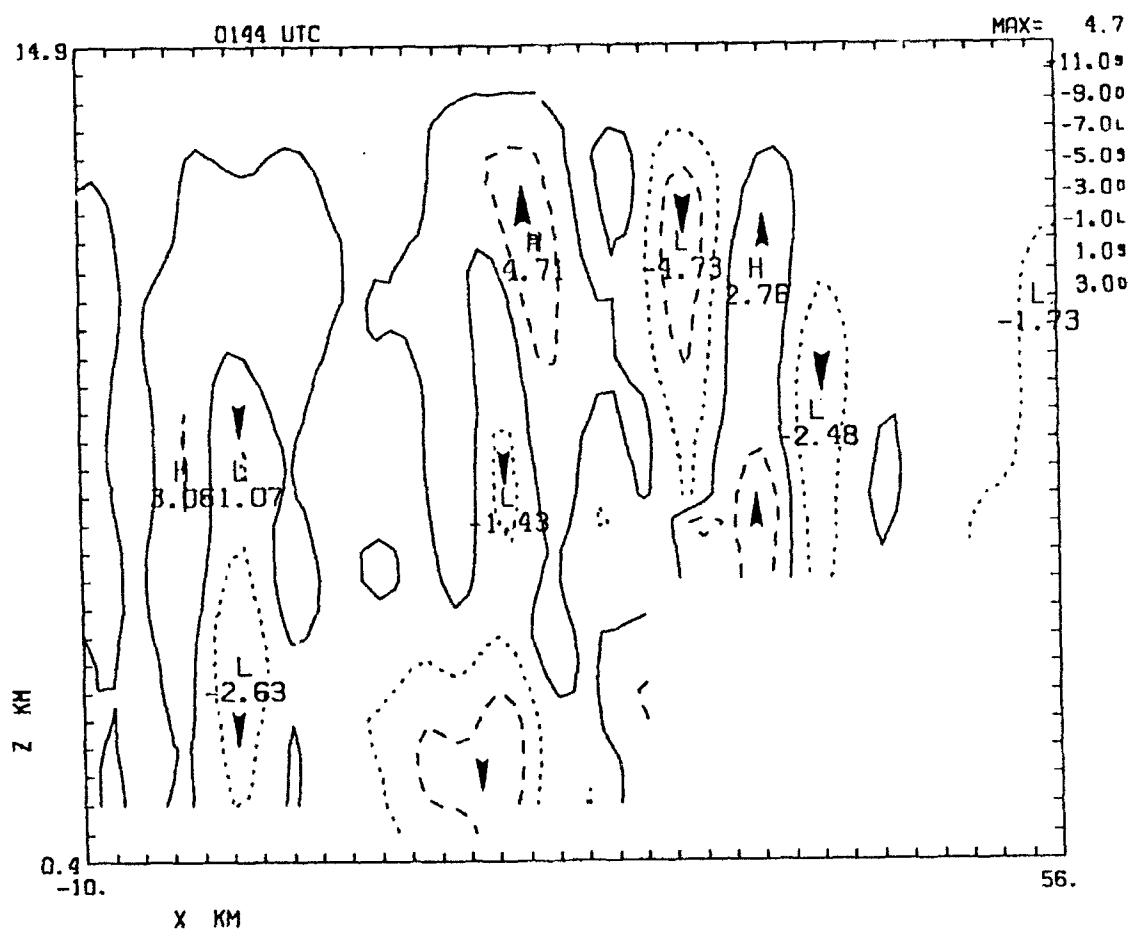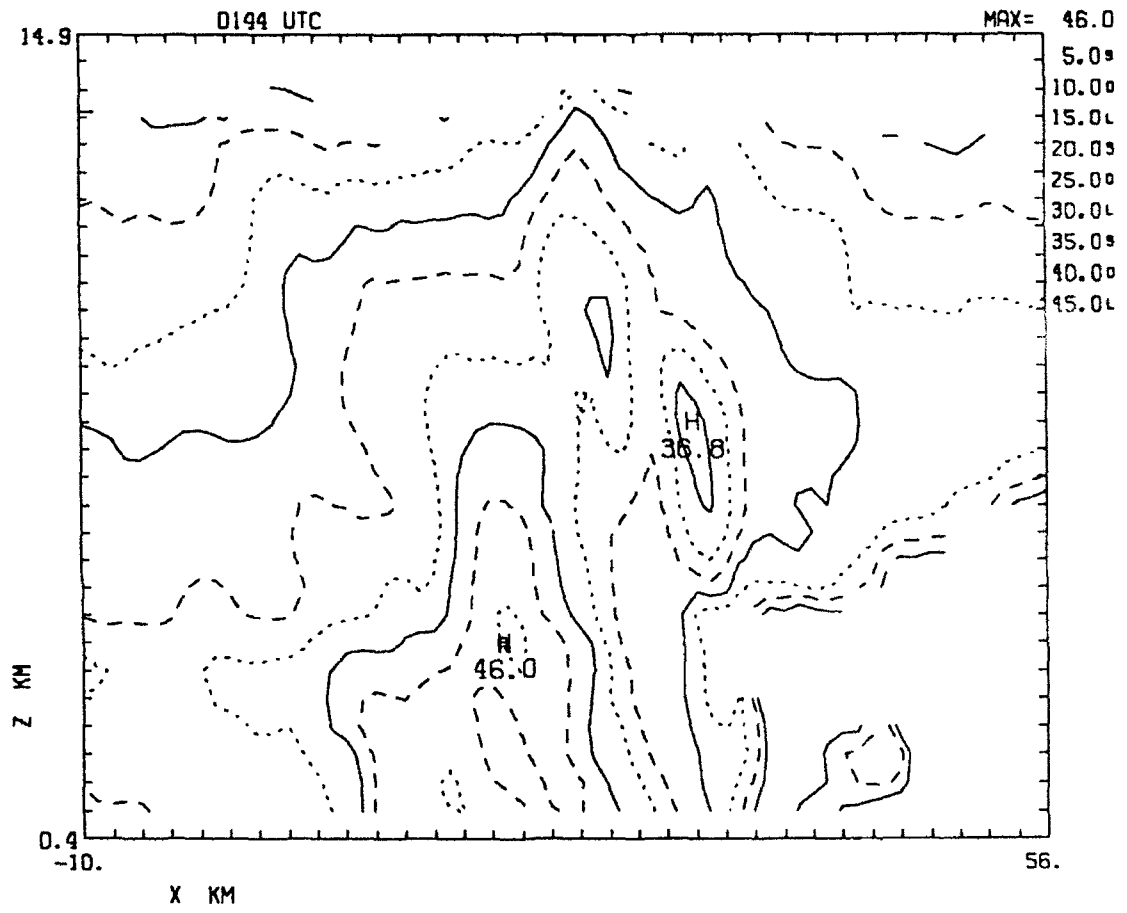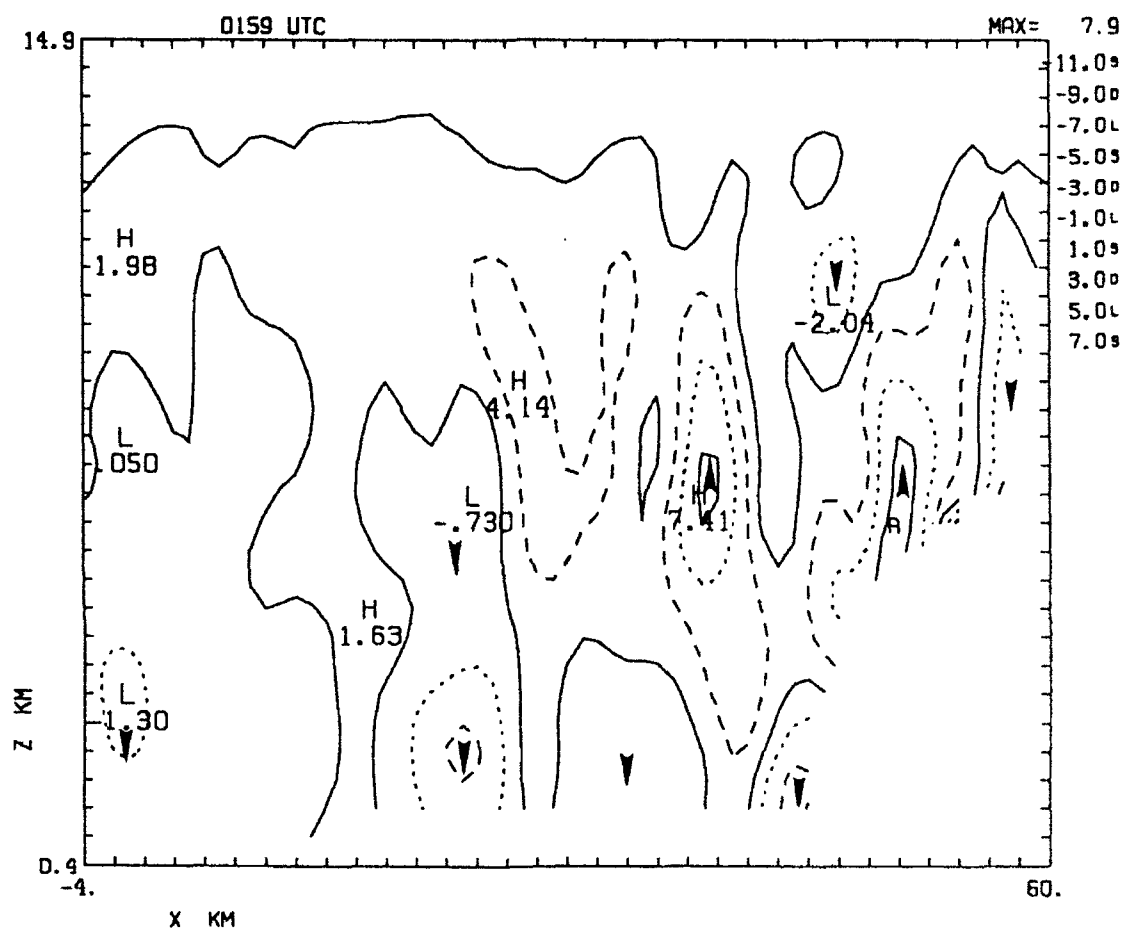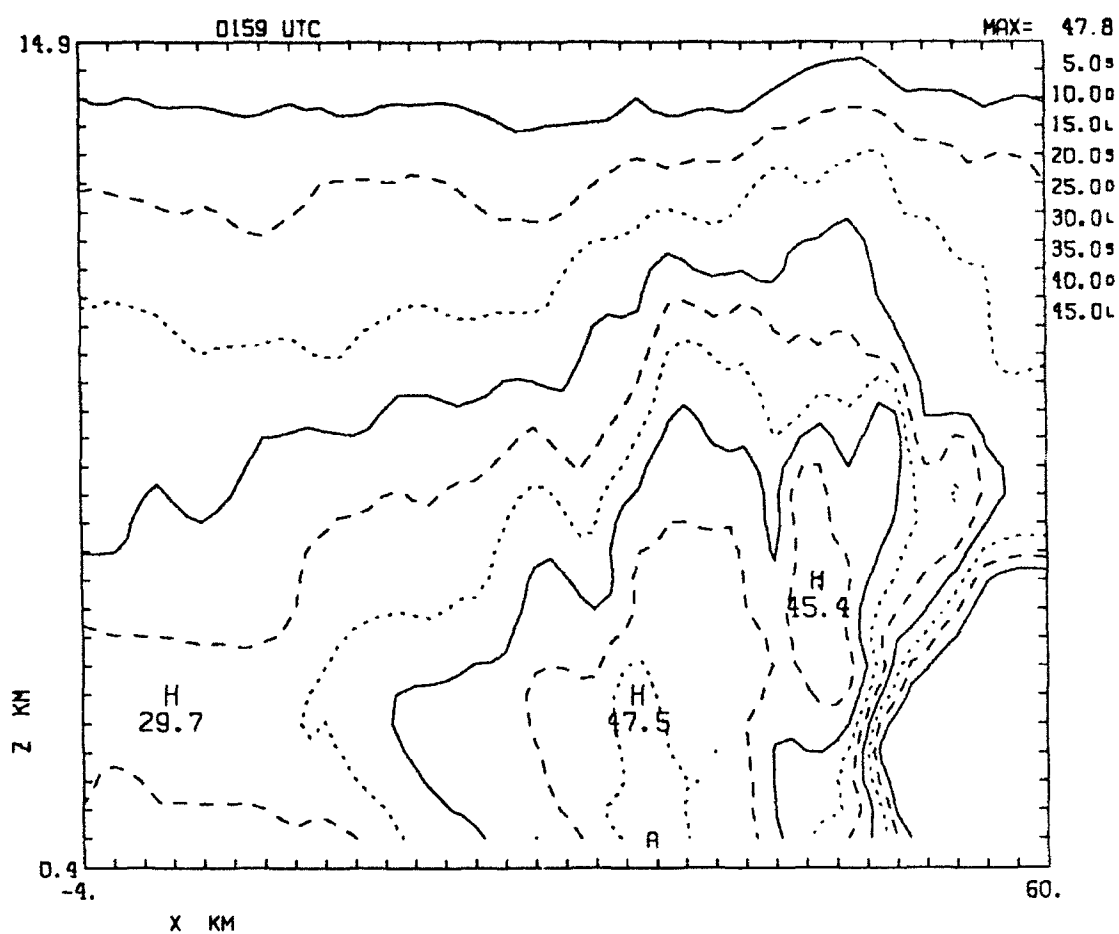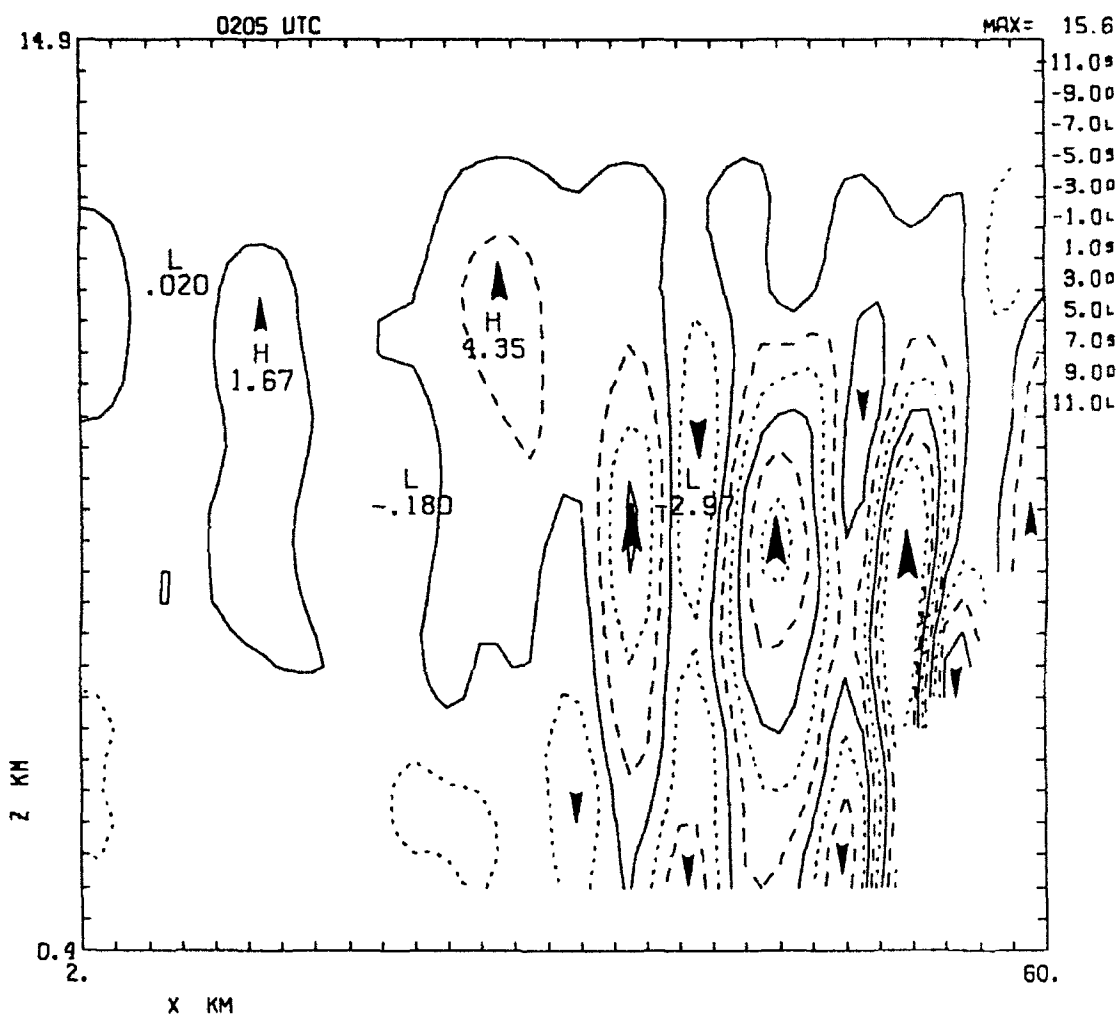
Figure 27. As in Fig. 15 except for Y = 3 km at 0159 UTC.
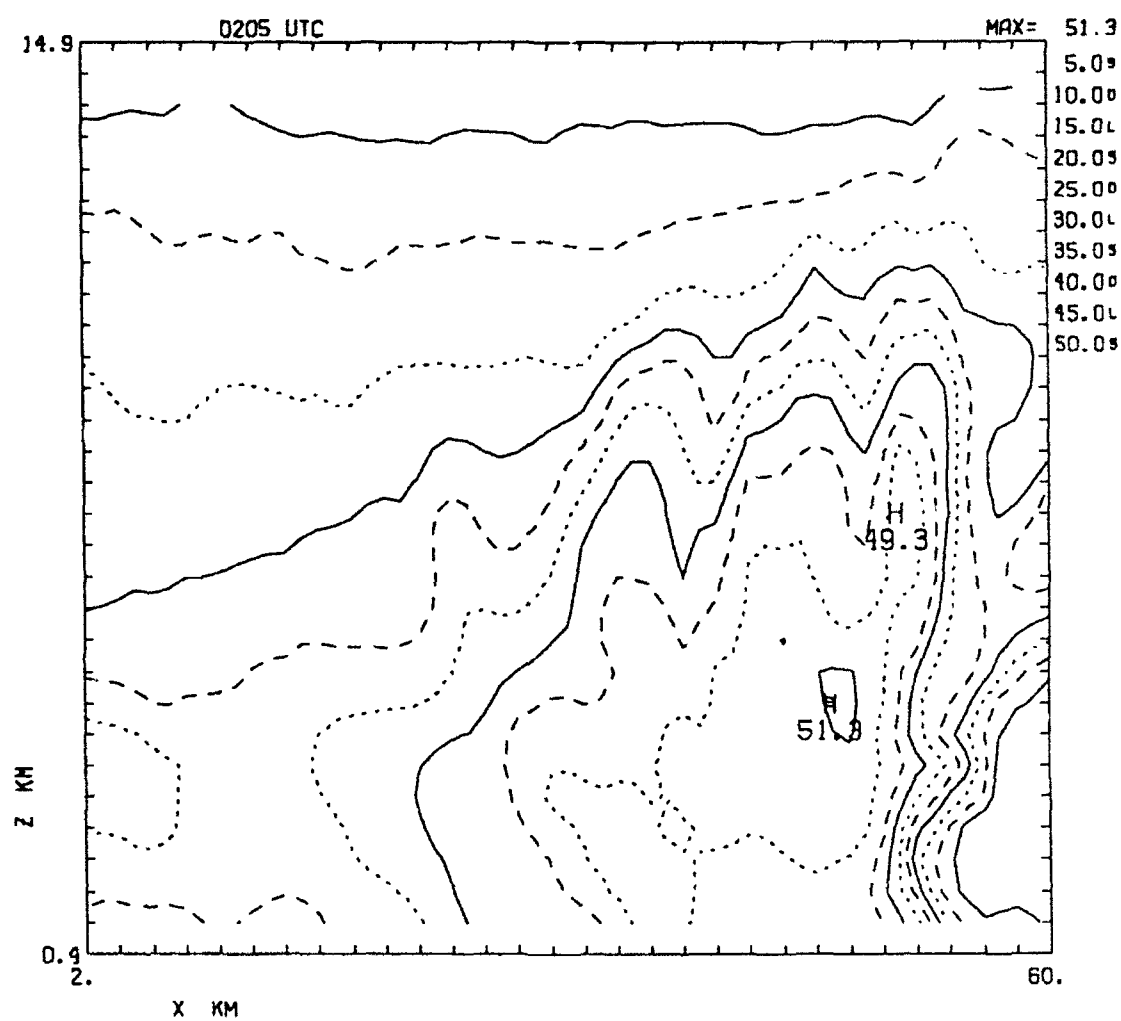
Figure 28. As in Fig. 16 except for Y = 6 km at 0205 UTC.

Figure 29. As in Fig. 15 except for Y = 6 km at 0205 UTC.

Profiles of area-averaged reflectivity were also created to gain further insight into the structure of the convective region, and for comparison to the variations noted in the vertical velocity fields. The results are shown in Fig. 30. The interesting feature at mid-upper levels is that although all the profiles follow the same general form, reflectivity in the upper levels appears to decrease by several dB with time as the updrafts weaken and are not carrying as many large precipitation particles into the mid and upper troposphere. Additionally, the profiles of reflectivity all converge uniformly at about 6.4 km altitude where it is obvious that all precipitation particles have frozen. The temperature at this level was approximately -15 °C. While an explanation is beyond the scope of this study, it is interesting to note that while the distributions of vertical velocity changed dramatically over the period of analysis, the level at which all particles froze appeared to remain quite steady.

The mean vertical velocities over the analysis volumes, the profiles of area-averaged vertical velocity and reflectivity, the histograms of vertical velocity, and the cross-sections of vertical velocity and reflectivity, all appear to indicate that a dramatic transition has occurred in the convective region during the period of analysis. A striking similarity exists in the profiles and cross-sections from the first three analyses, while those from the last three analyses are also similar to each other but markedly different from the first three analyses. The vertical drafts were strong and deep through 0134 UTC but weakened and became more shallow by 0144 UTC. Further weakening is evident through 0159 UTC before a slight resurgence at 0205 UTC.

This transition from a stronger to a weaker state over a mesoscale area appears quite similar to the behavior of the convection in the numerical modelling studies conducted by Fovell and Ogura (1988) and Rotunno et al. (1988). Moreover, as observed in both models, the transition occurred on the order of five hours after the initiation of convection. It does not appear that the temporal variations are simply being driven by convective-scale evolution within the sampling box. Were this the case, more variation between consecutive analysis times might be expected as the evolution of individual cells would not likely be in phase. Furthermore, the character of the convective drafts noted in the cross-sections appears to vary systematically over the mesoscale sampling box between analysis times, rather than on a random basis as may be expected for variation driven on a purely convective scale.
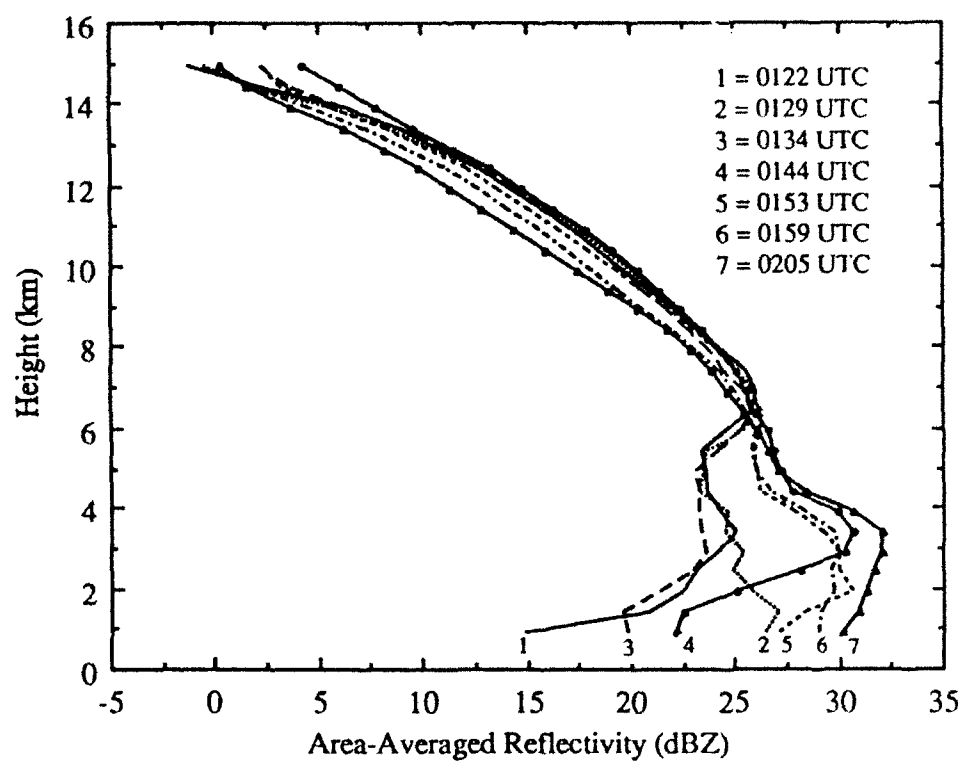
Figure 30. Profiles of area-averaged reflectivity for 0122 - 0205 UTC.

Evolution of Area-Averaged Vertical Velocity at Low-Levels

The area-averaged vertical velocities over the lowest 4 km are shown in Fig. 31. As noted at mid to upper-levels, the profiles from the first three analyses are quite similar to each other yet distinct from those of the last three analyses.

Above 3 km the earlier profiles all indicate net ascent which is stronger than that of the last three analysis times. However, the lowest 2.5 km is typified by net descent at nearly all times. The deepest layer of net descent occurs from 0134 UTC through 0153 UTC which is slightly lagging behind the occurrence of maximum updrafts at mid to upper-levels in the first three analyses. This net descent is likely due to evaporative cooling and water-loading as by-products of the strong convection occurring at the earlier times. The time of occurrence and the depth of this net descent are suggestive of the strong downdraft which occurred in the Rotunno et al. (1988) model and appeared to mark the transition to a weaker convective state. The resurgence in convection near the end of the analysis period is again apparent in the near-absence of net descent at 0159 and 0205 UTC.

The profiles of variance in the vertical velocity distribution for the lowest 4 km (Fig. 32) also reflect quite clearly the higher variance common to the first three analysis periods, and the similar yet smaller variance of the last three analyses. This is but another indicator that a significant transition in the state of convection has occured during the period of analysis as the distribution of low-level draft strengths has evidently narrowed after 0134 UTC.

The net low-level descent noted from 0134 - 0153 UTC, as well as the similarity of the profiles during this period is reflected in the histograms of vertical velocity from the 1.9 km grid level. At 0134 UTC (Fig. 33) the histograms of upward and downward velocities are nearly symmetric. Also, 5% of the downward velocities at this time are strong while 28% are moderate. Ten minutes later at 0144 UTC (also Fig. 33) the 1.9 km histogram is quite similar and varies by only a few percent. However, by 0159 UTC (Fig. 34) a slight change is noted; the fraction of moderate downward velocities has decreased by 9% while the fraction of moderate upward velocities has increased by 15%. At 0205 UTC (also Fig. 34) the population distribution of downward velocities remains essentially unchanged from that at 0159 UTC but the distribution of upward velocities indicates an increase in the fractions of moderate and strong drafts by 6% and 3%, respectively, as the convective activity has slightly increased.

Examination of the low-level reflectivity structure provides further strong evidence
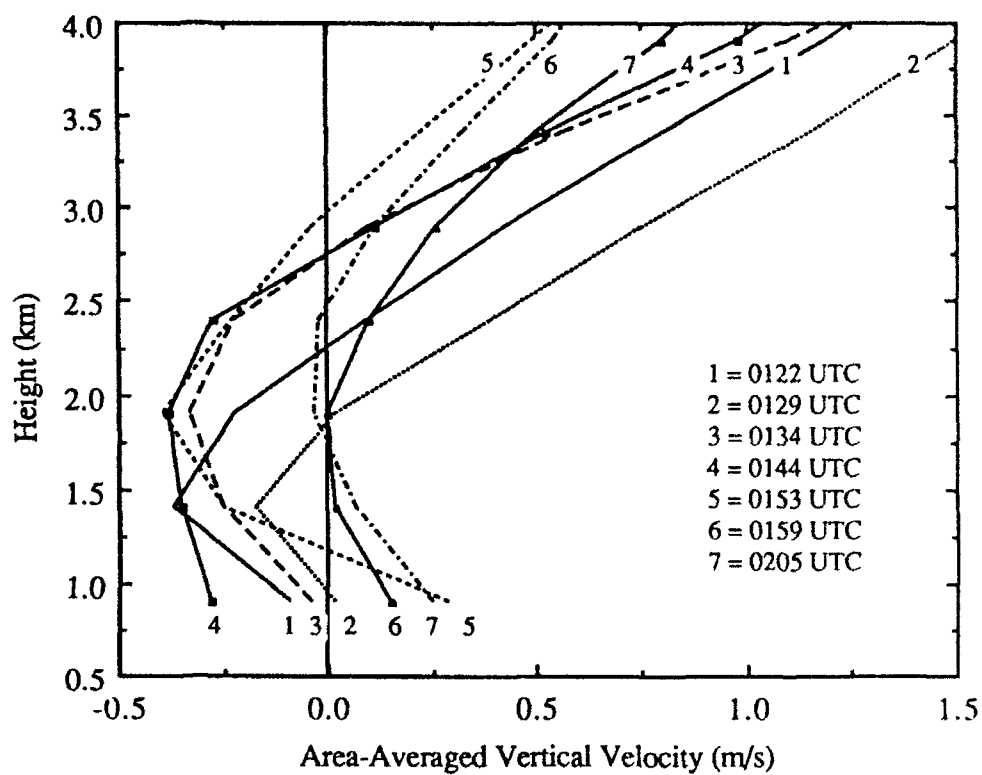
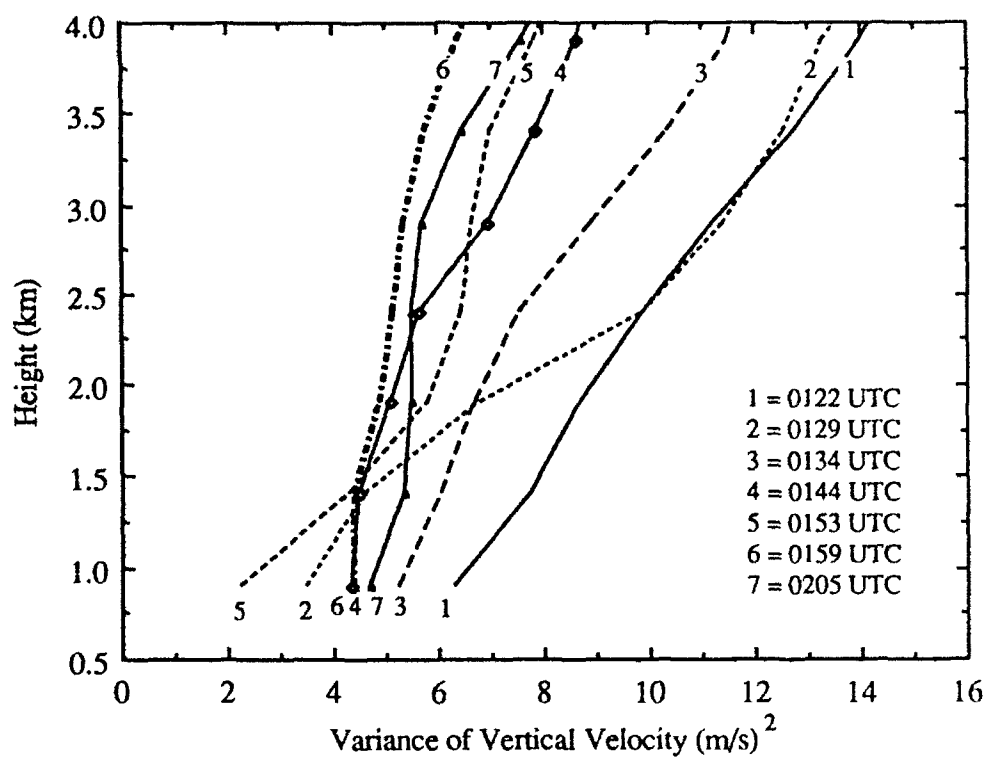Figure 31. As in Fig. 18 except for 0 - 4 km.

Figure 32. As in Fig. 19 except for 0 - 4 km.

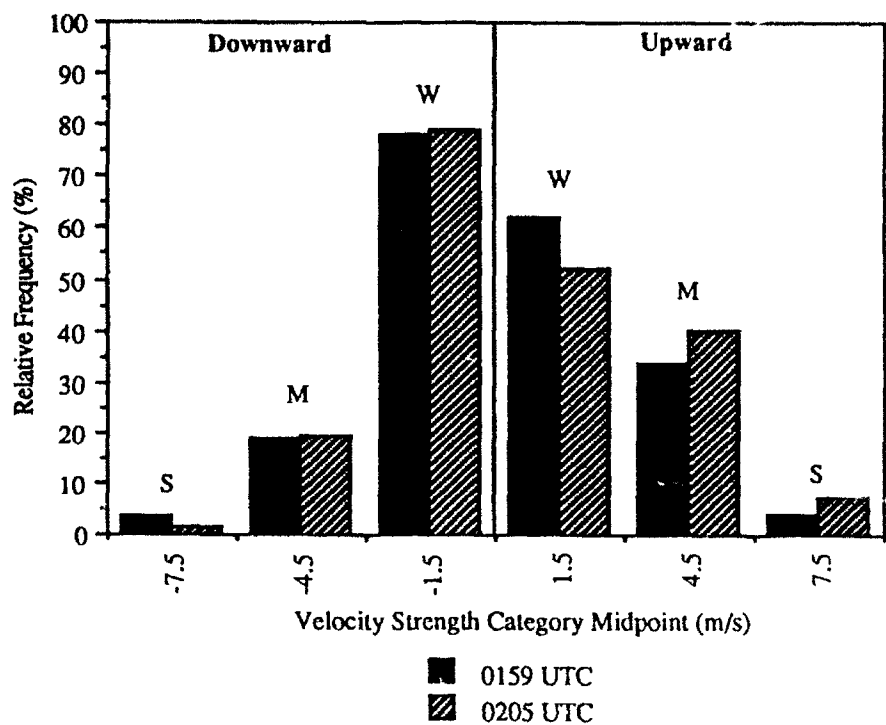Figure 33. As in Fig. 20 except for 0134 and 0144 UTC at 1.9km.

Figure 34. As in Fig. 20 except for 0159 and 0205 UTC at 1.9km.

that some transition has occurred in the convective region. The profiles of area-averaged reflectivity for the lowest 4 km are shown in Fig. 35. When compared sequentially, the profiles are slightly noisy but it appears that there is a basic progression in the increase of low-level reflectivity over the period of analysis. Between 6 and 2 km, a distinct similarity exists between the profiles from the first three analyses and those from the last four analyses. Mean reflectivity between the 2 km and 4.5 km levels increased roughly from 23 - 25 dBZ in the first three analyses to 27 - 32 dBZ in the last four analyses.

This increase in mean reflectivity at low-levels is evidenced by an increase in the number of grid points with reflectivity of at least 30 dBZ, while a decrease is noted in the number of grid points at mid-levels with the same reflectivity. The data in Table 4 indicate for each analysis time the number of grid points at 1.9 km and 5.9 km elevations within the 50 km length sampling template with reflectivity of at least 30 dBZ. At 1.9 km the number of grid points with high reflectivity increased to a maximum at 0159 UTC but the most significant increase was between 0134 - 0144 UTC. Conversely, the number of grid points with high reflectivity at 5.9 km was found to decrease in the latter three analyses which is consistent with the changes noted in the cross-sections of reflectivity.

This change in the reflectivity structure of the convective region is further illustrated by the horizontal plots of 30 dBZ contours at 5.9 km from 0134 UTC (Fig. 36) and 0159 UTC (Fig. 37), and the 1.9 km level at 0134 UTC (Fig. 38) and 0159 UTC (Fig. 39). Over this 25 minute period the area of high reflectivity at 5.9 km appears to narrow along the length of the convective line within the west Doppler lobe. Meanwhile, over the same period, the area of high reflectivity at low-levels appears to broaden significantly along the same length of the convective line. Furthermore, the increase of low-level reflectivity behind the convective line by 0159 UTC is indicative of a rapid increase in the intensity of the stratiform precipitation area during this 25 minute period; as was observed during the transition to a weaker convective state in the numerical simulations mentioned previously.

Changes in Storm-Relative Flow

The typical line-normal storm-relative flow from the first three analyses is fairly well represented by Fig. 40 where a band of inflowing air 3 - 4 km in depth centered at 3.4 km altitude can be seen entering the rear of the convective region. Maxima in this rear inflow are typically near 10 - 12 ms^{-1} and located well behind the primary convection (as seen in the corresponding cross-sections of vertical velocity and reflectivity shown in Figs. 41 and 42. Rear inflow is also frequently observed to extend downward to the surface and
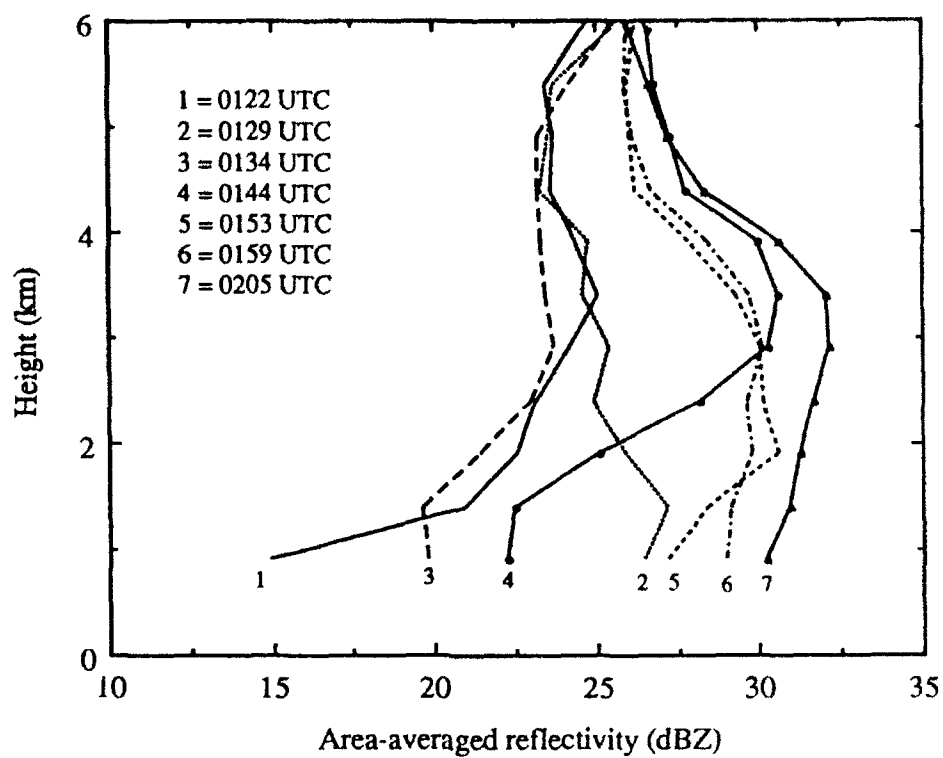
Figure 35. As in Fig. 30 except for 0 - 4 km.

Table 4. Number of grid points within the 50 km length sampling
template with reflectivity at least 30 dBZ.

Doppler Analysis Time (UTC)	Number of grid points at level	
	1.9 km	5.9 km
0122	1,107	1,026
0129	1,230	946
0134	1,279	1,067
0144	1,612	1,089
0153	1,714	974
0159	1,738	836
0205	1,722	628

30 dBZ contours at 5.9 km height
0134 UTC
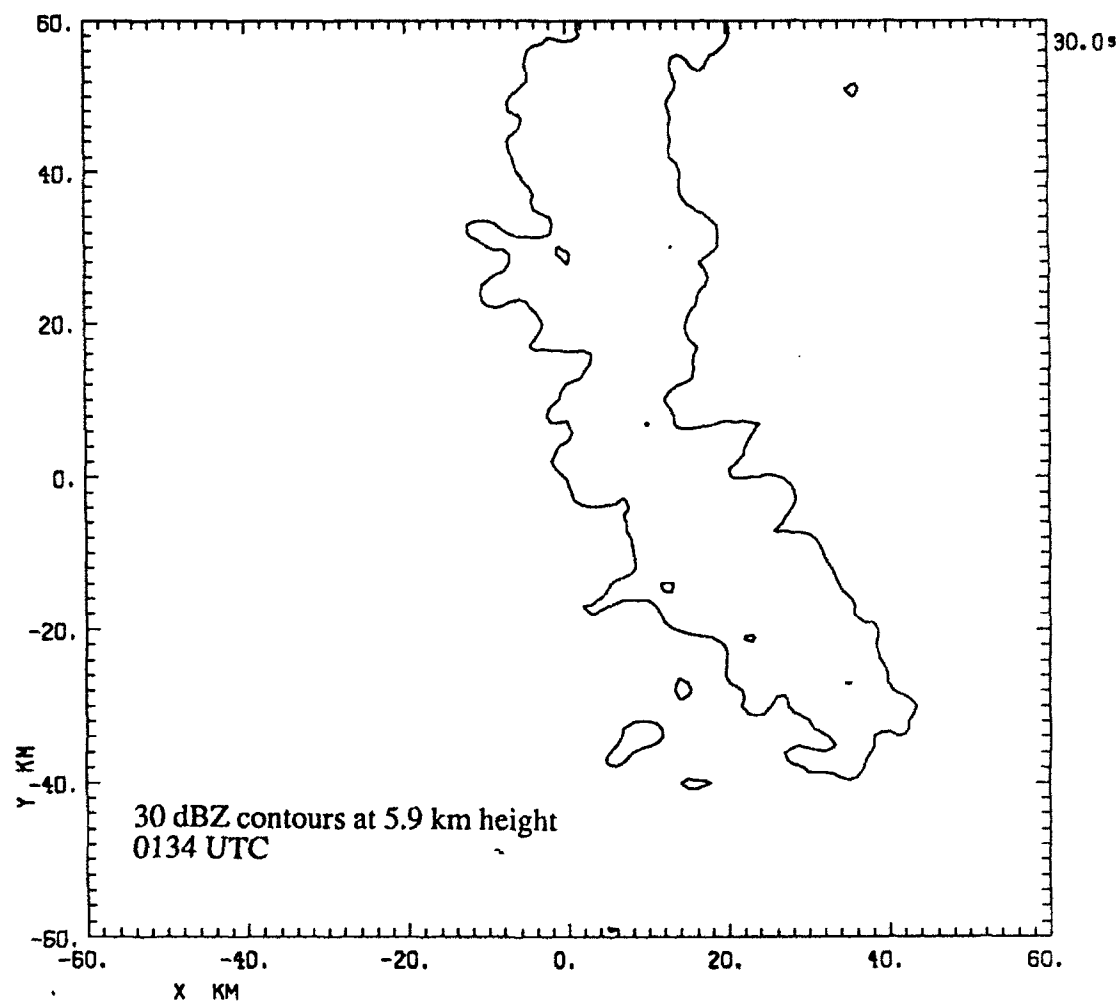
Figure 36. Plan view of 5.9 km 30 dBZ contours at 0134 UTC.

30 dBZ contours at 5.9 km height
0159 UTC

30.0ₛ

Y_KM

X_KM

-60.   -40.   -20.   0.   20.   40.   60.

60.
40.
20.
0.
-20.
-40.
-60.
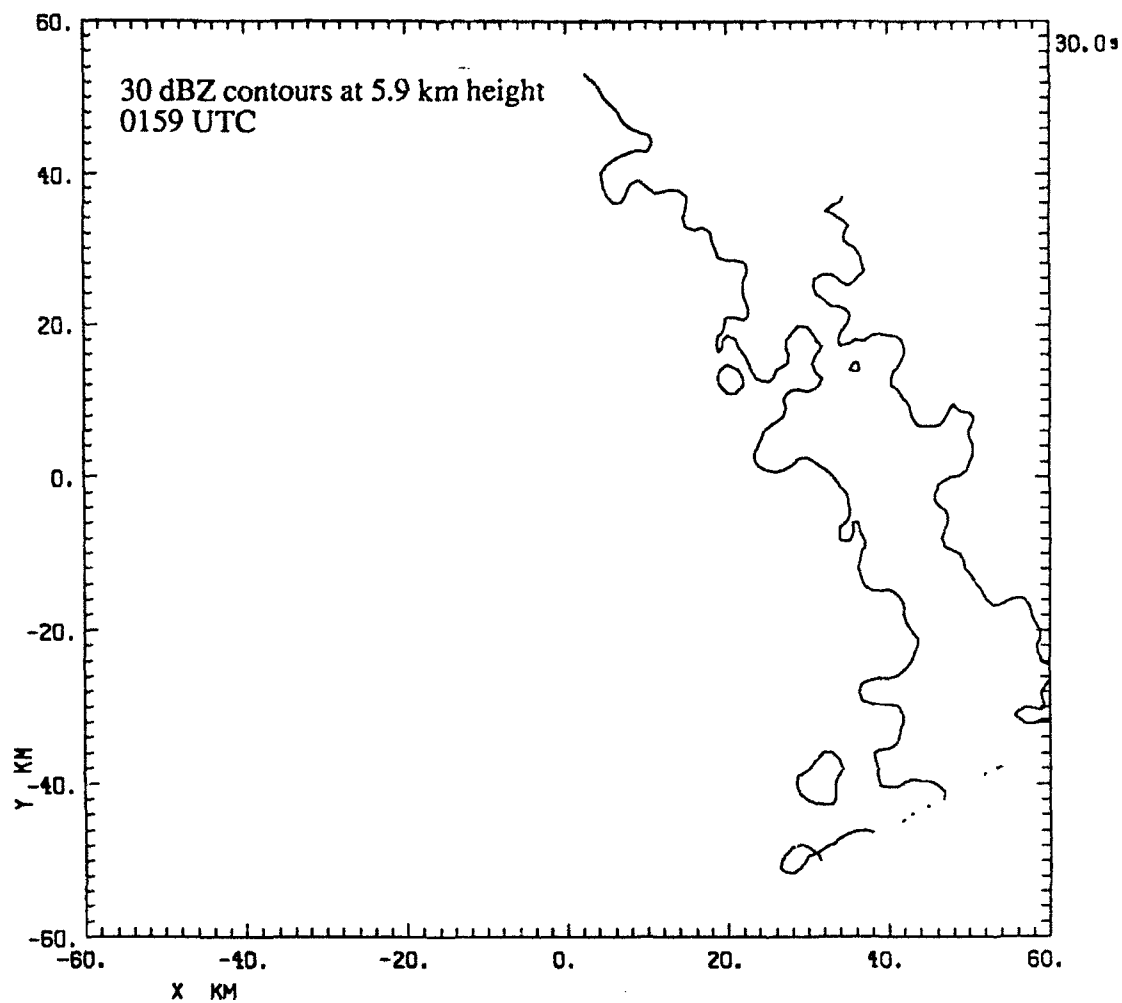
Figure 37. As in Fig. 36 except for 0159 UTC.
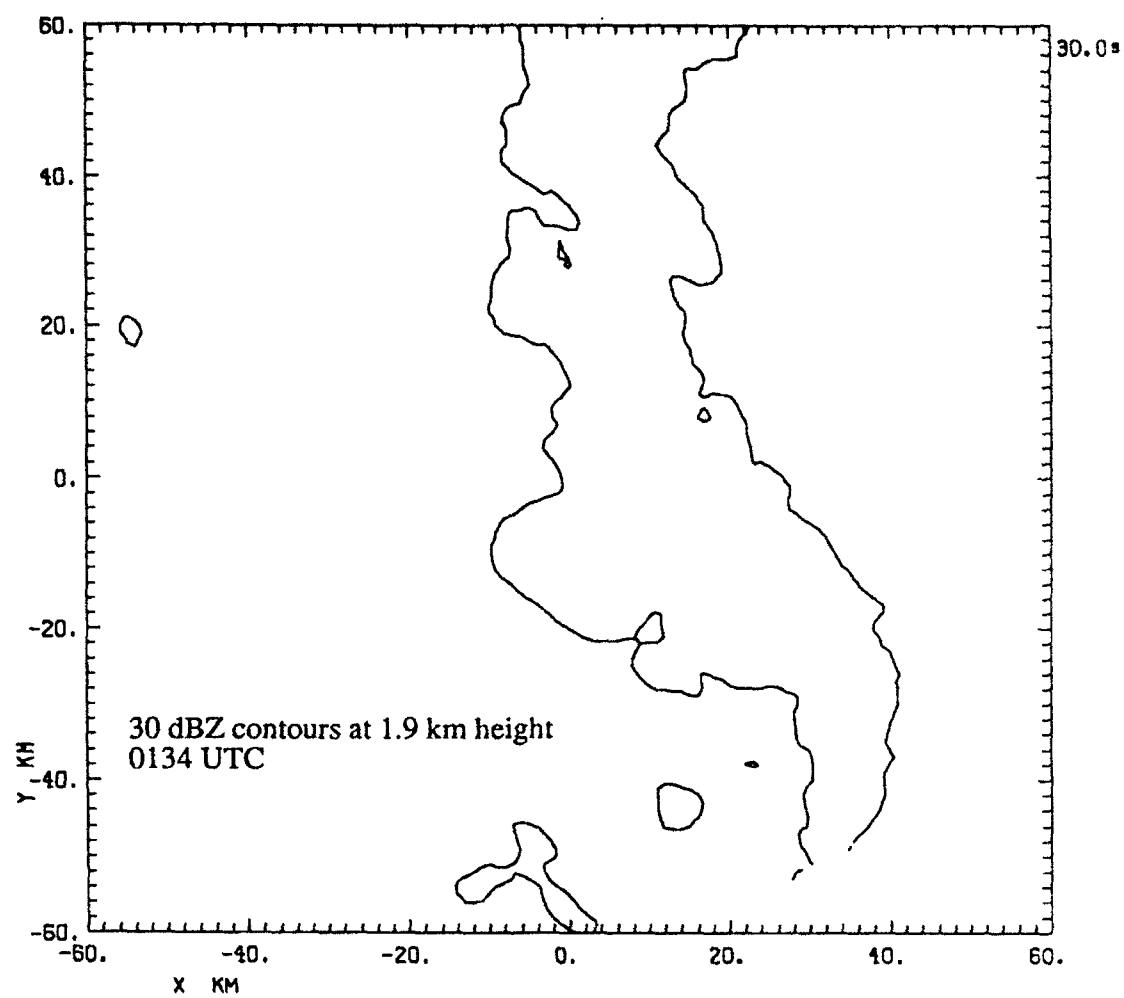
Figure 38. Plan view of 1.9 km 30 dBZ contours at 0134 UTC.
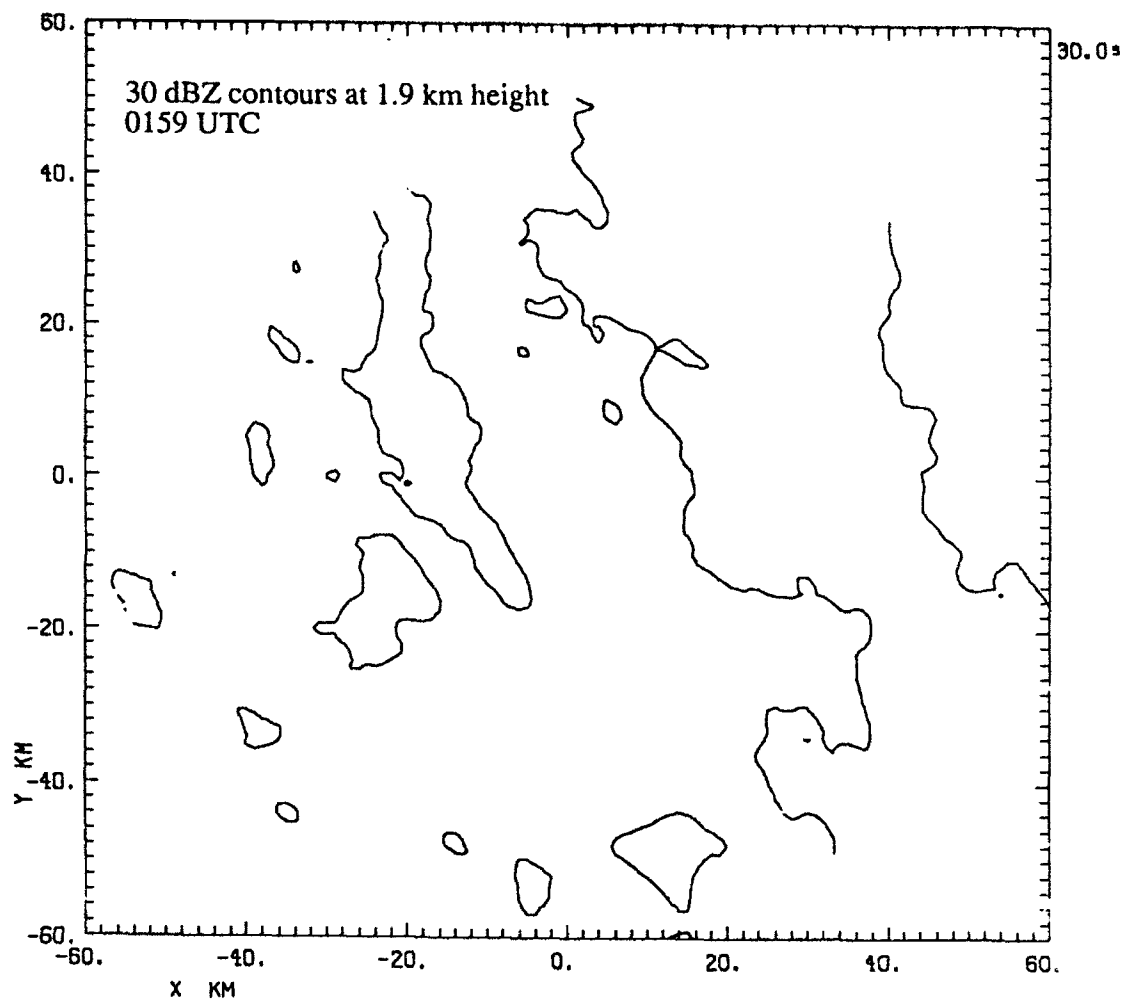
Figure 39. As in Fig. 38 except for 0159 UTC.
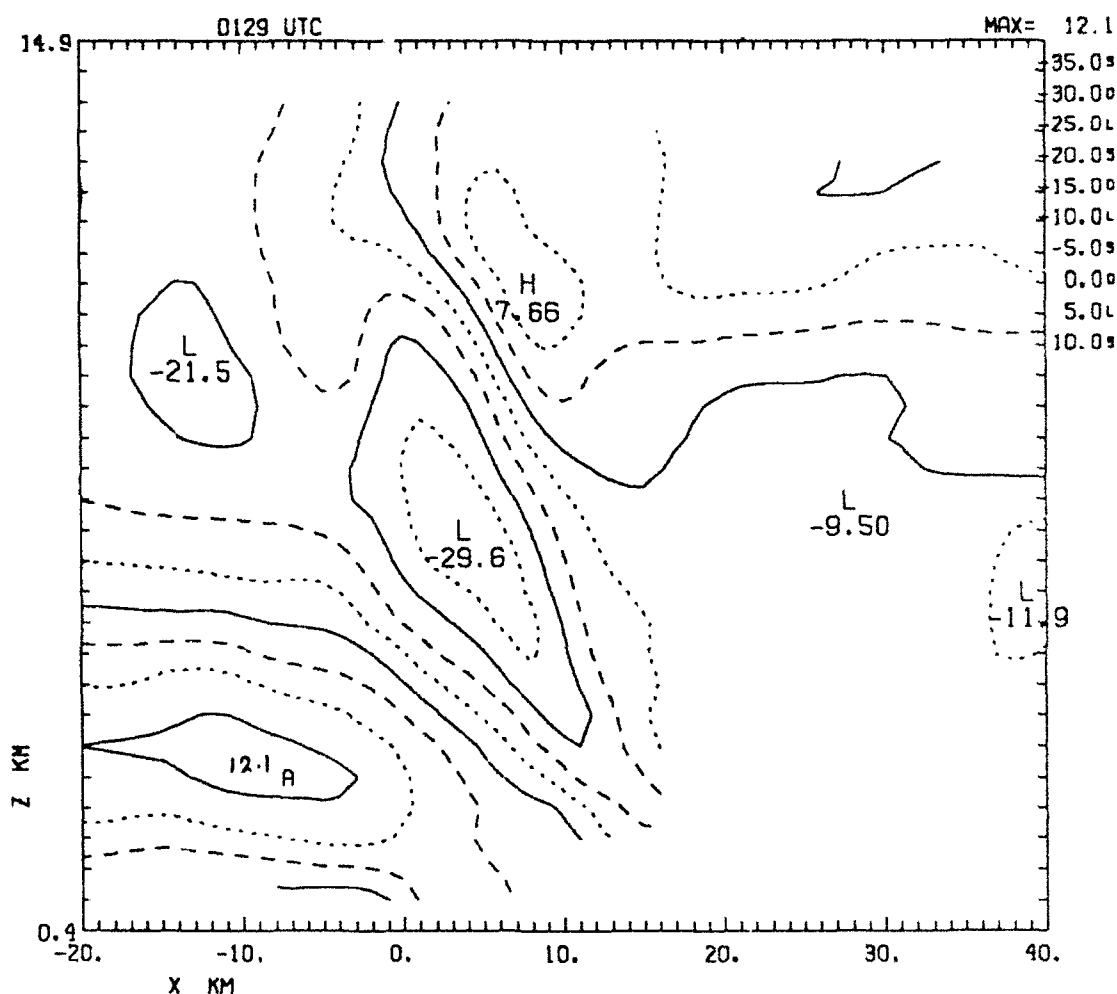
Figure 40. Vertical cross-section of the line-normal storm-relative wind field through the convective region along Y = 18 km at 0129 UTC. Velocity contours are: -35 ms⁻¹ (solid), -30 ms⁻¹ (long dashed), -25 ms⁻¹ (dotted), then repeating; -20 ms⁻¹ (solid), -15 ms⁻¹ (long dashed), -10 ms⁻¹ (dotted), -5 ms⁻¹ (solid), 0 ms⁻¹ (long dashed), +5 ms⁻¹ (dotted), and +10 ms⁻¹ (solid). Velocity maxima are indicated. Storm motion is left to right.

Figure 41. As in Fig. 16 except for Y = 18 km at 0129 UTC.

Figure 42. As in Fig. 15 except for Y = 18 km at 0129 UTC.

forward to the low-level reflectivity maxima. It was also noted to penetrate forward to near the leading edge of reflectivity in 30 - 40% of the cross-sections in the three earlier analyses. As indicated in Fig. 40, the region of rear inflow appears to slope fairly gently for some distance behind the convective line but then slopes more dramatically downward near the high reflectivity in the vicinity of the convective downdraft. Strong front-to-rear flow is also noted in the cross-sections (also Fig. 40) and is primarily colocated with the primary updrafts (Fig. 41). While some variability is noted, maxima in the front-to-rear flow of the first three analyses are typically 24 - 30 ms^{-1} in magnitude, and located at 6 - 7 km altitude along an axes tilted rearward 20 - 40° from vertical.

As in the first three analyses, a distinct band of storm-relative rear inflow was observed to have entered the convective line during the last three analyses (Fig. 43). The core of this rear inflow was also typically located at 3 - 4 km in height well to the rear of the convective region and its instantaneous flow pattern also sloped downward near the convective region . Velocities of the maxima of rear inflow in these later analyses are typically 10 - 14 ms^{-1}, only slightly higher than those noted in the earlier analyses. While the depth of the rear inflow core well behind the convective region does not appear to vary significantly across the period of analysis, an increased frequency is noted for the orientation of the instantaneous pattern of rear inflow into the convective region to become more gently sloped in the later analyses. The corresponding cross-sections of vertical velocity and reflectivity are shown in Figs. 44 and 45, respectively. Rear inflow is noted to penetrate forward to near the leading edge of reflectivity in approximately 40 - 60% of these later cross-sections. Additionally, the maxima in the rear inflow appears to frequently be located at a lower altitude near 1 - 1.5 km, and to penetrate farther into the convective region than the previous analyses, regardless of the slope of the inflow. While strong front-to-rear flow is observed in all of the final four analyses, the maxima typically appear to weaken and become more horizontally oriented, concurrent with the more gentle slope of the rear inflow.

The changes noted in the storm-relative flow fields and the reflectivity structure of the convective region bear a strong resemblence to the evolution of the flow fields and precipitation profile of the two-dimensional model of Rotunno et al. (1988). In their model, they noted that 4 hours into the simulation (Fig. 46a) the updrafts were oriented nearly vertically as was the 2 g kg^{-1} rainwater profile. A layer of low equivalent-potential temperature air was entering the rear of the storm at mid-levels near 4 km (parcels A and F) but did not extend to the surface.

At 4.5 hours into the simulation (Fig. 46b) precipitation had evaporated into the
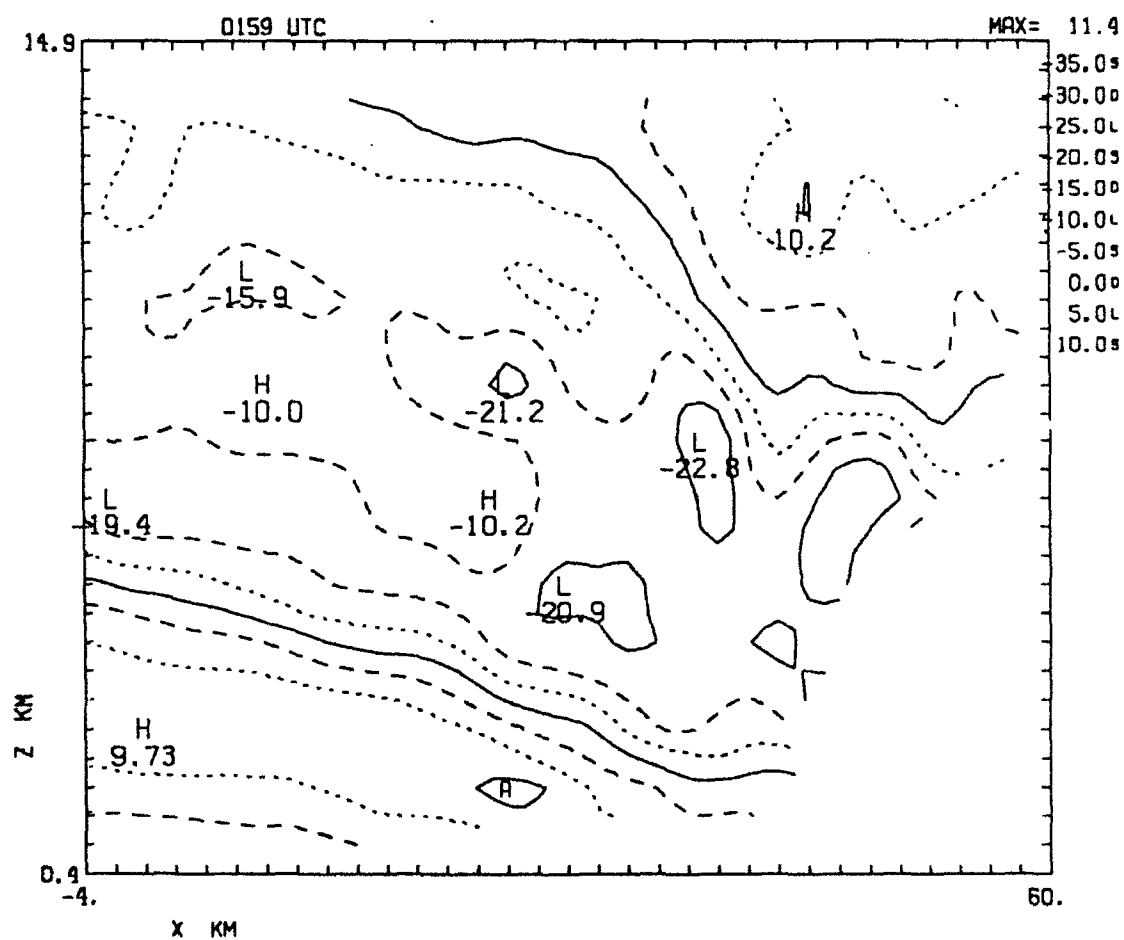
Figure 43. As in Fig. 40 except for Y = 6 km at 0159 UTC.
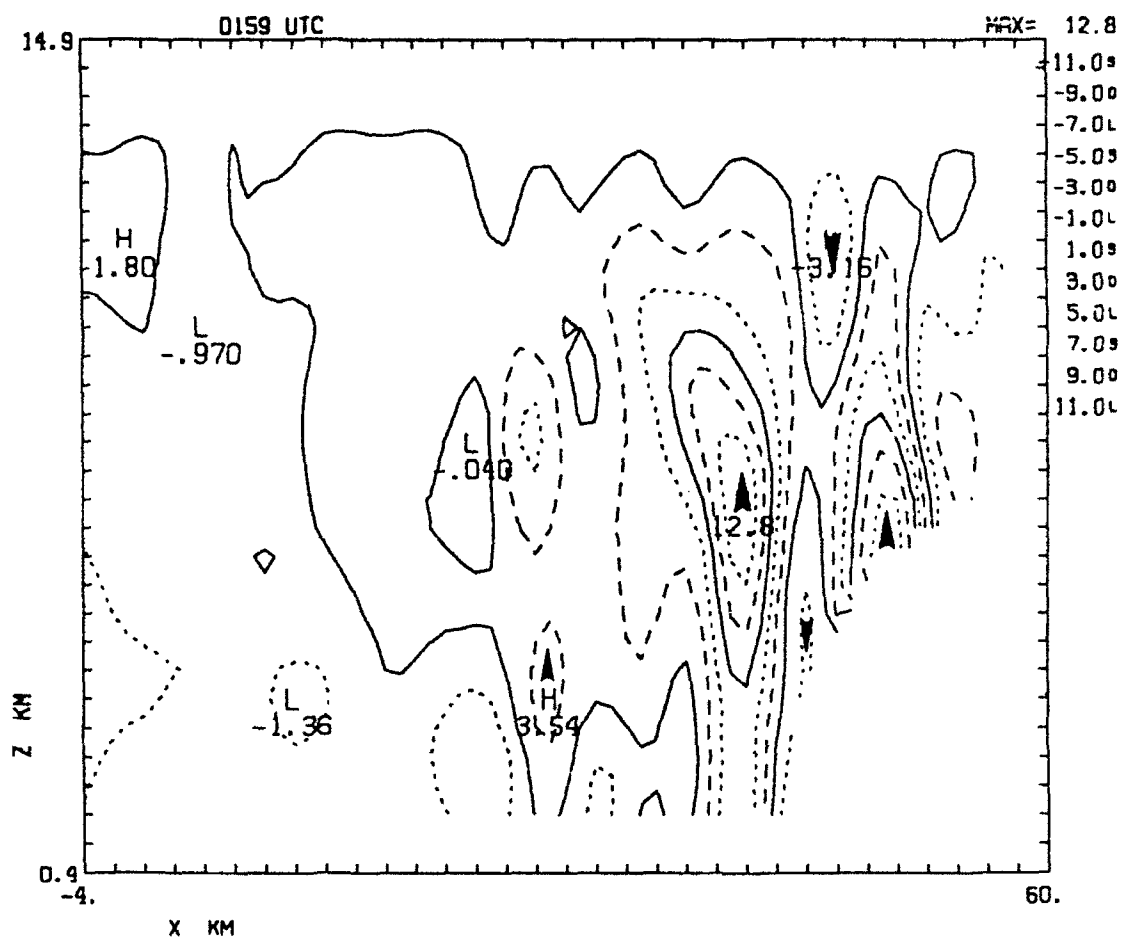
Figure 44. As in Fig. 16 except for Y = 6 km at 0159 UTC.
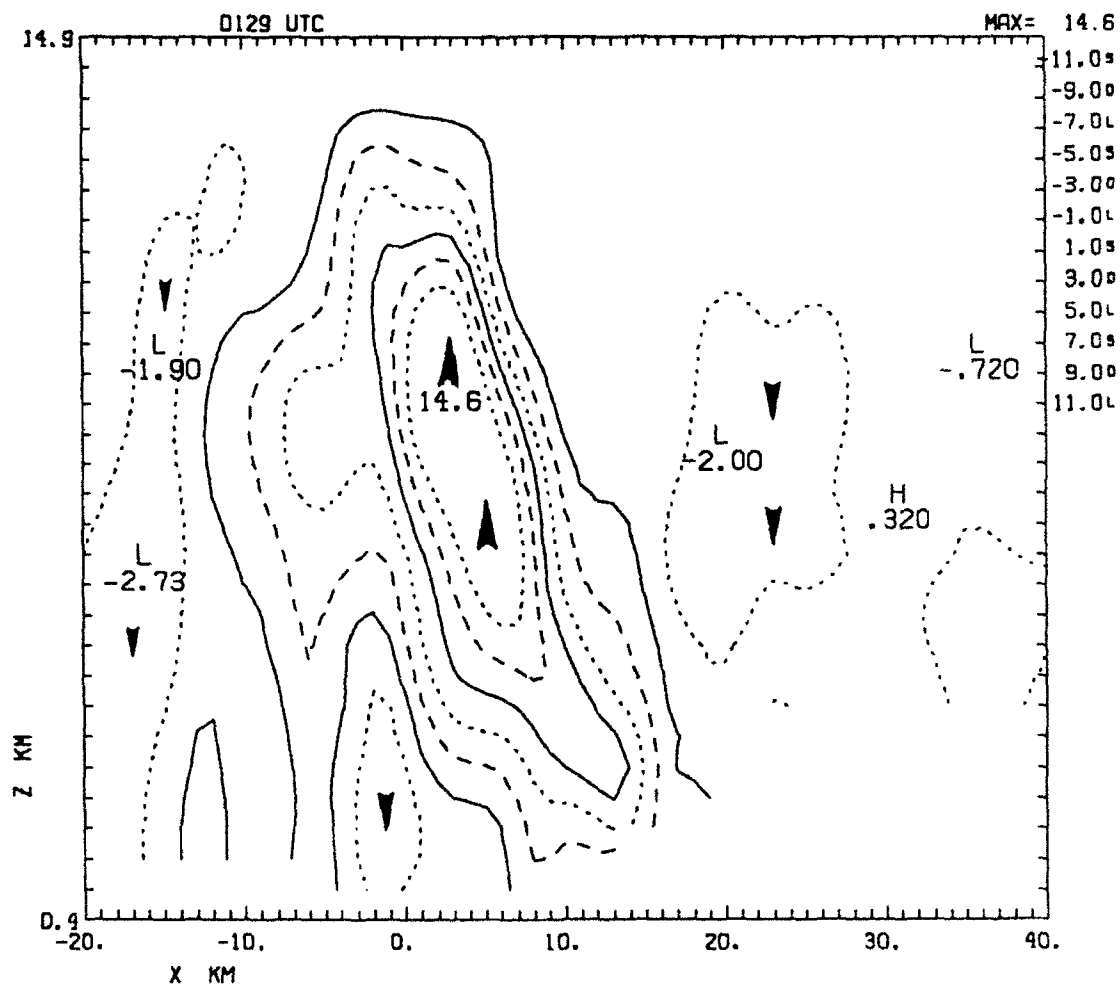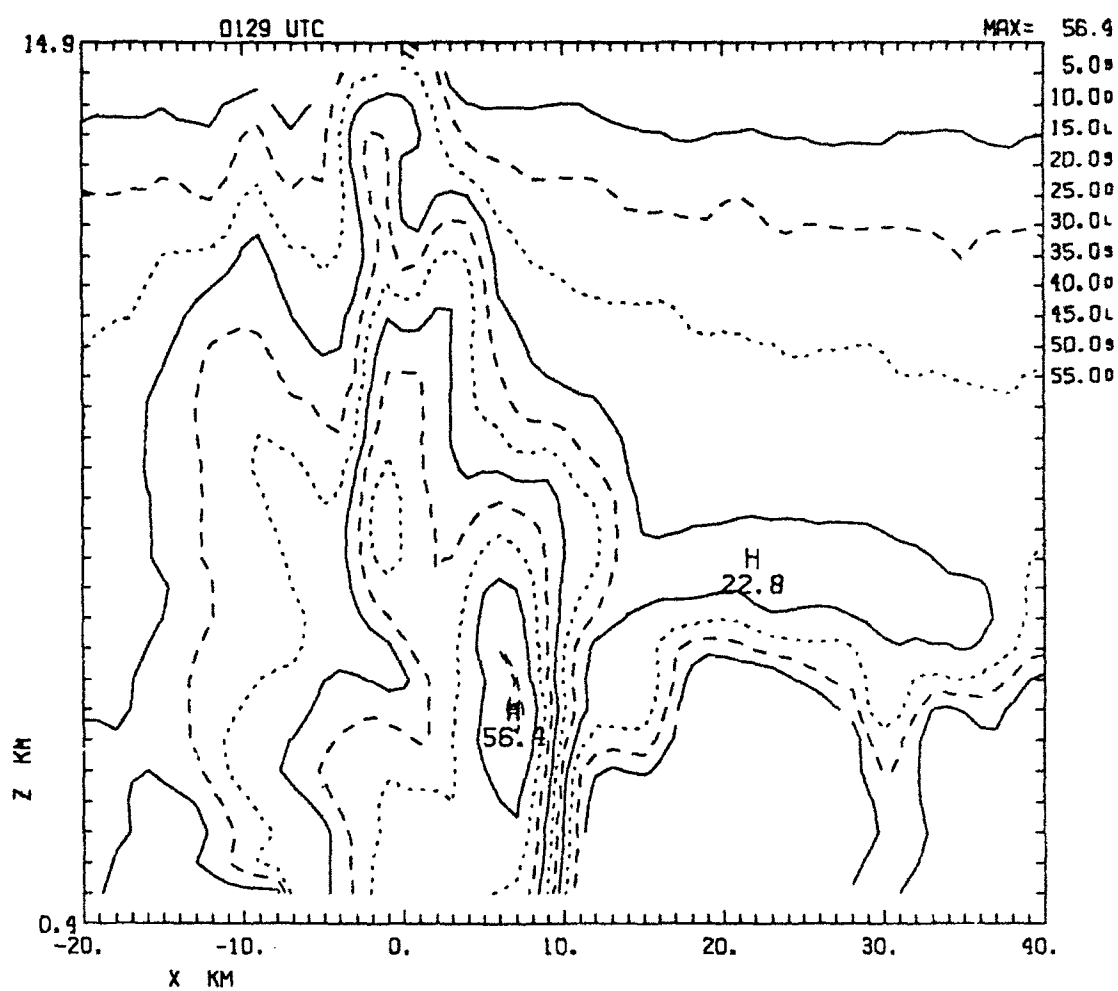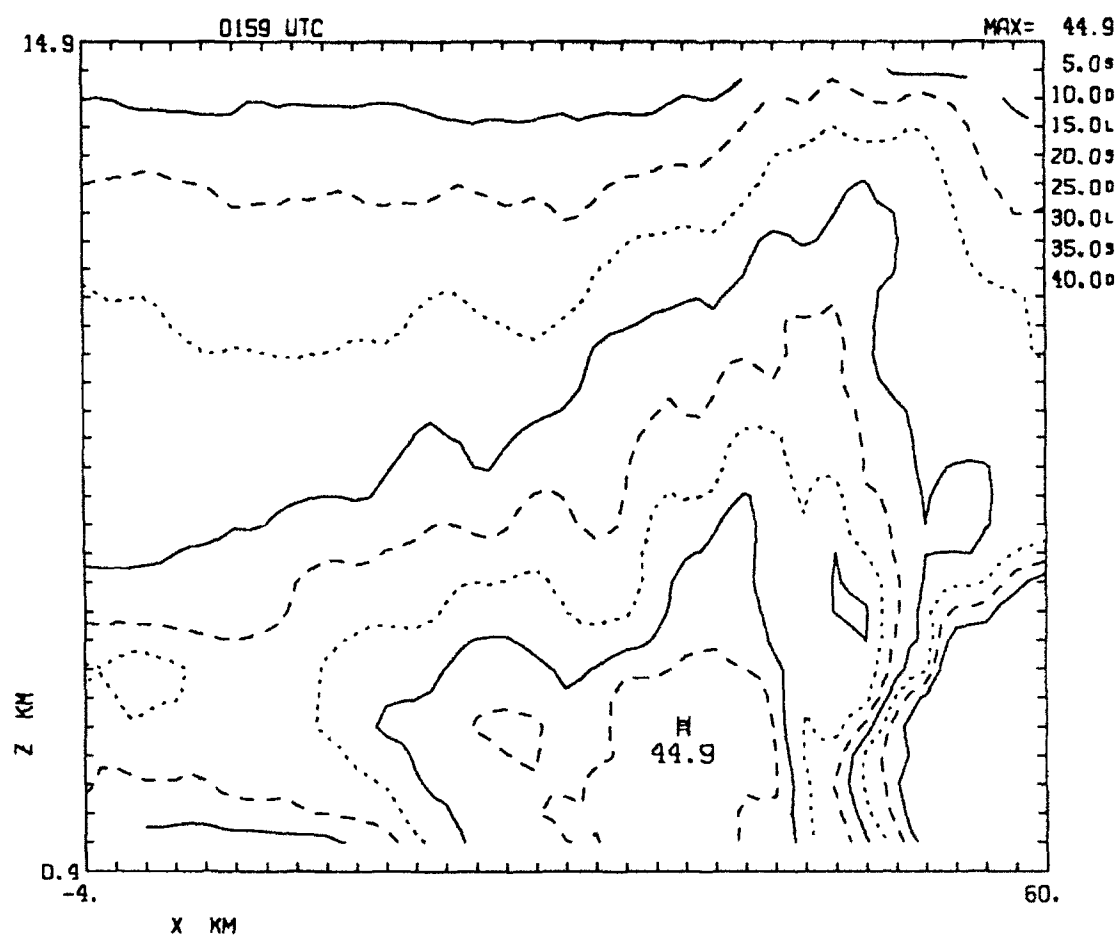
Figure 45. As in Fig. 15 except for Y = 6 km at 0159 UTC.
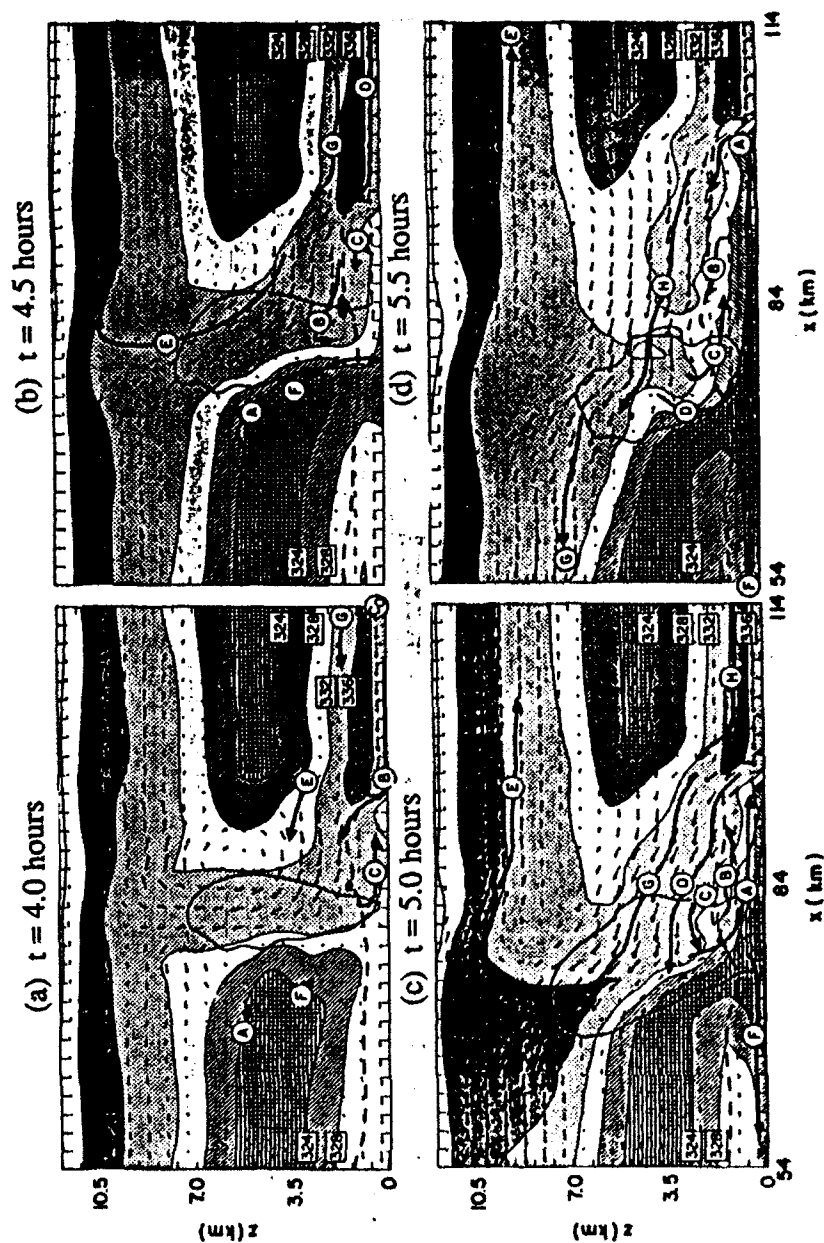
Figure 46. Time sequence from the two-dimensional model illustrating the phase where the cold pool surges downshear and the system weakens. Shading indicates equivalent -potential temperature at 4 K interval. (a) t = 4 hrs. The cold pool begins to dominate the flow. (b) t = 4.5 hrs. Rain evaporates into rear-side mid-level air and induces its descent. (c) t = 5 hrs. Rear-side mid-level air pours to the ground. (d) t = 5.5 hrs. The cold pool continues to surge downshear as the system weakens. From Rotunno et al. (1988).

mid-level air to the rear of the updraft and induced its descent (parcels A and F). Low equivalent-potential temperature air extended to the surface and highlighted the trajectory of rear inflow and downdraft air which strengthened the cold pool. This pattern bears a strong resemblence to the profile of rear inflow observed in the first three analyses of this study (Fig. 40). Additionally, the orientation of the flow vectors through the updrafts of the model at this time also seem to parallel the axis of the maxima in front-to-rear flow observed in the earliest three analyses. The 2 g kg^{-1} rainwater contour in the model also indicates that the reflectivity profile at this time would likely be at its greatest vertical extent, as was observed in the reflectivity cross-sections from the first three analyses of this study.

At 5 hours into the simulation (Fig. 46c) rear-side mid-level air poured to the surface and the cold pool surged downshear (in the positive x-direction). The orientation of this low equivalent-potential temperature air at the rear of the convective region has now begun to resemble the instantaneous pattern of rear inflow more characteristic of the cross-sections from the later three analyses. As the convection weakened, the orientation of the front-to-rear flow vectors of the model became more horizontal, indicating an increase in rearward transport of precipitation particles, as indicated by the change in the slope of the 2 g kg^{-1} rainwater contour, which in-turn aids in the rapid intensification of the trailing stratiform precipitation area. Again, this pattern in the front-to-rear flow of the model at this time strongly resembles the more horizontal orientation of the front-to-rear flow pattern characteristic of the later three analyses of the 10 - 11 June 1985 storm.

By 5.5 hours into the simulation (Fig. 46d) the cold pool (parcel A) continued to surge downshear. The orientation of the rear inflow was more gently sloped and strongly resembles the rear inflow pattern characteristic of the later three analyses. Moreover, the front-to-rear flow pattern continued to have a horizontal orientation similar to that of the later three analyses. The convective drafts of the model weakened significantly and the profile of the 2 g kg^{-1} rainwater contour became more shallow, which would indicate a decreasing cross-sectional profile of mid and upper-level reflectivity with an increasing low-level reflectivity profile, as was observed in the later three analyses of this study.

The behavior of the convective drafts, storm-relative flow patterns, and precipitation profile between the 4th and 5th hour of the two-dimensional simulation by Rotunno et al. (1988), appear to be highly correlated with the evolution of the characteristics of the vertical drafts, storm-relative flow, and reflectivity structure of that portion of the convective region under consideration in this study. This high degree of correlation strongly suggests that the seven Doppler-analyses of this study have sampled

the convective region during the period when as it is undergoing a transition from a stronger to a weaker state.

CHAPTER VI

SENSITIVITY TO THE SAMPLING TECHNIQUE

To test the sensitivity of the mean vertical velocities obtained by the sampling techniques described in Chapter IV to the choice of reflectivity and reflectivity gradient thresholds used, volume-averaged vertical velocites were calculated for the west lobe at 0144 UTC using various combinations of template threshold values. The baseline threshold values chosen were 30 dBZ for reflectivity and 1.5 dB km^{-1} for reflectivity gradient. The reflectivity was then varied by $\pm$ 10% (27/33 dBZ) and the reflectivity gradient by $\pm$ 33% (1.0/2.0 dB km^{-1}). Initially, both 3.9 km and 5.9 km were used as the choice of mid-level for the construction of the forward template component. The forward template was then based on points at either 3.9 or 5.9 km that had reflectivities greater than the reflectivity threshold, or had reflectivity gradients greater than the reflectivity-gradient threshold. The rear portion of the template was always based on the 1.9 km level, using grid points that had reflectivities greater than the stated reflectivity threshold. As in the analysis discussed in Chapter IV, the horizontal extent of the template was limited to just the convective region. Any points ahead of the main band of high reflectivity associated with the line or behind the main band of high reflectivity were omitted from the template. In this manner, small isolated showers ahead of the main convective line and the intense portion of the stratiform region were excluded from the analyses. Results of these calculations are shown in Tables 5 and 6. For comparison, results were also calculated for a single-level horizontal template case, in which both the forward and rear sampling components were constructed at the same level. This was conducted for three different levels (1.9, 3.9, and 5.9 km) and the results are given in Table 7.

For the (5.9/1.9 km) and (3.9/1.9 km) dual-level templates, the results indicate that the mean vertical velocity appears to be more sensitive to the the choice of reflectivity used to construct the template than to the choice of reflectivity gradient. That is, changing the reflectivity by $\pm$ 3 dBZ while holding the reflectivity gradient constant produced variations in mean vertical velocity of about 0.07 ms^{-1}. However, changing the reflectivity gradient by 0.5 dB km^{-1} only induced changes in mean vertical velocity on the order of 0.02 ms^{-1}. Additionally, the differences in mean vertical velocities calculated by using the same combinations of reflectivity and reflectivity gradient but using different template levels, are also on the order of 0.02 ms^{-1}. A larger variation in mean vertical velocity is noted however, between calculations using a 3.9 km versus a 5.9 km single-level template which

Table 5. West lobe volume-averaged vertical velocity data at 0144 UTC using a dual-level(3.9/1.9 km) horizontal sampling template.

Reflectivity (dBZ)	Reflectivity Gradient (dB km⁻¹)	N (template)	Mean w (ms⁻¹)	Std Dev (ms⁻¹)	Min w (ms⁻¹)	Max w (ms⁻¹)	N (volume)
27	1.0	3,112	0.73	2.38	-13.0	17.0	69,047
27	1.5	3,008	0.73	2.38	-13.0	17.0	67,088
27	2.0	2,911	0.73	2.39	-13.0	17.0	65,441
27	----	2,710	0.74	2.38	-13.5	17.5	62,849
30	1.0	2,743	0.79	2.53	-13.0	17.0	59,756
30	1.5	2,634	0.78	2.54	-13.0	17.0	57,693
30	2.0	2,530	0.80	2.55	-13.0	17.0	55,916
30	----	2,285	0.80	2.54	-13.5	17.5	52,524
33	1.0	2,335	0.85	2.73	-13.0	17.0	49,055
33	1.5	2,210	0.86	2.76	-13.0	17.0	46,678
33	2.0	2,098	0.87	2.78	-13.0	17.0	44,751
33	----	1,801	0.88	2.80	-13.5	17.5	40,478
* ---	----	-------	0.85	2.58	-13.5	17.5	75,518

Template thresholding:
   Front component: 3.9 km reflectivity > threshold or reflectivity gradient > threshold
   Rear component: 1.9 km reflectivity > threshold
   Template components merged along x(16.5) km

Sampling window: x(-10,34) km   y(-20,60) km   z(0.4, 14.9) km

N = number of grid points   w = vertical velocity   Std Dev = standard deviation of w

* = volume averaged data inside the sampling window without template thresholding

Table 6. West lobe volume-averaged vertical velocity data at 0144 UTC using a dual-level (5.9/1.9 km) horizontal sampling template.

Reflectivity (dBZ)	Reflectivity Gradient (dB/km)	N (template)	Mean w (m/s)	Std Dev (m/s)	Min w (m/s)	Max w (m/s)	N (volume)
27	1.0	3,102	0.75	2.40	-13.0	17.0	68,481
27	1.5	2,975	0.76	2.42	-13.0	17.0	66,782
27	2.0	2,890	0.76	2.42	-13.0	17.0	65,618
27	----	2,822	0.77	2.42	-13.5	17.5	65,593
30	1.0	2,726	0.80	2.54	-13.0	17.0	59,115
30	1.5	2,571	0.81	2.56	-13.0	17.0	56,693
30	2.0	2,455	0.82	2.57	-13.0	17.0	55,255
30	----	2,340	0.82	2.58	-13.5	17.5	53,335
33	1.0	2,300	0.87	2.75	-13.0	17.0	48,116
33	1.5	2,118	0.89	2.79	-13.0	17.0	45,570
33	2.0	1,965	0.89	2.81	-13.0	17.0	43,316
33	----	1,797	0.90	2.83	-13.5	17.0	40,211
* ---	----	-------	0.85	2.58	-13.5	17.5	75,518

Template thresholding:
  Front component: 5.9 km reflectivity > threshold or reflectivity gradient > threshold
  Rear component: 1.9 km reflectivity > threshold
  Template components merged along x(16.5) km

Sampling window: x(-10,34) km y(-20,60) km z(0.4, 14.9) km

N = number of grid points w = vertical velocity Std Dev = standard deviation of w

* = volume averaged data inside the sampling window without template thresholding

Table 7. West lobe volume-averaged vertical velocity data at 0144 UTC using a single-level horizontal sampling template.

Template Reference Level (km)	Mean w (ms⁻¹)	Std Dev (ms⁻¹)	N (thru volume)	Min w (ms⁻¹)	Max w (ms⁻¹)	N (template)
1.9	0.79	2.52	60,651	-13.0	17.0	2,738
3.9	0.80	2.60	54,422	-13.0	17.0	2,525
5.9	0.97	2.86	42,265	-13.0	17.0	2,202
* ---	0.85	2.58	75,518	-13.5	17.5	---

Template thresholding: > 30 dBZ or 1.5 dB km⁻¹ at template reference level

Sampling window: x(-10,34) km   y(-20,60) km   z(0.4, 14.9) km

N = number of grid points   w = vertical velocity   Std Dev = standard deviation of w

* = volume averaged data inside the sampling window without template thresholding

is on the order of 0.17 ms^{-1}. Given that no extreme fluctuations in mean vertical velocity were noted for small changes in the dual-level template parameters, the baseline values of 30 dBZ reflectivity and 1.5 dB km^{-1} reflectivity gradient were used to construct the sampling templates used in this study.

For the initial sensitivity analysis at 0144 UTC the rectangular box in which the template was constructed was arbitrarily set at 80 km in length along the y-axis (the along-line direction) of the domain. Subsequent preliminary analyses were accomplished at all analysis times with the rectangular boxes constructed to extend 100 km in the along-line direction and approximately 60 km in the across-line direction. The actual cross-line dimension varies slightly to accomodate changes in the width of the convective line with time, and the movement of the line near the edge of the analysis domain at the later times. Inspection of area-averaged vertical velocity profiles obtained with these 100 km length templates reveals a somewhat unorganized variation of mean vertical velocity in space and time (Fig. 47).

Closer inspection of the areal-extent of the derived vertical motion fields revealed some differences in the filling of the 100 km boxes with data, due to the viewing angle of the radars and attenuation of the radar beam from CP-3. Fig. 48 shows a plan-view of the 0129 UTC vertical velocity field at 5.9 km. The gap in the field near the bottom of the figure is due to attenuation of the radar beam from CP-3 by several intense convective cells as it scans nearly straight down the convective line. The gap appears to move from left to right as the convective line moves past CP-3 and radar beam continues to be attenuated. Also, near the top of the figure, the "corner" of the vertical velocity field, an artifact of the scan geometry of the two radars, can be seen near the middle of the convective region. As it may be possible that these irregularities in the areal-extent of the vertical velocity field could induce a bias in the representation of points in the across-line direction, a smaller sampling box was constructed.

The cross-line width of these smaller boxes remains unchanged but the along-line dimension was reduced from 100 km, y (-40, 60), to 50 km, y (-10, 40). While the smaller box samples a lesser portion of the convective line, it minimizes the effects of irregularities in the vertical velocity field due to attenuation and the radar view-angle, yet allows sampling of the convective region on the meso-beta scale. All subsequent sampling of the vertical velocity fields was accomplished with these 50 km length boxes.

Finally, it is recognized that as the lack of low-level reflectivity data ahead of the convective line precludes the calculation of low-level updrafts in developing cells, a bias is introduced into the estimates of area-averaged vertical velocity at low-levels. However,

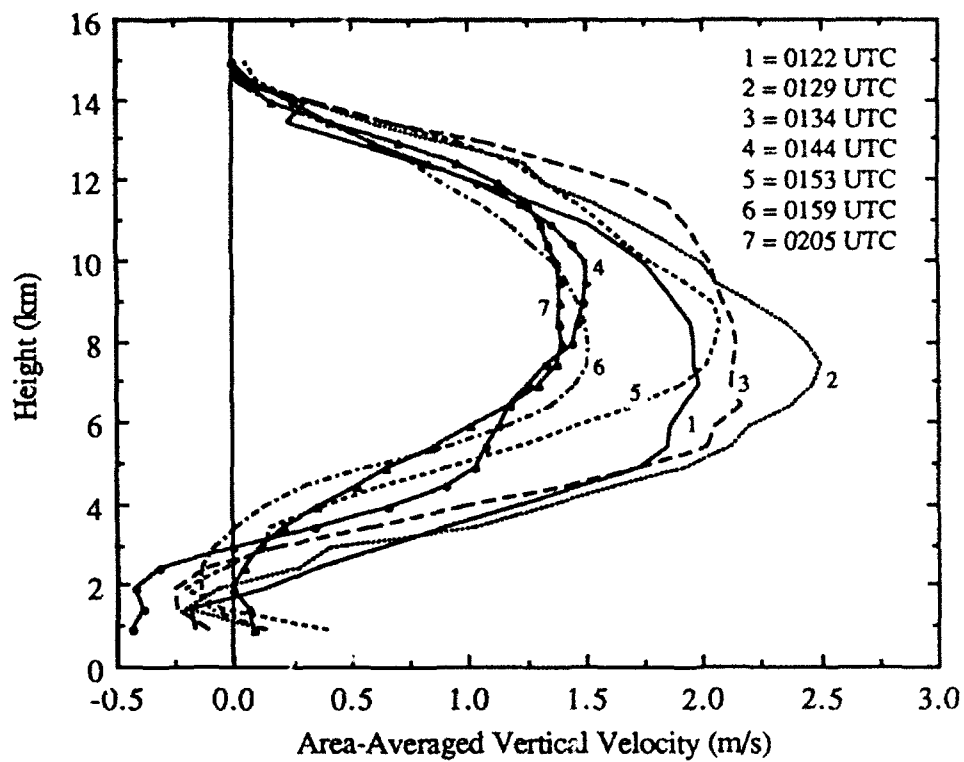Figure 47. As in Fig. 18 except for 100 km length template.
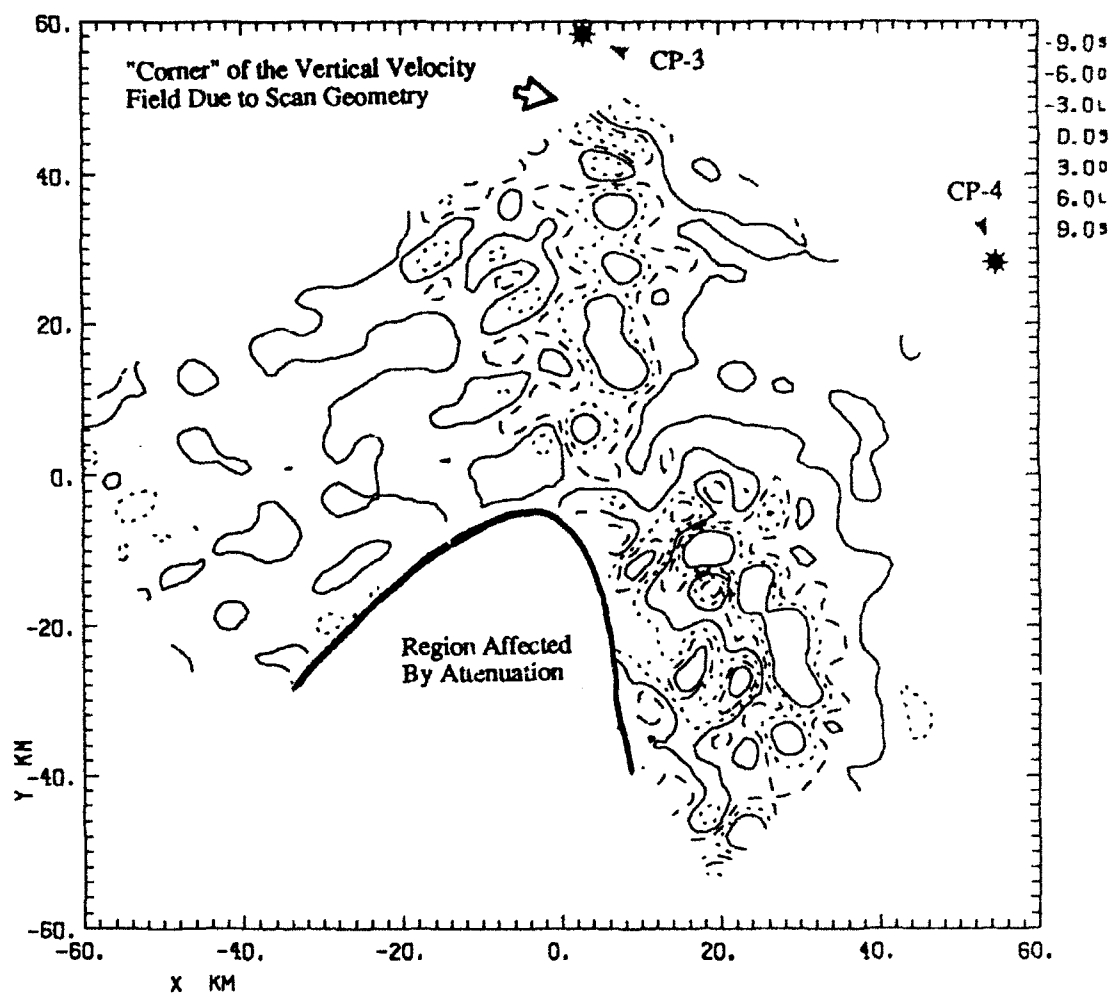
Figure 48. Plan view of 0129 UTC vertical velocity field at 5.9 km height showing regions affected by attenuation and scan geometry. Vertical velocity contours are: -9 ms^{-1} (solid), -6 ms^{-1} (long dashed), -3 ms^{-1} (dotted), then repeating; 0 ms^{-1} (solid), +3 ms^{-1} (long dashed), +6 ms^{-1} (dotted), and +9 ms^{-1} (solid).

this bias is present through the entire 43 minute period of analysis, thus permitting comparison of area-averaged vertical velocity among the seven individual analyses.

CHAPTER VII

CONCLUSIONS AND SUGGESTIONS FOR FURTHER STUDY

The evolution of area-averaged vertical velocity over a mesoscale portion of the convective region of the 10 - 11 June 1985 PRE-STORM squall line has been examined. This study is perhaps one of the first to examine the profiles of mean vertical motion over the convective region with high temporal resolution over a meso (~1 hr) time scale. The objective of the research was to expand current knowledge of the temporal variations of the structure and characteristics of the vertical motion field within the convective region of an individual squall line, and to examine the correlation between the variations in this field and changes with the mesoscale circulation within the storm.

With seven high-resolution dual-Doppler analyses, representing a temporal resolution of 6 - 10 minutes, it was possible to sample the vertical velocity field of a 50 km length segment of the convective region over a nearly one hour period. Area-averaged vertical velocities were computed from individual vertical velocity measurements obtained by sampling the convective region, as objectively defined by thresholds of reflectivity and reflectivity gradient. Vertical profiles of area-averaged vertical velocity indicated an apparently significant and sequential increase in the height and magnitude of peak area-averaged vertical velocity from 0122 - 0134 UTC, a subsequent decrease after 0134 UTC through 0159 UTC, and a slight recovery at 0205 UTC; suggesting an initial period of convective development followed by a sudden weakening, and the indication of possible resurgence by the end of the analysis period. The changes in the variance of the vertical velocity distribution were also observed to follow the temporal trends noted in the profiles of area-averaged vertical velocity.

To investigate the distribution of the vertical velocity field which made up the area-averaged vertical velocity profiles, histograms of the magnitudes of vertical velocity, by grid point, were computed at each analysis time. The histograms show the spectrum of vertical velocity magnitudes narrowing with time across the period of analysis; indicating a trend toward a smaller population of strong vertical velocities and a growing population of weak and moderate velocities. The decrease in spectral width of the magnitudes was noted across both upward and downward velocities but was found to be primarliy due to the decrease in the population of strong upward velocities with time, most notably after 0134 UTC. Strong upward velocities accounted for nearly one third of all upward velocities in the mid-levels through the first three analysis times but dropped to less than one fifth by

0144 UTC; indicating a dramatic weakening of convection by this time. The maxima in upward vertical velocity was observed to climb in height with time through 0134 UTC before decreasing again. Relatively few strong downward velocities were noted throughout the period of analyses although the maximum downward magnitude was observed to move from mid-level to low-level with time, and peak at 0153 UTC.

Vertical cross-sections of the storm-relative wind components, reflectivity, and vertical velocity through the analysis region were used to determine if internal changes in storm structure were related to the observed temporal variations in the vertical velocity field. Examination of the well-developed rear inflow found it to become more gently sloped into the convective region and to penetrate foward to the leading edge of relectivity more frequently in the later analyses, suggesting that a forward surge in the cold pool may have led to the observed weakening in convection during the period of analysis. Thus it appears that the structure of the cold pool and orientation of the rear inflow are closely linked to the state of convection and therefore to the profiles of area-averaged vertical velocity.

Cross-sections of reflectivity were found to support the notion that convective activity was not steady during the analysis period. The area covered by reflectivity of at least 30 dBZ was found to increase with time in the lower levels while decreasing in the levels above, coincident with the reduction in the population of strong upward velocities. The slope of reflectivity in the vertical cross-sections was also noted to shift from a slightly rearward tilt to a more forward tilt by the last analysis time.

The character of the vertical drafts was found to change dramatically after 0134 UTC as they in general became much weaker in magnitude, smaller in diameter, and shorter in depth by 0144 UTC and the later analyses. Many of the updrafts in the first three analyses were found to be 6 - 12 km wide and to extend from low-level, well into the upper levels, while those at the later times were not as well developed. The deepest and strongest downdrafts were noted to occur behind and at a slightly lower height than the stronger updrafts. Low-level downdrafts were observed to be primarily weak to moderate although their strengths increased slightly in the later analyses.

Comparison of the results of this study with the simulations of squall line evolution by Fovell and Ogura (1988) and Rotunno et al. (1988) indicate that the seven Doppler-analyses covering the 43 minute period of this study have possibly captured the rapid transition of the convective region from a stronger to a weaker state. Similar to the model behavior, the convective drafts of this storm have been shown to dramatically weaken over a 10 - 15 minute period as the reflectivity structure indicates a rapid development of the

stratiform region, and the cold pool appears to strengthen and surge downshear. This transition to a weaker state also occurrs on the order of five hours after the initiation of convection, as did the numerical simulations.

Given that we have observed a major transition in the state of convection over a 43 minute period, it appears that a "snapshot" of area-averaged vertical velocity may not be representative over the entire lifecycle of the squall line. Moreover, it may not be entirely representative over the duration of the mature stage of the squall line. We can say however, that a mean profile of area-averaged vertical velocity over the 43 minute period of analysis would hold to approximately a factor of 30 - 50%.

Finally, it has been shown that the high degree of variability noted in the area-averaged vertical velocity profiles from different squall lines (Houze 1989) may not be entirely due to differences in convective structure between storms. The results of this study indicate that the area-averaged vertical velocity over a segment of the convective region varied by as much as a factor of two over a 43 minute period, evidently as a result of mesoscale evolution. However, it might be expected that this high degree of variability may represent the rather extreme case due to the apparent sampling of the storm as it makes a critical transition between two stages of its lifecycle.

To further the results of this study in determining the representativeness of convective region vertical velocity profiles, future work should attempt to focus on data sets which are suitable for simultaneous examination of a larger segment of the convective line. This would permit the investigation of the along-line variability in area-averaged vertical motion, and the comparison of its magnitude to that observed due to evolution, to determine the relative importance of each. Additionally, this work should be repeated for convective storms in other stages of evolution to determine the degree of variability in area-averaged vertical velocities over the squall line lifecycle. Only when the vertical motion field within the convective region has been adequately described in space and time, will the parameterization of its vertical heating profile for other studies be truly representative.

REFERENCES

Balsley, B.B., L.W. Ecklund, D.A. Carter, A.C. Riddle and K.S. Gage, 1988: Average vertical motions in the tropical atmosphere observed by a radar wind profiler on Pohnpei (7° N latitude, 157° E longitude). *J. Atmos. Sci.*, **45**, 396-405.

Biggerstaff, M.I., R.A. Houze, Jr., and S.A. Rutledge, 1988: Vertical drafts in the convective regions of mesoscale convective systems in Kansas. Preprints, *Tenth International Cloud Physics Conference*, Bad Homburg, 15-20 August 1988. pp. 705-707. Offenbach am Main: *Deutcher Wetterdienst*.

_____, and R.A. Houze, Jr., 1991a: Kinematic and precipitation structure of the 10-11 June 1985 squall line. *Mon Wea. Rev.*, **119**, 3034-3065.

_____, and R.A. Houze, Jr., 1991b: Midlevel vorticity structure of the 10-11 June 1985 squall line. *Mon Wea. Rev.*, **119**, 3066-3079.

Bluestein, H.B. and M.H. Jain, 1985: Formation of mesoscale lines of precipitation: Severe squall lines in Oklahoma during the spring. *J. Atmos. Sci.*, **42**, 1711-1732.

_____, G.T. Marx, and M.H. Jain, 1987: Formation of mesoscale lines of precipitation: Nonsevere squall lines in Oklahoma during the spring. *Mon. Wea. Rev.*, **115**, 2719-2727.

Chong, M., 1983: Les radars meteorologiques Doppler pour l'etude de la convection orgeuse. Application a une ligne de grains tropicale. These de Doctorat d'Etat. Universite de Paris, France.

_____, P. Amayenc, G. Scialom and J. Testud, 1987: A tropical squall line observed during the COPT 81 experiment in West Africa. Part I: Kinematic structure inferred from dual-Doppler radar data. *Mon. Wea. Rev.*, **115**, 670-694.

Fovell, R.G., and Y. Ogura, 1988: Numerical simulation of a midlatitude squall line in two dimensions. *J. Atmos. Sci.*, **45**, 3846-3879.

_____, and _____, 1989: Effect of vertical wind shear on numerically simulated multicell storm structure. *J. Atmos. Sci.*, **46**, 3144-3176.

Gamache, J.F., and R.A. Houze, Jr., 1982: Mesoscale air motions associated with a tropical squall line. *Mon. Wea. Rev.*, **110**, 118-135.

_____, and _____, 1985: Further analysis of the composite wind and thermodynamic structure of the 12 September GATE squall line. *Mon. Wea. Rev.*, **113**, 1241-1259.

Hamilton, R.A., and J.W. Archibold, 1945: Meteorology of Nigeria and adjacent territory. *Quart. J. Roy. Meteor. Soc.*, **83**, 303-314.

Hartman, D.L., H.H. Hendon and R.A. Houze, Jr., 1984: Some implications of the mesoscale circulations in tropical cloud clusters for large-scale dynamics and climate. *J. Atmos. Sci.*, **41**, 113-121.

Heymsfield, G.M., and S. Schotz, 1985: Structure and evolution of a severe squall line over Oklahoma. *Mon. Wea. Rev.*, **113**, 1563-1589.

Houze, R.A., Jr., 1977; Structure and dynamics of a tropical squall line system. *Mon. Wea. Rev.*, **105**, 1540-1567.

____, and E.N. Rappaport, 1984: Air motions and precipitation structure of an early summer squall line over the eastern tropical Atlantic. *J. Atmos. Sci.*, **41**, 553-574.

____, 1989: Observed structure of mesoscale convective systems and implications for large-scale heating. *Quart. J. Roy. Meteor. Soc.*, **115**, 425-461.

____, S.A. Rutledge, M.I. Biggerstaff, and B.F. Smull, 1989: Interpretation of Doppler weather radar displays of midlatitude mesoscale convective systems, *Bull. Amer. Meteor. Soc.*, **70**, 608-619.

____, B.F. Smull, and P. Dodge, 1990: Mesoscale organization of springtime rainstorms in Oklahoma. *Mon. Wea. Rev.*, **118**, 613-654.

Johnson, R.H., 1982: Vertical motions of near-equatorial winter monsoon convection. *J. Meteor. Soc. Jap.*, **60**, 682-690.

Lafore, J-P., and M.W. Moncrieff, 1989: A numerical simulation of a midlatitude squall line in two dimensions. *J. Atmos. Sci.*, **46**, 521-544.

Leary, C.A., and R.A. Houze, Jr., 1979: The structure and evolution of convection in a tropical cloud cluster. *J. Atmos. Sci.*, **36**, 437-457.

____, and E.N. Rappaport, 1987: The lifecycle and internal structure of a mesoscale convective complex. *Mon. Wea. Rev.*, **115**, 1503-1527.

LeMone, M.A., and E.J. Zipser, 1980: Cumulonimbus vertical velocity events in GATE. Part I: Diameter, intensity, and mass flux. *J. Atmos. Sci.*, **37**, 2444-2457.

Leise, J.A., 1981: A multi-dimensional scale-telescoped filter and data extension package. Nat. Ocean. and Atmos. Admin. Tech. Memo, WPL-82, 20pp.

Marks, F.D., Jr., and R.A. Houze, Jr., 1987: Inner-core structure of Hurricane Alicia from airborne Doppler-radar observations. *J. Atmos. Sci.*, **44**, 1296-1317.

Mohr, C.G., L.S. Miller, and R.L. Vaughn, 1979: An economical procedure for Cartesian interpolation and display of reflectivity factor data in three-dimensional space. *J. Appl. Meteor.*, **18**, 661-670.

____, and ____, 1983: CEDRIC - a software package for Cartesian space editing, synthesis, and display of radar fields under interactive control. Preprints, *21st Conf. on Radar Meteor.*, Edmonton, Alberta, Amer. Meteor. Soc., 559-574.

Moncrieff, M.W., and M.J. Miller, 1976: A theory for organized steady convection and its transport properties. *Quart. J. Roy. Meteor. Soc.*, **102**, 373-394.

Newton, C.W., 1950: Structure and mechanisms of the prefrontal squall line. *J. Meteor.*, **7**, 210-222.

Ogura, Y., and M.T. Liou, 1980: The structure of a midlatitude squall line. *J. Atmos. Sci.*, **37**, 553-567.

Oye, R., and R.E. Carbone, 1981: Interactive Doppler editing software. Preprints. *20th Conf. on Radar Meteor.*, Boston, Amer. Meteor. Soc., 683-689.

Pedgley, D.E., 1962: A meso-synoptic analysis of the thunderstorms on 28 August 1958. *Brit. Meteor. Off., Geophys. Mem.*, **106**, 74pp.

Rotunno, R., J.B. Klemp and M.L. Weisman, 1988: A theory for strong, long-lived squall lines. *J. Atmos. Sci.*, **45**, 463-485.

Rutledge, S.A., R.A. Houze, Jr., M.I. Biggerstaff, and T. Matejka, 1988: The Oklahoma-Kansas mesoscale convective system of 10-11 June 1985: Precipitation structure and single-Doppler radar analysis. *Mon. Wea. Rev.*, **116**, 1409-1430.

Smull, B.F., and R.A. Houze, Jr., 1985: A midlatitude squall line with a trailing region of stratiform rain: Radar and satellite observations. *Mon. Wea. Rev.*, **113**, 117-133.

____, and ____ 1987a: Dual-Doppler radar analysis of a midlatitude squall line with a trailing region of stratiform rain. *J. Atmos. Sci.*, **44**, 2128-2148.

____, and ____, 1987b: Rear inflow in squall lines with trailing stratiform precipitation. *Mon. Wea. Rev.*, **115**, 2869-2889.

Thorpe, A.J., M.J. Miller, and M.W. Moncrieff, 1982: Two-dimensional convection in nonconstant shear: a model of midlatitude squall lines. *Quart. J. Roy. Meteor. Soc.*, **108**, 739-762.

Vasiloff, S.V., 1989: Vorticity dynamics of a squall line: A Doppler-radar analysis of the 10-11 June 1985 squall line. M.S. thesis, University of Oklahoma, 100 pp.

Weisman, M.L., and J.B. Klemp, 1982: The dependence of numerically simulated convective storms on windshear and bouyancy. *Mon. Wea. Rev.*, **110**, 504-520.

____, ____, and R. Rotunno, 1988: Structure and evolution of numerically simulated squall lines. *J. Atmos. Sci.*, **45**, 1990-2013.

Zhang, D.-L., K. Gao, .r¹ D.B. Parsons, 1989: Numerical simulation of an intense squall line during 10-11 June 1985 PRE-STORM. Part I: Model verification. *Mon Wea. Rev.*, **117**, 960-994.

____ and ____, 1989: Numerical simulation of an intense squall line during 10-11 June 1985 PRE-STORM. Part II: Rear inflow and surface pressure perturbations. *Mon. Wea. Rev.*, **117**, 2067-2094.

Zipser, E.J., 1969: The role of organized unsaturated downdrafts in the structure and rapid decay of an equatorial disturbance. *J. Appl. Meteor.*, **8**, 799-814.

____, 1977: Mesoscale and convective-scale downdrafts as distinct components of squall line circulation. *Mon. Wea. Rev.*, **105**, 1568-1589.

____, and M.A. LeMone, 1980: Cumulonimbus vertical velocity events in GATE. Part II: Synthesis and model core structure. *J. Atmos. Sci.*, **37**, 2458-2469.

APPENDICES

APPENDIX A

CEDRIC FUNCTIONS USED IN THE CREATION OF THE DUAL-LEVEL (5.9/1.9 KM) HORIZONTAL SAMPLING TEMPLATE AND THE SAMPLING OF THE VERTICAL VELOCITY FIELDS

Comment: set window to 1.9 - 5.9 km levels of entire sampling template

---

+++ FUNCTION +++

EDITING WINDOW LOOKS LIKE THIS:

		DISTANCES	
AXIS	MIN	MAX	UNITS
X	-10.0	56.0	KM
Y	-10.0	40.0	KM
Z	1.9	5.9	KM

Comment: compute reflectivity gradient and points with reflectivity at least 30 dBZ

---

2 EDIT FIELDS EXIST AT PRESENT:
  MAXDZ   W4DP
0 CONSTANT FIELD PLANES W/INITIALIZATION INFO
FUNCTION STACK.....

F (OUT)	TYPE	FUNCTION	F1	F2	C1
DX	/T	DF1/DX	MAXDZ		
DY	/T	DF2/DY	MAXDZ		
SUM	/T	F1*F1+F2*F2	DX	DY	
GRAD	/P	SQRT(F1)	SUM		
RDBZ30	/P	F1, IF, C1 < F2	MAXDZ	MAXDZ	29.999

DIRECTION THROUGH THE Z PLANES: 1

4 EDIT FIELDS EXIST AT PRESENT:
  MAXDZ   W4DP   GRAD   RDBZ30

Comment: resize window for forward portion of template, compute those points with reflectivity gradient exceeding 1.5 db/km, compute those points with reflectivity of at least 30 dBZ or reflectivity gradient exceeding 1.5 dB/km, define forward half of template by assigning value of 99 where grid points do not meet the above criteria (else "bad")

EDITING WINDOW LOOKS LIKE THIS:

		DISTANCES	
AXIS	MIN	MAX	UNITS
X	17.0	56.0	KM
Y	-10.0	40.0	KM
Z	1.9	5.9	KM

4 EDIT FIELDS EXIST AT PRESENT:
  MAXDZ W4DP GRAD RDBZ30
1 CONSTANT FIELD PLANES W/INITIALIZATION INFO
1:     BL   /   9900
FUNCTION STACK....

F (OUT)	TYPE	FUNCTION	F1	F2	C1
RGRAD15	/T	F1, IF, C1 < F2	MAXDZ	GRAD	1.500
RDB30G15	/T	F1 .ORELSE. F2	RDBZ30	RGRAD15	
TEMPF	/P	F1, IF, F2 EQ. BAD	BL	RDB30G15	

DIRECTION THROUGH THE Z PLANES: 1

5 EDIT FIELDS EXIST AT PRESENT:
  MAXDZ W4DP GRAD RDBZ30 TEMPF

Comment: resize window for rear half of template, assign value of 99 at grid points with reflectivity less than 30 dBZ

EDITING WINDOW LOOKS LIKE THIS:

		DISTANCES	
AXIS	MIN	MAX	UNITS
X	-10.0	16.0	KM
Y	-10.0	40.0	KM
Z	1.9	5.9	KM

5 EDIT FIELDS EXIST AT PRESENT:
  MAXDZ W4DP GRAD RDBZ30 TEMPF
1 CONSTANT FIELD PLANES W/INITIALIZATION INFO
1:     BL   /   RETAINED
FUNCTION STACK....

F (OUT)	TYPE	FUNCTION	F1	F2	C1
TEMPR	/P	F1, IF, F2 EQ. BAD	BL	RDBZ30	

DIRECTION THROUGH THE Z-PLANES: 1

6 EDIT FIELDS EXIST AT PRESENT:
  MAXDZ W4DP GRAD RDBZ30 TEMPF TEMPR

Comment: resize window for entire template, create constant field plane (T1) from 1.9 km level of rear portion of template, then merge with forward half of template

---

EDITING WINDOW LOOKS LIKE THIS:

		DISTANCES	
AXIS	MIN	MAX	UNITS
X	-10.0	56.0	KM
Y	-10.0	40.0	KM
Z	1.9	5.9	KM

6 EDIT FIELDS EXIST AT PRESENT:
   MAXDZ W4DP GRAD RDBZ30 TEMPF TEMPR
1 CONSTANT FIELD PLANES W/INITIALIZATION INFO
1:    T1   / TEMPR   (1.9 KM)
FUNCTION STACK....

F (OUT)	TYPE	FUNCTION	F1	F2	C1
TEMP5	/P	F1 .ORELSE. F2	T1	TEMPF	

DIRECTION THROUGH THE Z-PLANES: 1

7 EDIT FIELDS EXIST AT PRESENT:
   MAXDZ W4DP GRAD RDBZ30 TEMPF TEMPR TEMP5

Comment: resize window to full vertical extent, create constant field plane (T5) from 5.9 km level of the merged template (TEMP5), create the "sampled" vertical velocity field (WTEMP5) by keeping only those grid points from the original vertical velocity field (W4DP) where a value of 99 had not been assigned (where T5 equal "bad"; the grid points meet the thresholds of reflectivity or reflectivity gradient)

EDITING WINDOW LOOKS LIKE THIS:

		DISTANCES	
AXIS	MIN	MAX	UNITS
X	-10.0	56.0	KM
Y	-10.0	40.0	KM
Z	0.9	14.9	KM

7 EDIT FIELDS EXIST AT PRESENT:
   MAXDZ W4DP GRAD RDBZ30 TEMPF TEMPR TEMP5

1 CONSTANT FIELD PLANES W/INITIALIZATION INFO
1:    T5   / TEMP5   (5.9 KM)
FUNCTION STACK....

F (OUT)	TYPE	FUNCTION	F1	F2	C1
WTEMP5	/P	F1, IF, F2 EQ. BAD	W4DP	T5	

DIRECTION THROUGH THE Z-PLANES: 1

8 EDIT FIELDS EXIST AT PRESENT:
   MAXDZ W4DP GRAD RDBZ30 TEMPF TEMPR TEMP5 WTEMP5

APPENDIX B

AREA-AVERAGED
VERTICAL VELOCITY AND REFLECTIVITY DATA

Table B1. Area-averaged vertical velocity and reflectivity data for 0122 UTC.

Grid Level (km)	Mean w (ms^{-1})	Std Dev w (ms^{-1})	Points Sampled	Mean Reflectivity (dBZ)
0.9	-0.09	2.51	671	14.95
1.4	-0.37	2.78	1,252	20.95
1.9	-0.22	2.95	1,317	22.61
2.4	0.09	3.15	1,361	23.13
2.9	0.42	3.35	1,382	24.21
3.4	0.80	3.57	1,387	25.12
3.9	1.19	3.74	1,399	24.36
4.4	1.50	3.86	1,430	23.65
4.9	1.79	3.80	1,500	23.70
5.4	1.86	3.77	1,617	23.50
5.9	1.80	3.67	1,820	24.57
6.4	1.83	3.77	1,846	25.86
6.9	1.86	3.89	1,846	26.13
7.4	1.78	4.02	1,867	25.54
7.9	1.77	4.09	1,867	24.42
8.4	1.72	4.13	1,867	23.23
8.9	1.66	4.11	1,860	22.15
9.4	1.57	3.99	1,850	21.03
9.9	1.46	3.76	1,837	19.80
10.4	1.33	3.46	1,823	18.49
10.9	1.20	3.12	1,787	17.17
11.4	1.04	2.70	1,767	15.79
11.9	0.84	2.19	1,763	14.33
12.4	0.64	1.65	1,687	12.73
12.9	0.45	1.10	1,485	10.99
13.4	0.25	0.65	1,214	8.95
13.9	0.31	0.42	322	6.38
14.4	0.02	0.06	84	2.27
14.9	0.00	0.00	0	-1.17
Volume	1.17	3.46	41,908	

Table B2. Area-averaged vertical velocity and reflectivity data for 0129 UTC.

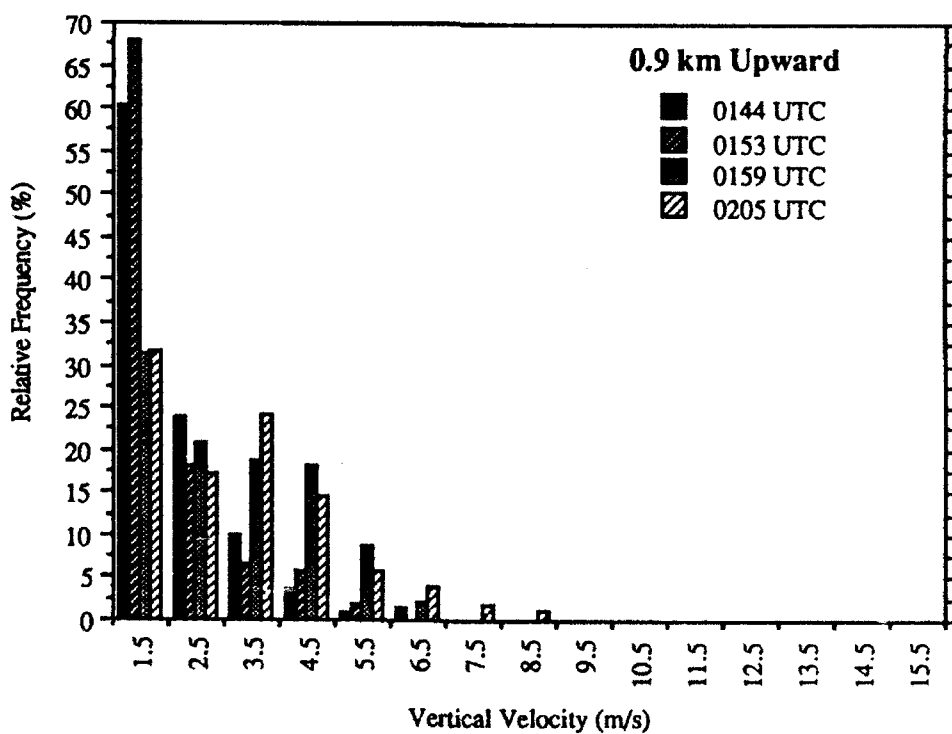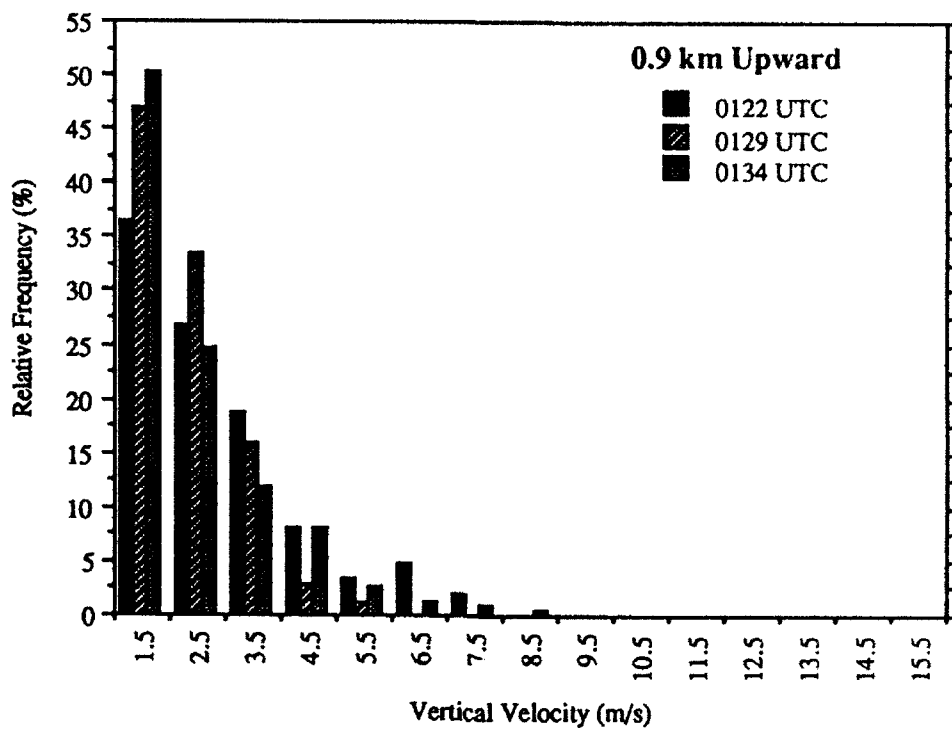| Grid Level (km)	Mean w (ms⁻¹)	Std Dev w (ms⁻¹)	Points Sampled	Mean Reflectivity (dBZ)
0.9	0.02	1.87	620	26.45
1.4	-0.17	2.15	1,008	27.19
1.9	0.02	2.61	1,070	25.92
2.4	0.39	3.15	1,266	24.91
2.9	0.75	3.38	1,287	25.46
3.4	1.15	3.54	1,311	24.62
3.9	1.50	3.65	1,368	24.77
4.4	1.85	3.83	1,380	23.30
4.9	2.14	3.98	1,409	23.57
5.4	2.32	4.06	1,471	23.71
5.9	2.38	4.11	1,560	25.49
6.4	2.52	4.16	1,580	26.22
6.9	2.56	4.20	1,596	26.01
7.4	2.54	4.22	1,596	25.18
7.9	2.44	4.19	1,645	24.20
8.4	2.33	4.19	1,654	23.28
8.9	2.20	4.17	1,654	22.38
9.4	2.08	4.12	1,647	21.33
9.9	1.96	4.05	1,631	20.12
10.4	1.82	3.88	1,628	18.85
10.9	1.66	3.61	1,620	17.49
11.4	1.44	3.19	1,617	16.00
11.9	1.17	2.65	1,605	14.36
12.4	0.89	2.03	1,564	12.62
12.9	0.60	1.41	1,479	10.68
13.4	0.33	0.87	1,244	8.44
13.9	0.20	0.41	668	5.61
14.4	0.03	0.07	145	1.74
14.9	0.00	0.00	0	-0.46
Volume	1.58	3.63	38,322	

Table B3. Area-averaged vertical velocity and reflectivity data for 0134 UTC.

Grid Level (km)	Mean w (ms⁻¹)	Std Dev w (ms⁻¹)	Points Sampled	Mean Reflectivity (dBZ)
0.9	-0.04	2.29	802	19.83
1.4	-0.25	2.46	1,238	19.68
1.9	-0.33	2.59	1,238	21.42
2.4	-0.22	2.75	1,238	23.02
2.9	0.09	2.98	1,238	23.68
3.4	0.56	3.22	1,240	23.47
3.9	1.10	3.39	1,314	23.30
4.4	1.59	3.48	1,341	23.26
4.9	1.86	3.56	1,430	23.22
5.4	2.16	3.71	1,452	24.24
5.9	2.28	3.89	1,519	25.39
6.4	2.50	4.03	1,524	25.84
6.9	2.66	4.12	1,524	25.48
7.4	2.76	4.16	1,524	24.64
7.9	2.79	4.18	1,524	23.77
8.4	2.75	4.20	1,524	22.87
8.9	2.67	4.24	1,524	21.77
9.4	2.60	4.28	1,516	20.69
9.9	2.50	4.30	1,514	19.59
10.4	2.38	4.25	1,510	18.46
10.9	2.25	4.11	1,498	17.20
11.4	2.04	3.83	1,496	15.86
11.9	1.79	3.43	1,489	14.46
12.4	1.49	2.91	1,484	12.92
12.9	1.13	2.29	1,470	11.20
13.4	0.75	1.62	1,402	9.09
13.9	0.42	0.91	1,191	6.32
14.4	0.04	0.08	713	3.67
14.9	0.00	0.00	0	2.22
Volume	1.64	3.67	38,477	

Table B4. Area-averaged vertical velocity and reflectivity data for 0144 UTC.

Grid Level (km)	Mean w (ms⁻¹)	Std Dev w (ms⁻¹)	Points Sampled	Mean Reflectivity (dBZ)
0.9	-0.28	2.09	1,102	22.22
1.4	-0.35	2.12	1,485	22.53
1.9	-0.38	2.26	1,486	25.11
2.4	-0.27	2.38	1,486	28.16
2.9	0.11	2.64	1,512	30.33
3.4	0.52	2.80	1,531	30.62
3.9	0.98	2.94	1,576	29.93
4.4	1.30	3.01	1,614	27.81
4.9	1.44	3.06	1,693	27.30
5.4	1.53	3.08	1,771	26.83
5.9	1.58	3.06	1,827	26.67
6.4	1.67	3.06	1,832	25.98
6.9	1.69	3.07	1,882	25.65
7.4	1.72	3.11	1,883	25.12
7.9	1.78	3.18	1,911	24.34
8.4	1.74	3.24	1,911	23.42
8.9	1.69	3.29	1,917	22.44
9.4	1.64	3.30	1,916	21.44
9.9	1.57	3.24	1,917	20.34
10.4	1.47	3.12	1,918	19.14
10.9	1.34	2.95	1,910	17.80
11.4	1.20	2.68	1,911	16.36
11.9	1.05	2.31	1,902	14.80
12.4	0.87	1.85	1,867	13.26
12.9	0.68	1.32	1,792	11.55
13.4	0.46	0.77	1,722	9.59
13.9	0.25	0.35	1,458	7.77
14.4	0.09	0.09	835	6.07
14.9	0.00	0.00	0	4.27
Volume	1.06	2.81	47,567	

Table B5. Area-averaged vertical velocity and reflectivity data for 0153 UTC.

Grid Level (km)	Mean w (ms⁻¹)	Std Dev w (ms⁻¹)	Points Sampled	Mean Reflectivity (dBZ)
0.9	0.29	1.50	640	27.17
1.4	-0.25	2.07	1,080	28.46
1.9	-0.39	2.41	1,414	30.62
2.4	-0.23	2.54	1,570	30.10
2.9	-0.04	2.58	1,611	30.01
3.4	0.22	2.65	1,615	29.33
3.9	0.49	2.80	1,632	27.86
4.4	0.75	2.93	1,641	26.23
4.9	1.00	3.05	1,667	26.09
5.4	1.21	3.08	1,712	26.00
5.9	1.35	2.98	1,741	26.26
6.4	1.47	2.87	1,762	26.33
6.9	1.52	2.83	1,798	25.89
7.4	1.51	2.84	1,832	25.10
7.9	1.49	2.88	1,840	24.18
8.4	1.43	2.91	1,848	23.08
8.9	1.36	2.89	1,855	21.97
9.4	1.27	2.87	1,851	20.70
9.9	1.17	2.86	1,846	19.34
10.4	1.07	2.84	1,834	17.95
10.9	1.00	2.74	1,812	16.59
11.4	0.94	2.56	1,803	15.13
11.9	0.88	2.28	1,800	13.63
12.4	0.78	1.94	1,795	12.10
12.9	0.62	1.50	1,762	10.41
13.4	0.40	0.96	1,714	8.36
13.9	0.17	0.43	1,685	5.67
14.4	0.02	0.06	779	3.22
14.9	0.00	0.00	0	2.33
Volume	0.84	2.63	45,939	

Table B6. Area-averaged vertical velocity and reflectivity data for 0159 UTC.

Grid Level (km)	Mean w (ms⁻¹)	Std Dev w (ms⁻¹)	Points Sampled	Mean Reflectivity (dBZ)
0.9	0.25	2.10	983	29.03
1.4	0.07	2.10	1,653	29.17
1.9	-0.03	2.21	1,653	29.80
2.4	-0.02	2.27	1,653	29.68
2.9	0.11	2.31	1,653	30.09
3.4	0.32	2.40	1,675	29.76
3.9	0.54	2.53	1,689	28.46
4.4	0.71	2.66	1,697	26.73
4.9	0.86	2.73	1,712	26.17
5.4	1.01	2.82	1,748	25.87
5.9	1.16	2.92	1,798	25.97
6.4	1.20	2.88	1,824	25.66
6.9	1.18	2.79	1,864	25.13
7.4	1.11	2.69	1,874	24.31
7.9	1.01	2.59	1,874	23.19
8.4	0.89	2.50	1,874	21.99
8.9	0.79	2.44	1,866	20.70
9.4	0.70	2.38	1,870	19.46
9.9	0.66	2.30	1,850	18.26
10.4	0.62	2.16	1,841	16.98
10.9	0.57	1.95	1,833	15.66
11.4	0.52	1.68	1,824	14.23
11.9	0.47	1.42	1,813	12.72
12.4	0.42	1.15	1,795	11.13
12.9	0.32	0.84	1,781	9.41
13.4	0.20	0.49	1,764	7.32
13.9	0.08	0.18	1,679	4.67
14.4	0.01	0.03	553	1.88
14.9	0.00	0.00	0	0.19
Volume	0.59	2.27	41,908	

Table B7. Area-averaged vertical velocity and reflectivity data for 0205 UTC.

Grid Level (km)	Mean w (ms⁻¹)	Std Dev w (ms⁻¹)	Points Sampled	Mean Reflectivity (dBZ)
0.9	0.15	2.17	823	30.21
1.4	0.02	2.31	1,570	30.96
1.9	0.00	2.34	1,570	31.29
2.4	0.10	2.35	1,573	31.69
2.9	0.26	2.39	1,573	32.14
3.4	0.50	2.54	1,595	32.07
3.9	0.80	2.76	1,615	30.62
4.4	1.04	2.95	1,659	28.38
4.9	1.19	3.14	1,703	27.19
5.4	1.28	3.30	1,707	26.60
5.9	1.35	3.41	1,712	26.09
6.4	1.38	3.48	1,740	25.49
6.9	1.36	3.50	1,741	24.76
7.4	1.28	3.40	1,741	23.90
7.9	1.16	3.19	1,741	22.90
8.4	1.01	2.94	1,741	21.74
8.9	0.88	2.68	1,728	20.44
9.4	0.77	2.47	1,711	19.06
9.9	0.68	2.32	1,695	17.53
10.4	0.62	2.20	1,681	15.99
10.9	0.60	2.04	1,664	14.46
11.4	0.59	1.79	1,649	12.92
11.9	0.56	1.45	1,632	11.41
12.4	0.48	1.06	1,613	9.88
12.9	0.37	0.69	1,595	8.24
13.4	0.22	0.36	1,551	6.27
13.9	0.05	0.14	1,116	3.80
14.4	0.00	0.02	193	1.56
14.9	0.00	0.00	0	0.28
Volume	0.72	2.59	43,632	

APPENDIX C

HISTOGRAMS OF VERTICAL VELOCITY MAGNITUDES

The following histograms of upward and downward vertical motion distributions were computed at 1 ms^{-1} interval of vertical velocity. Velocities with magnitude less than 1ms^{-1} were excluded. Upward motions and downward motions were treated separately The values on the abscissa represent the midpoint of each velocity increment. Velocities with magnitudes larger than 10 ms^{-1} downward or 16 ms^{-1} upward were included in the last velocity increment (i.e. 15 to 16 ms^{-1} for upward velocities and -9 to -10 ms^{-1} for downward velocities).

Two bar charts showing Relative Frequency (%) versus Vertical Velocity (m/s) for "0.9 km Upward".

Top chart legend: 0122 UTC, 0129 UTC, 0134 UTC.

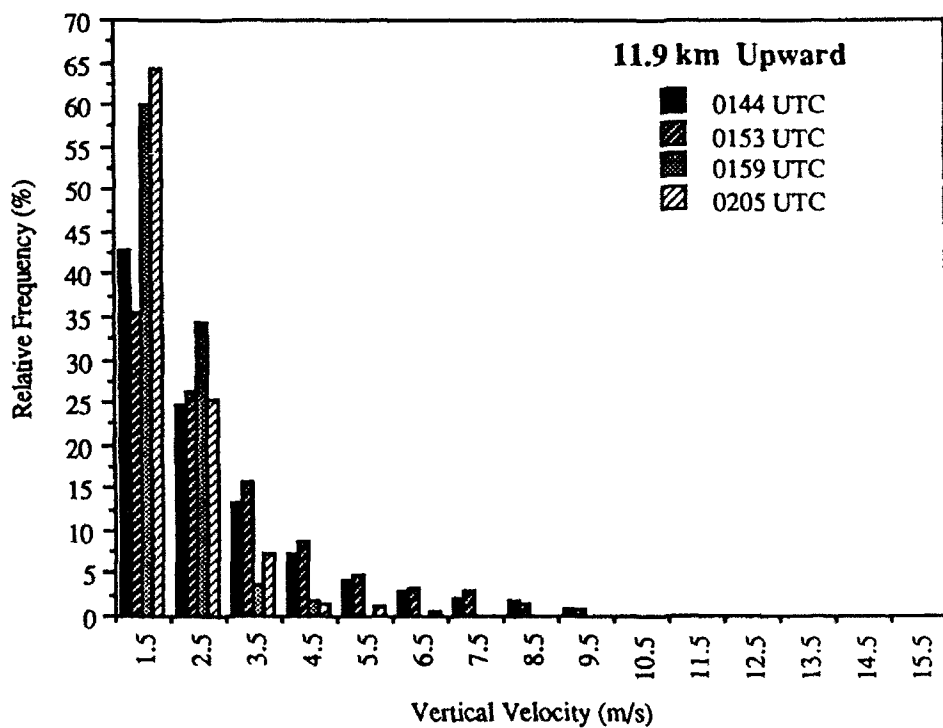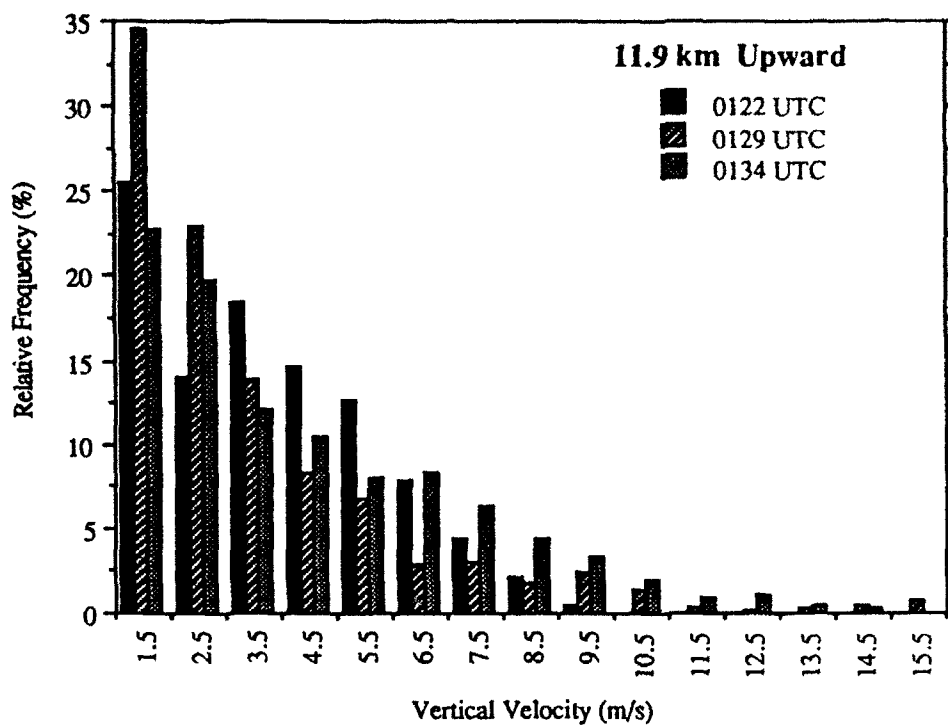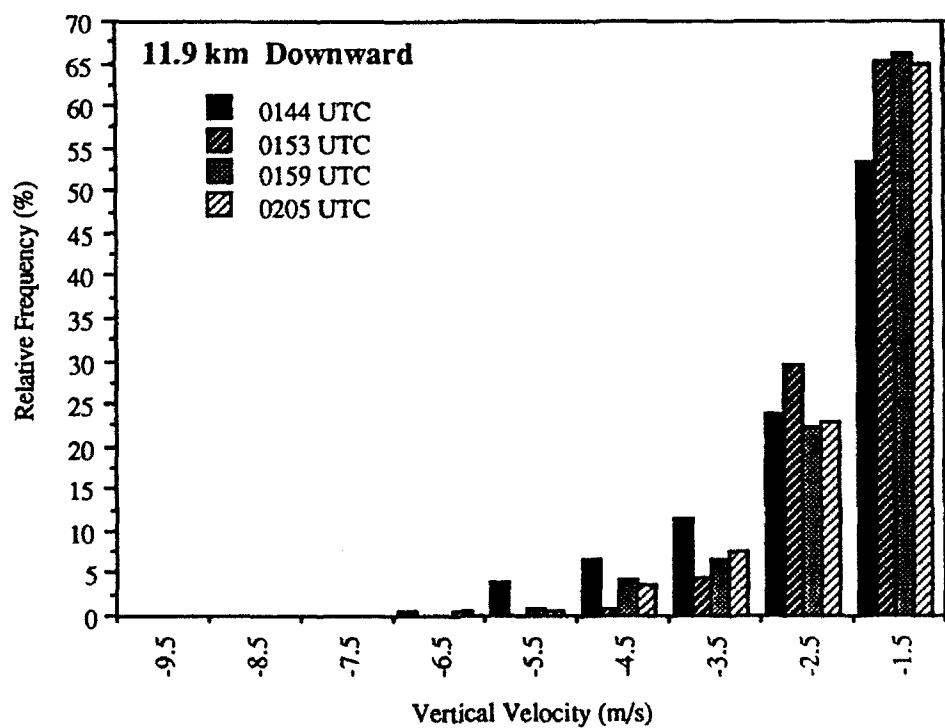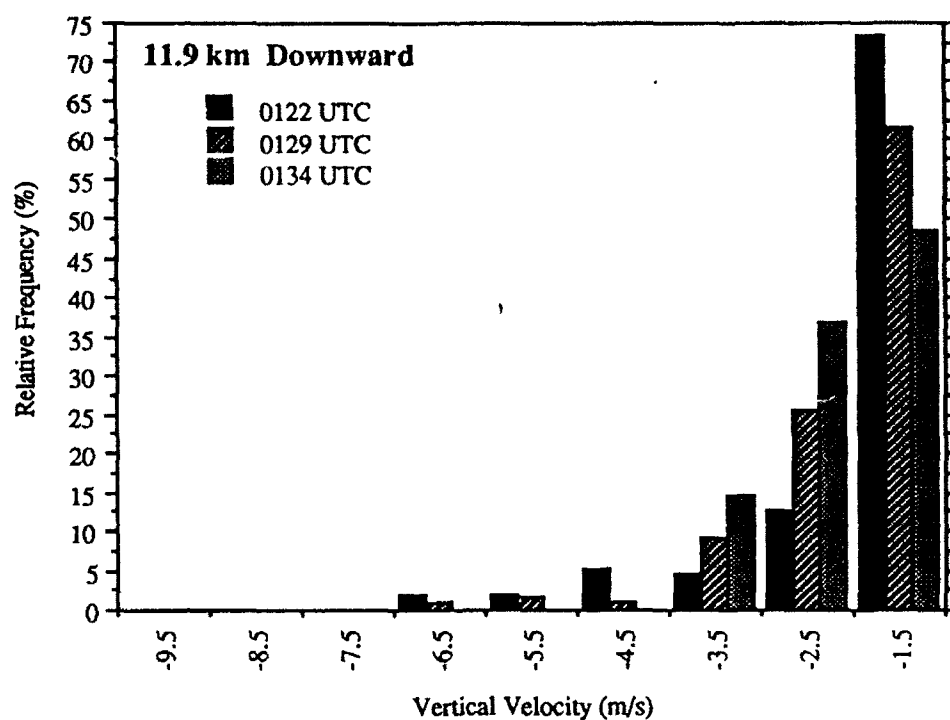Bottom chart legend: 0144 UTC, 0153 UTC, 0159 UTC, 0205 UTC.
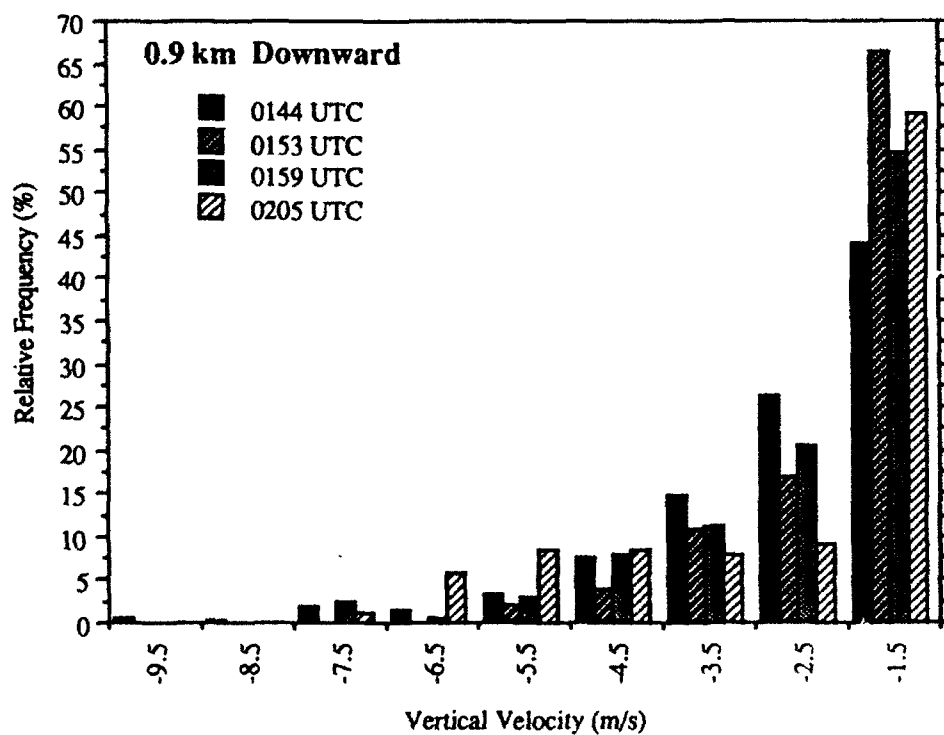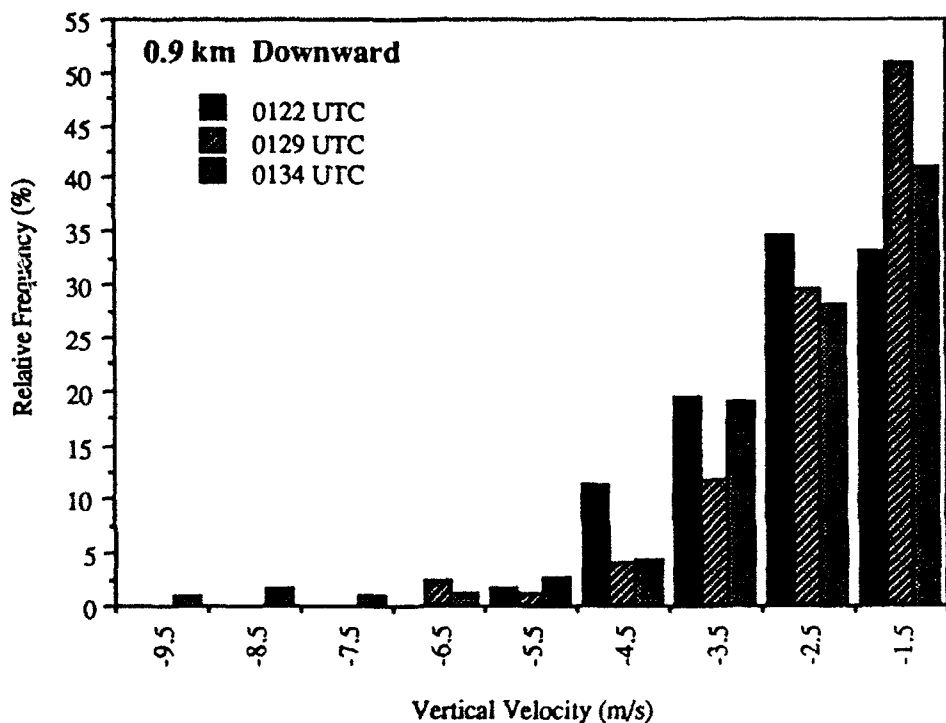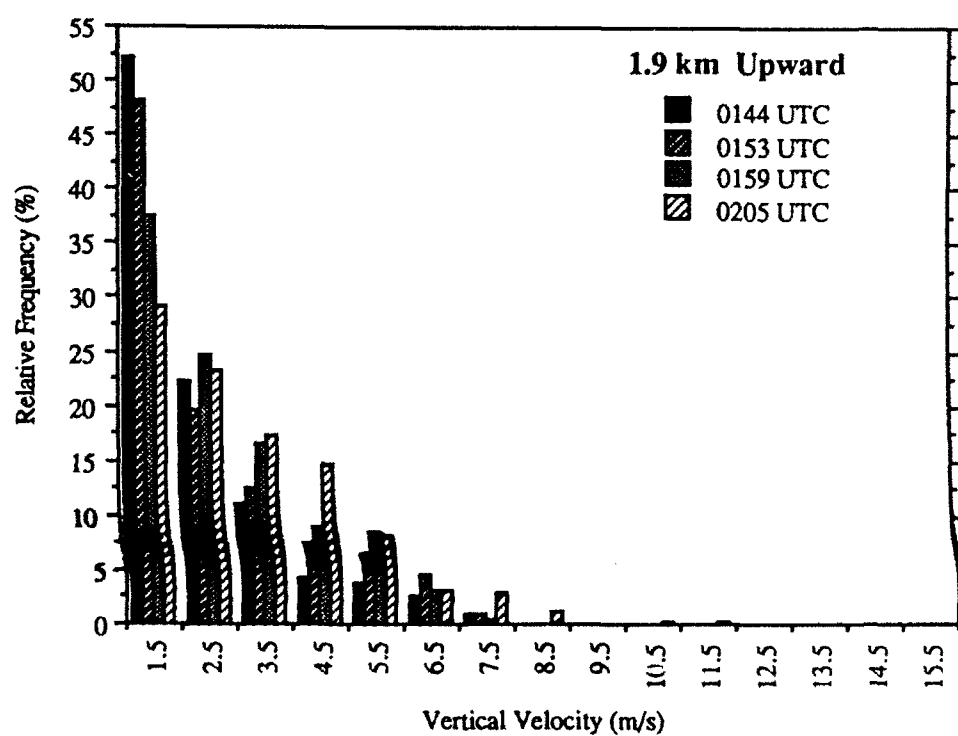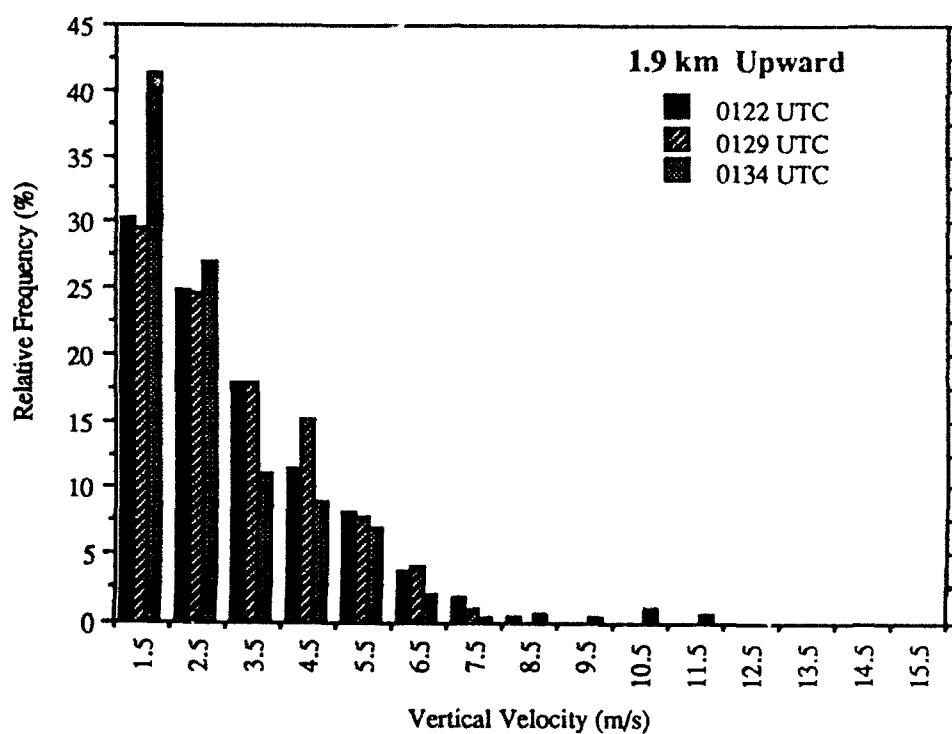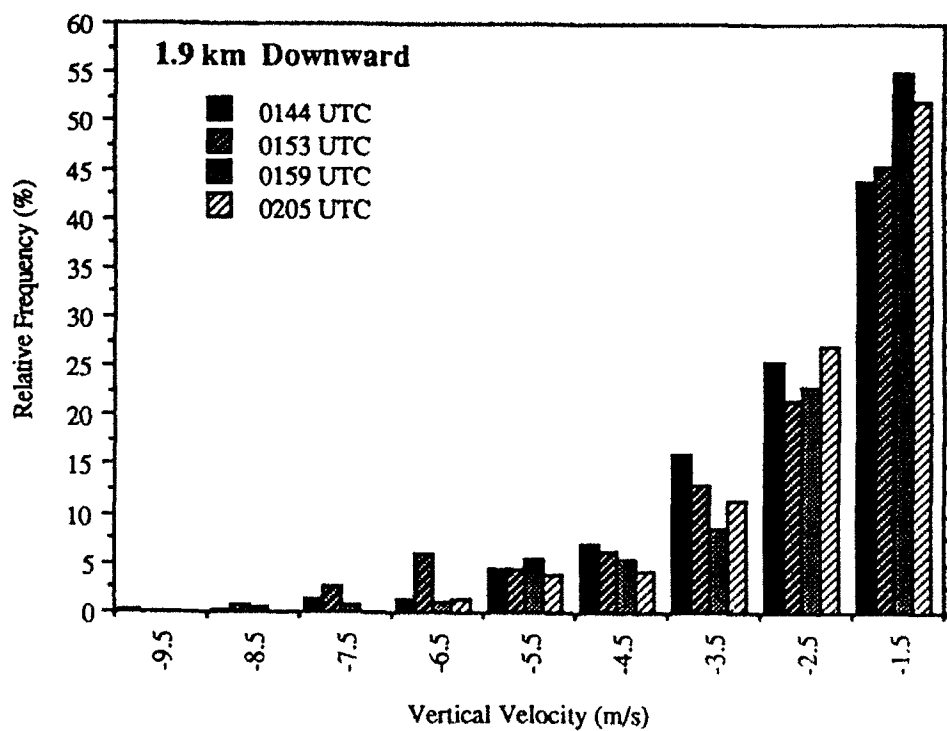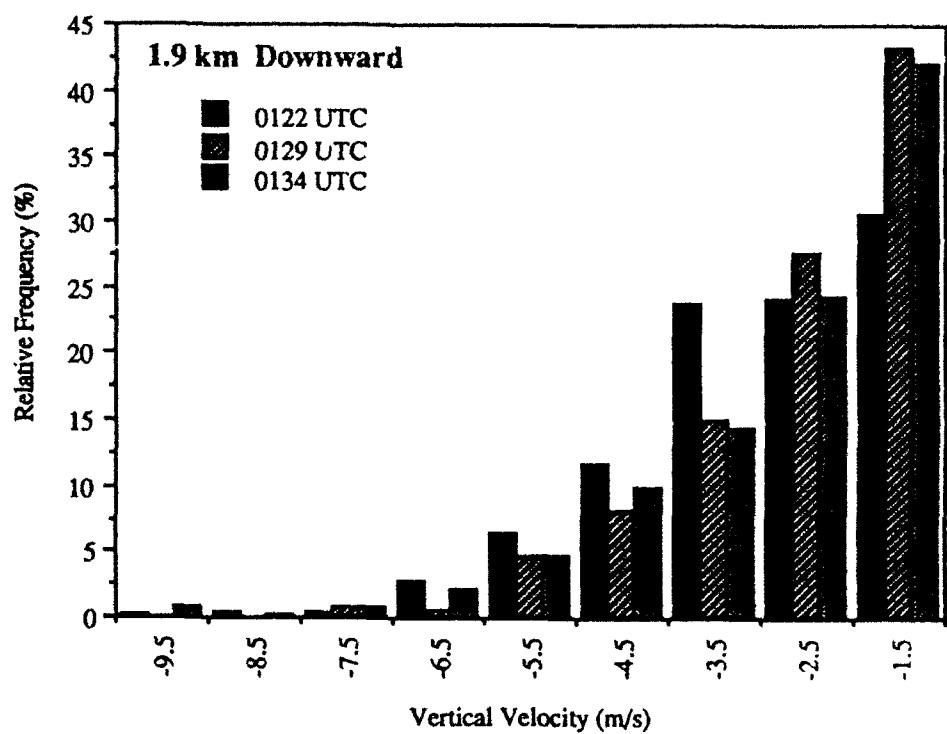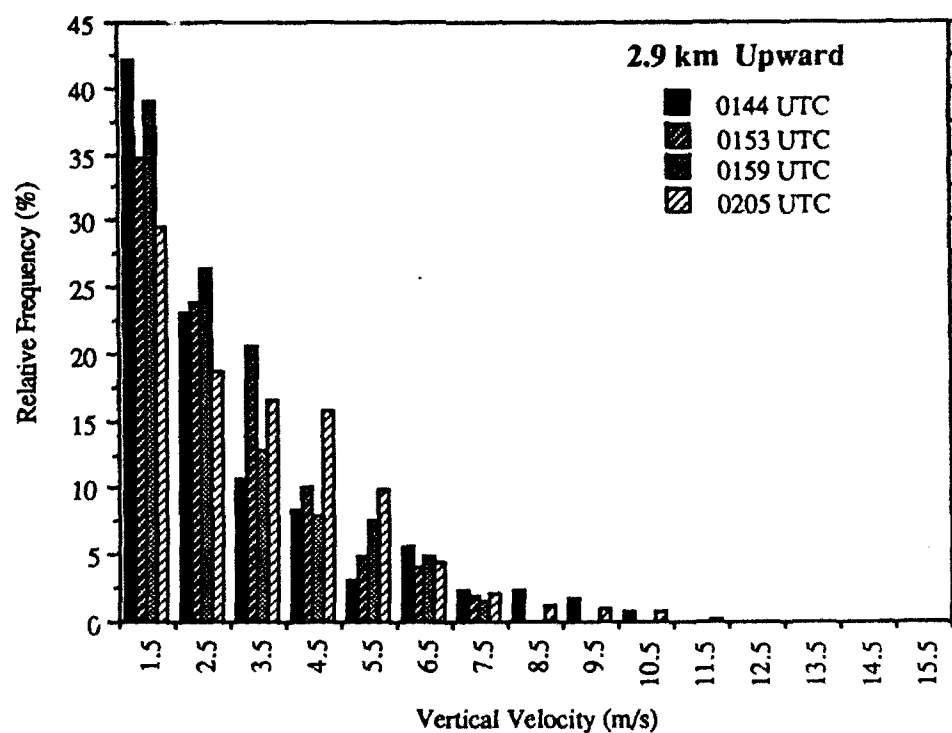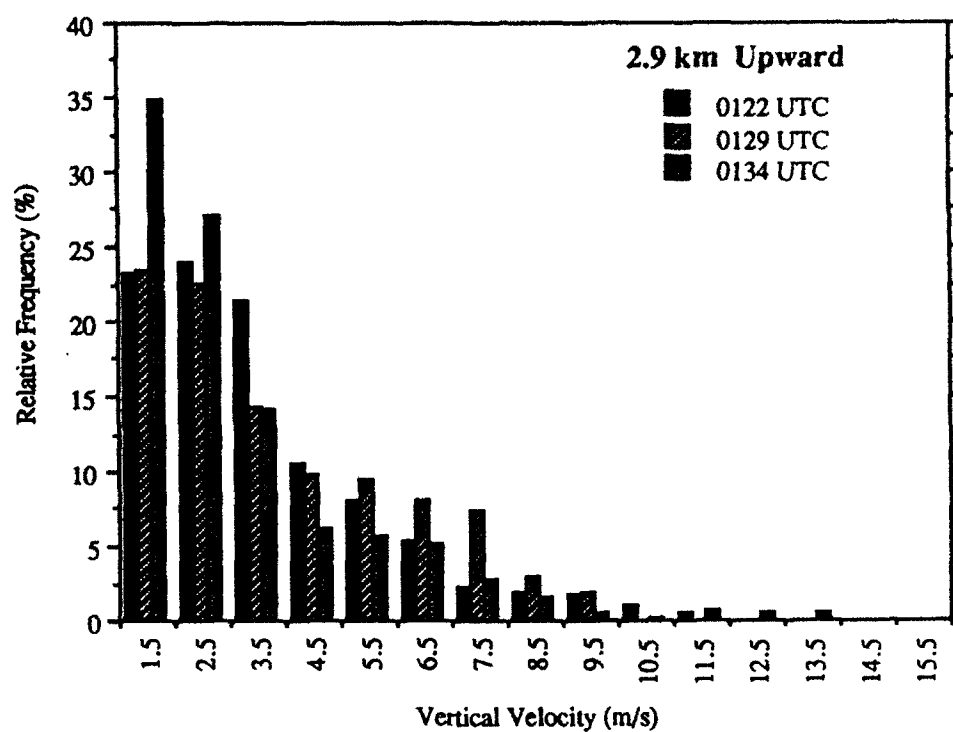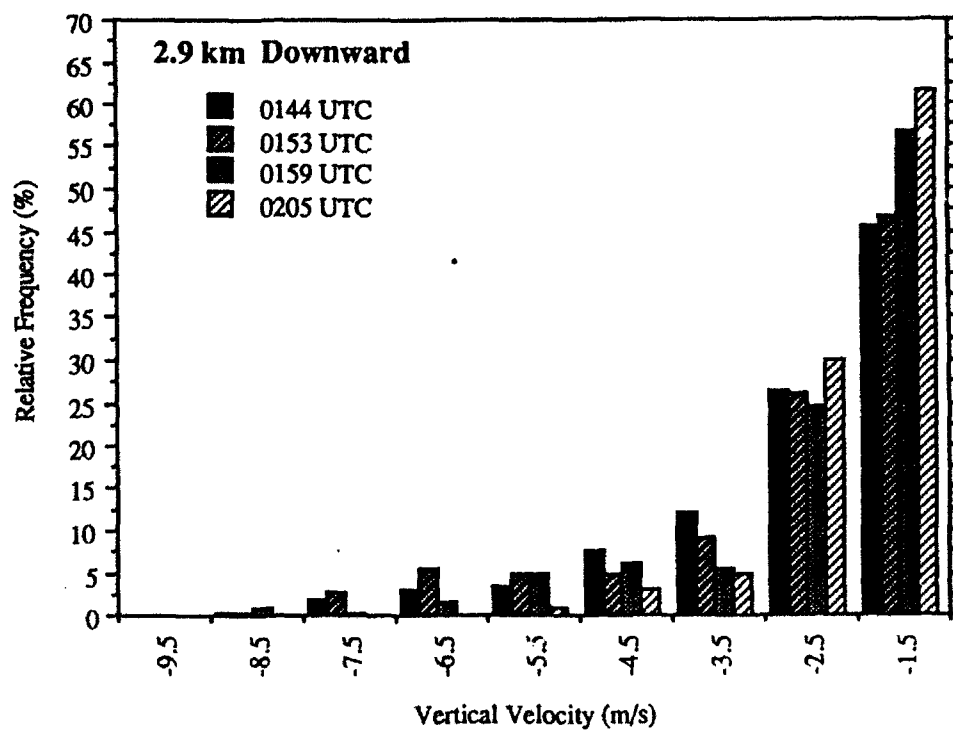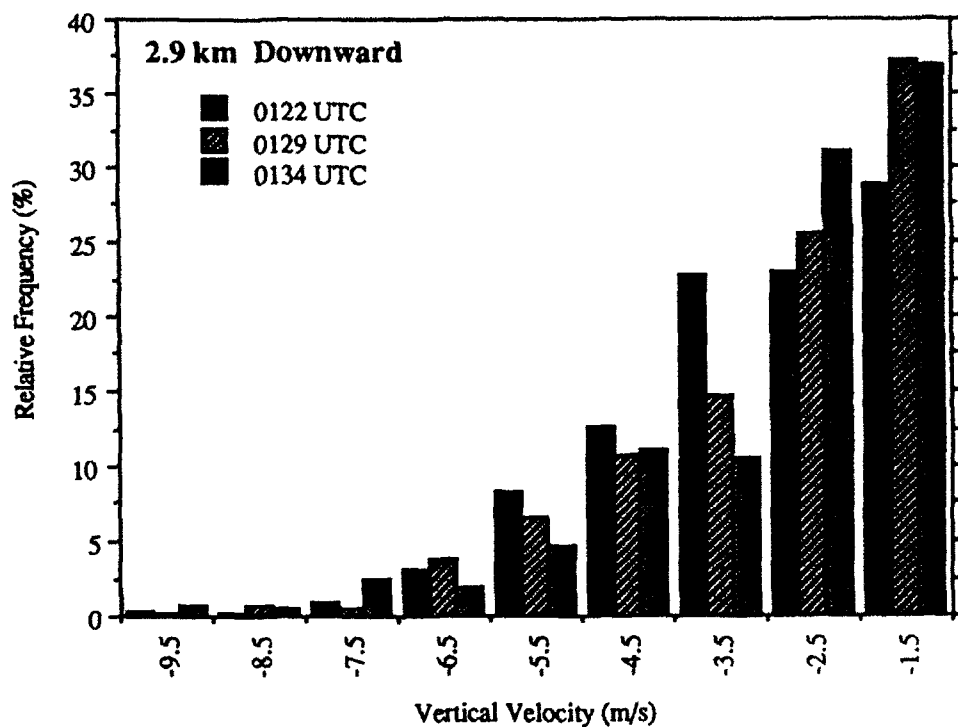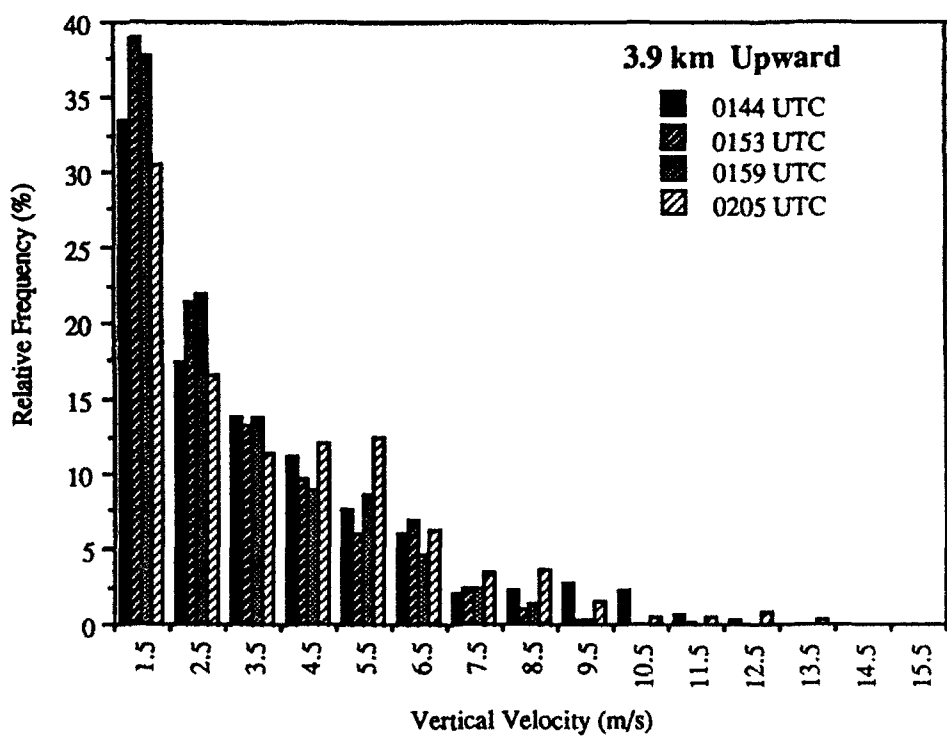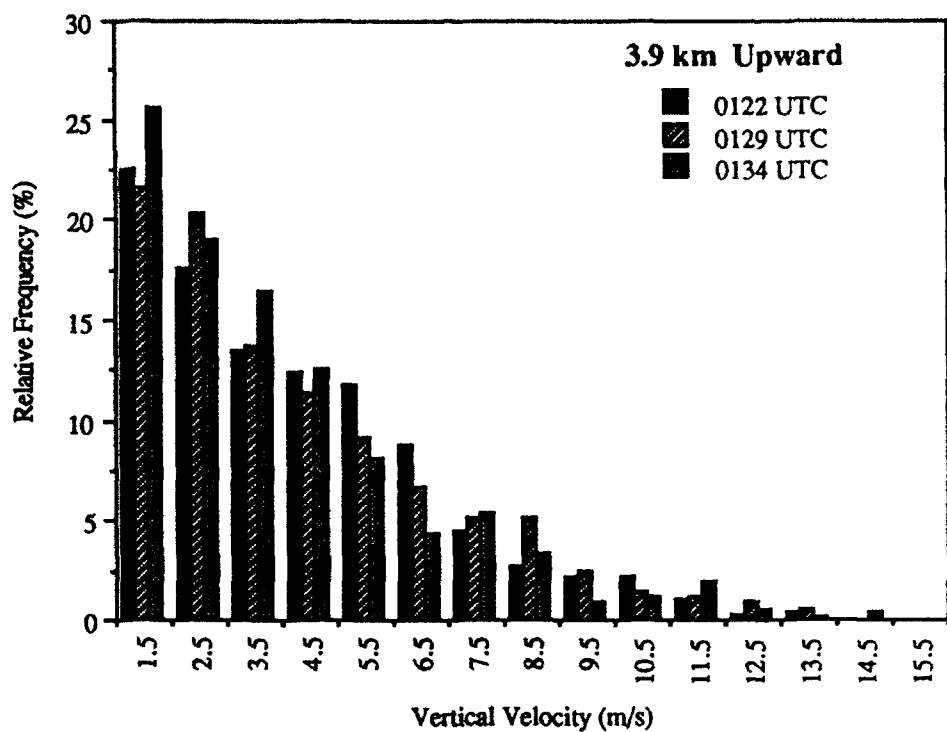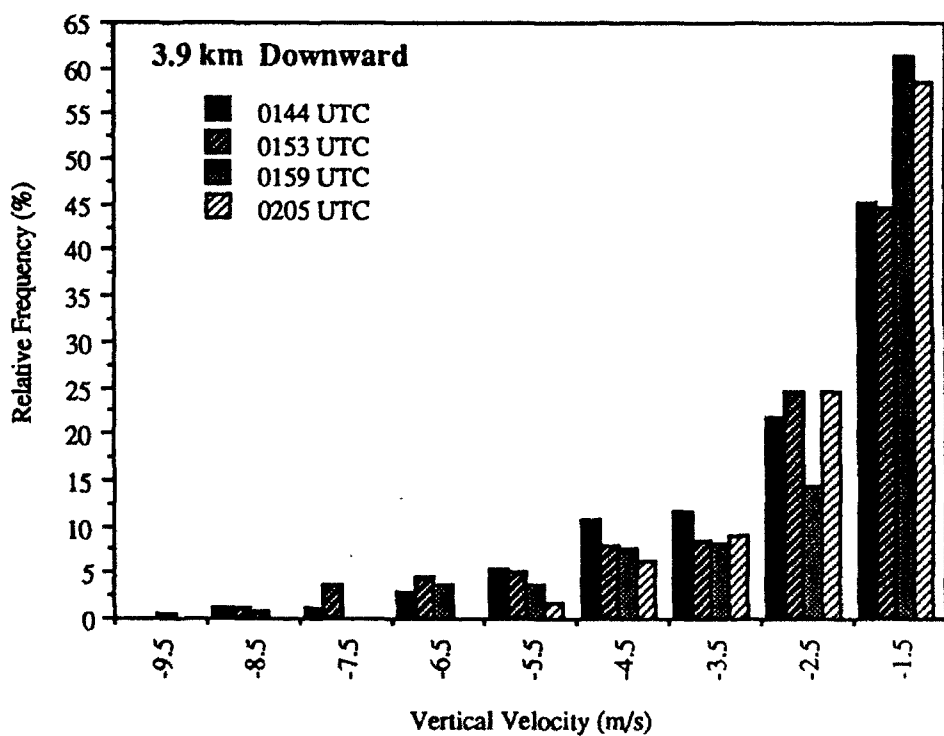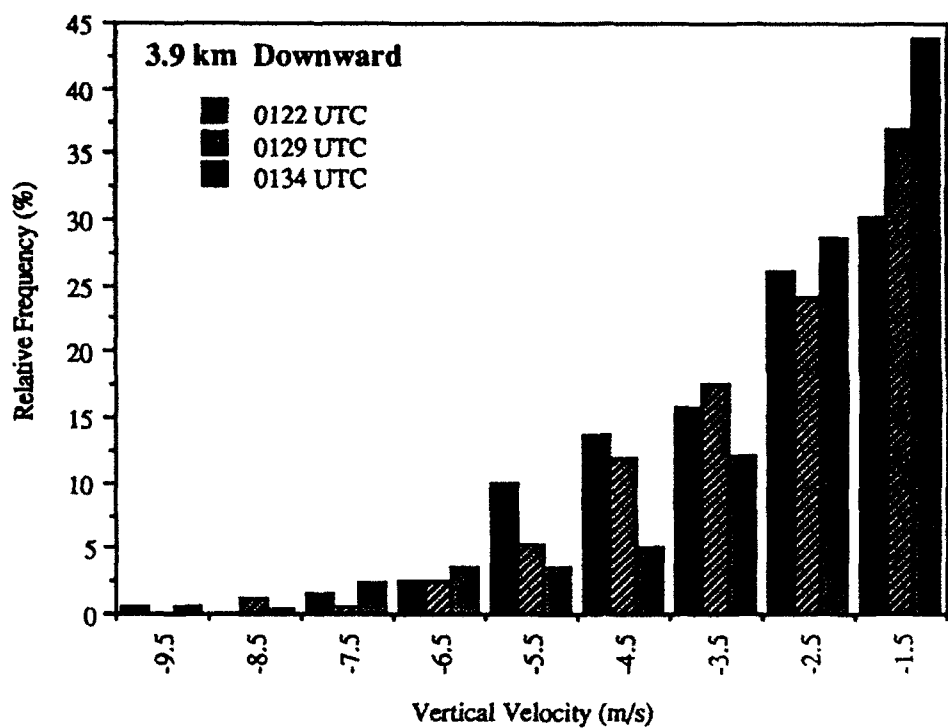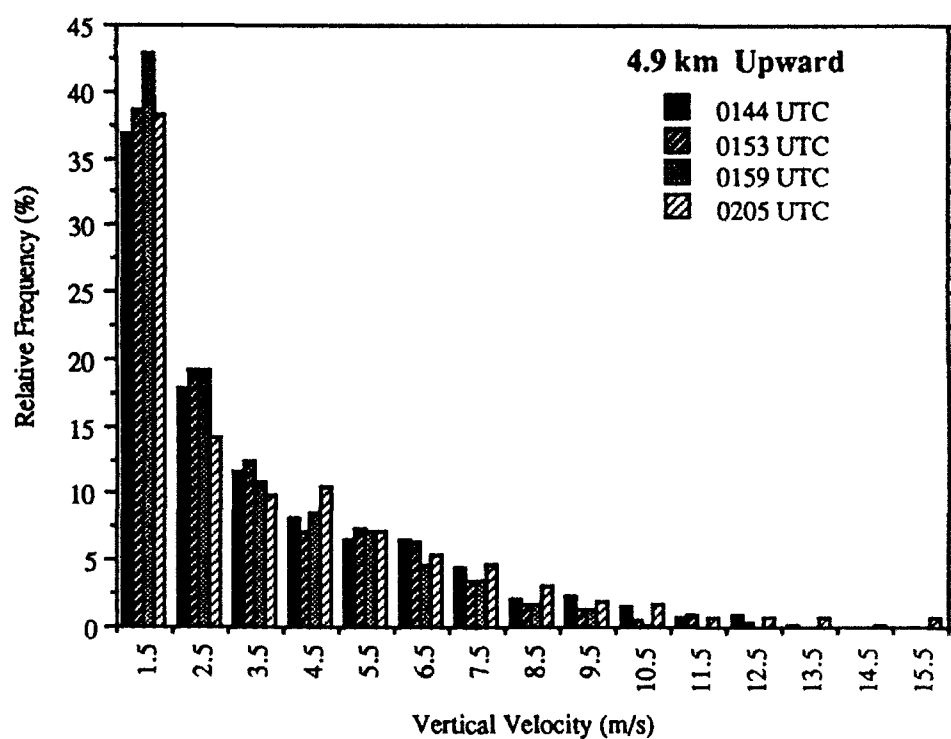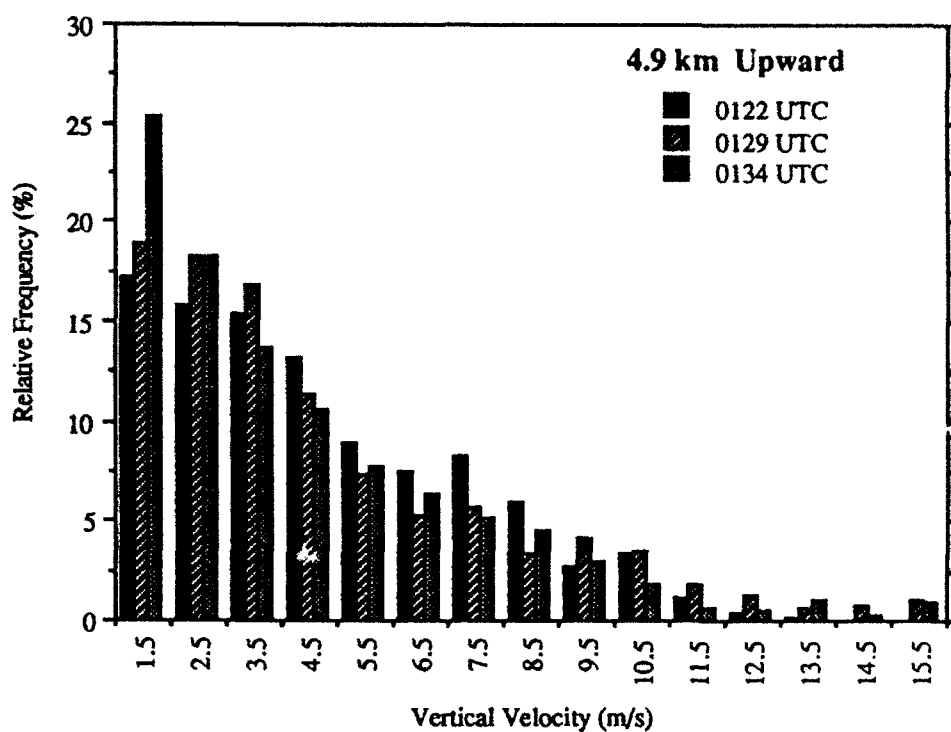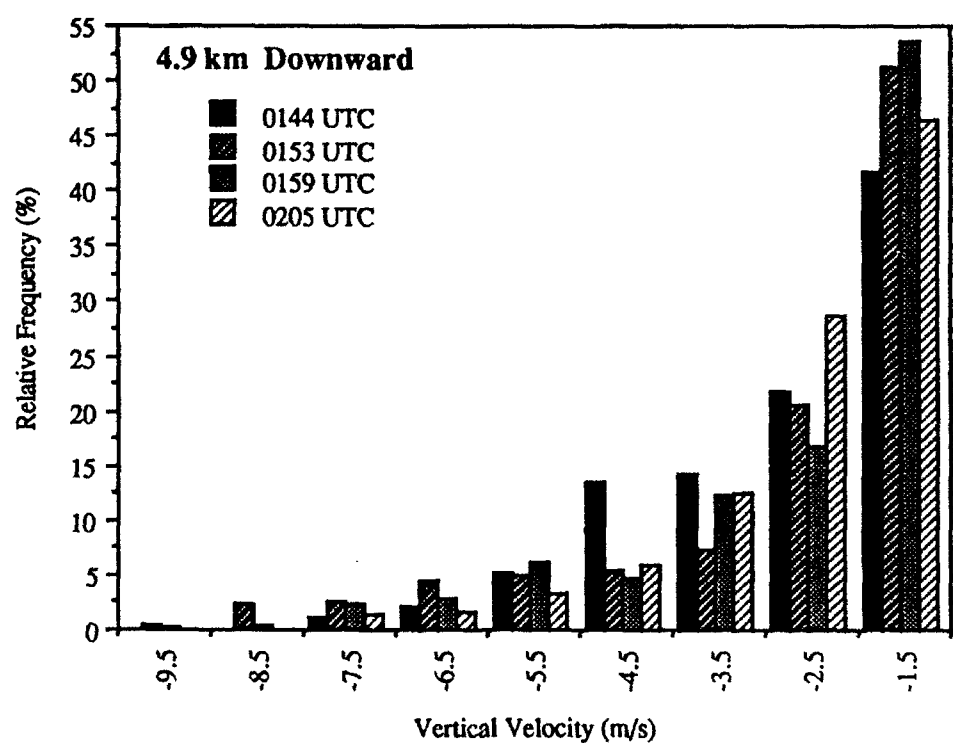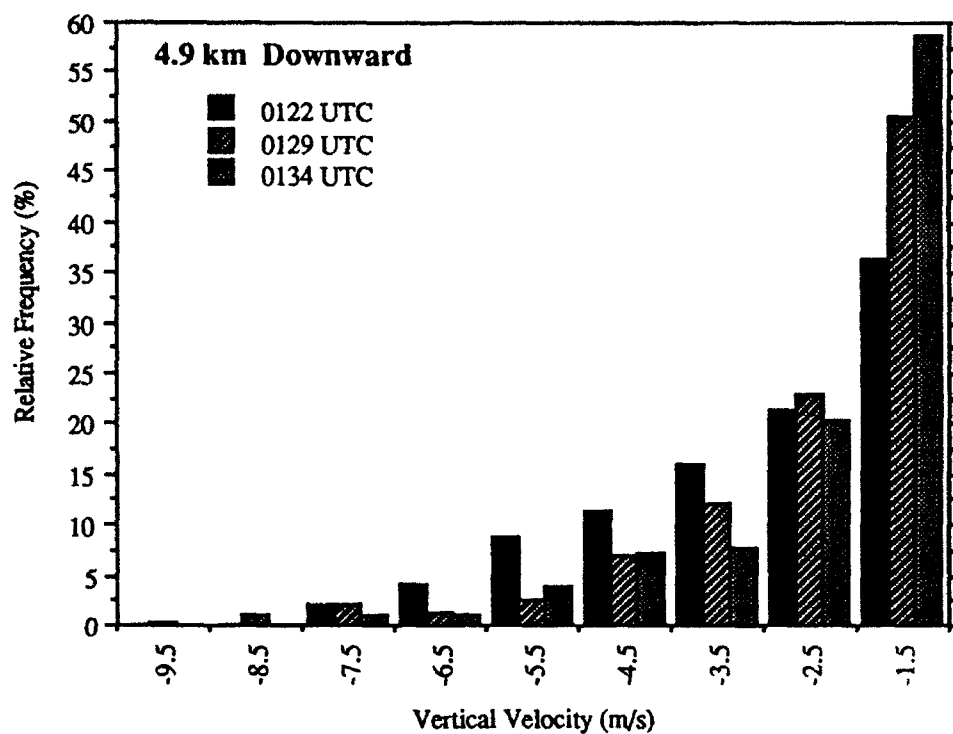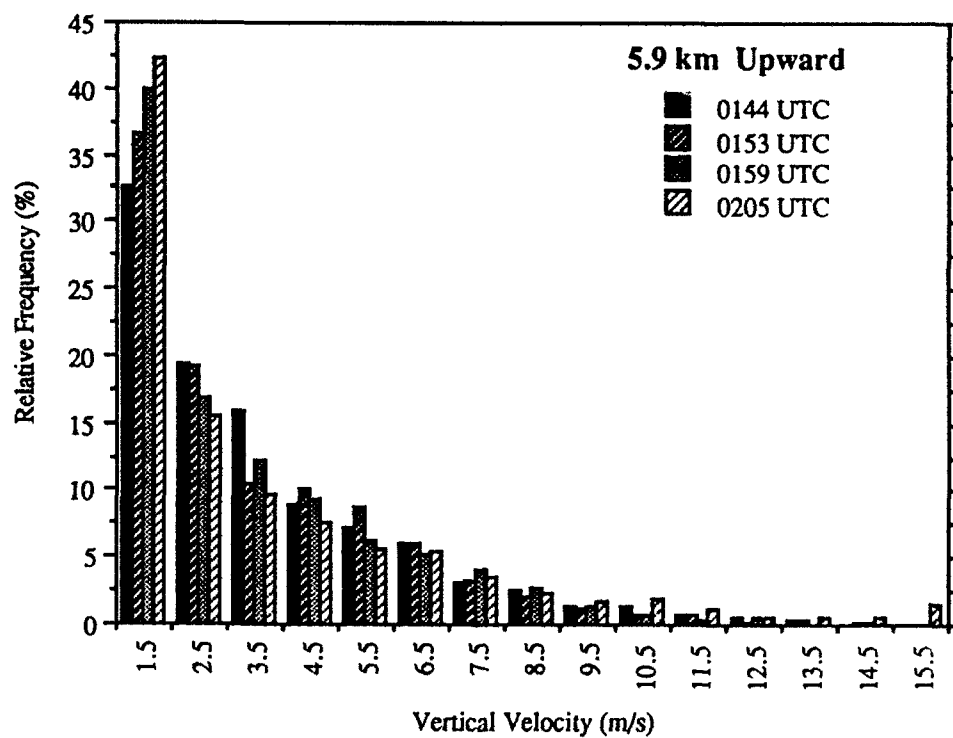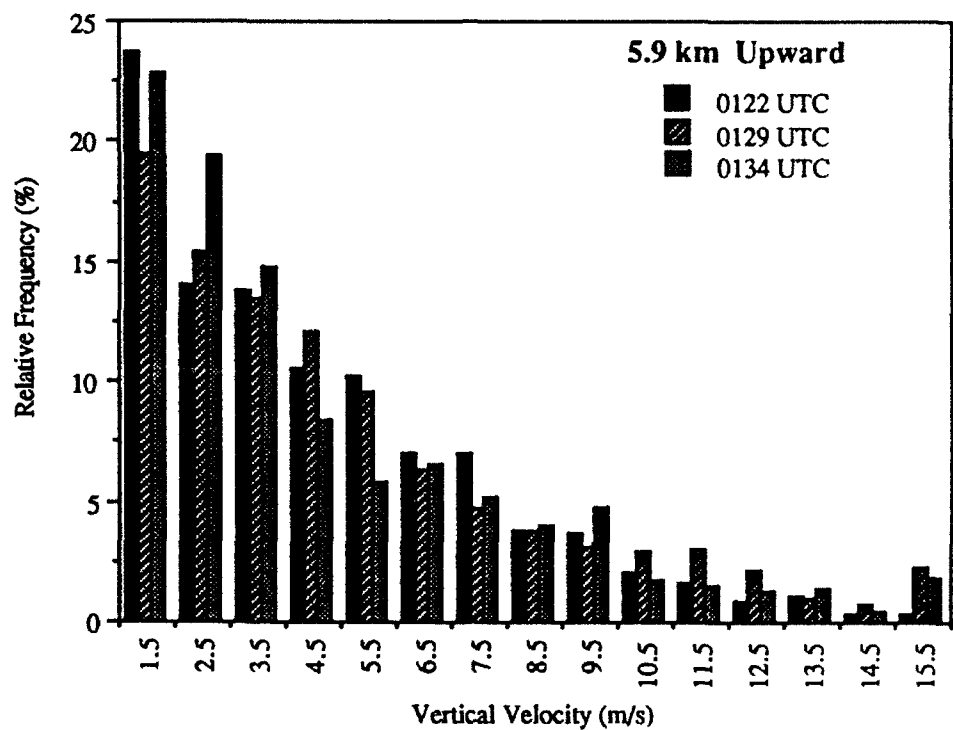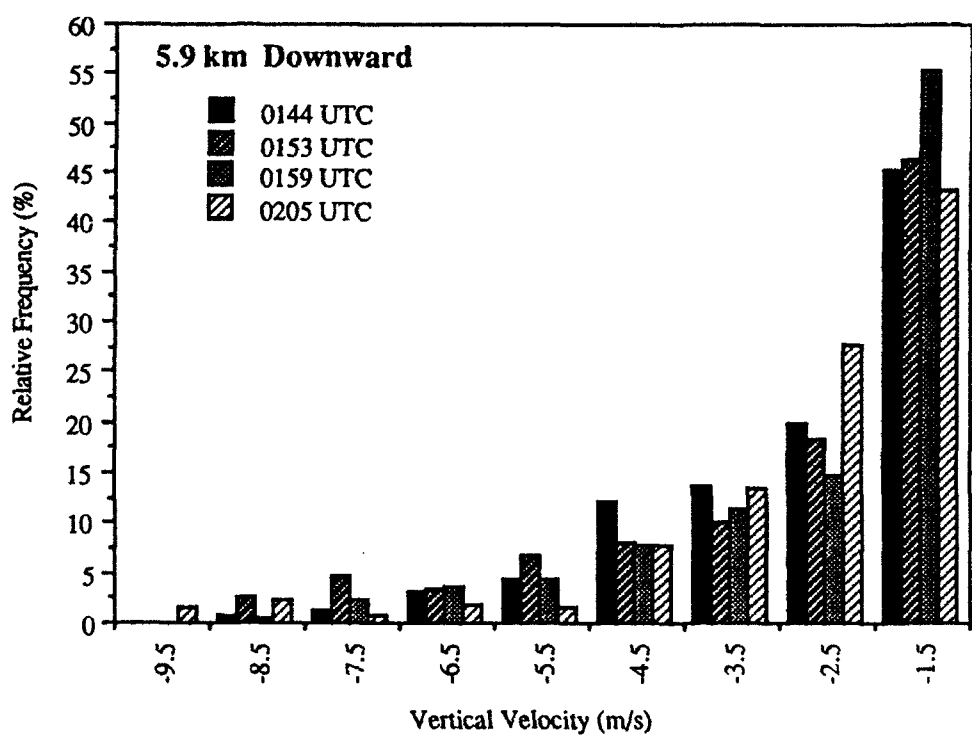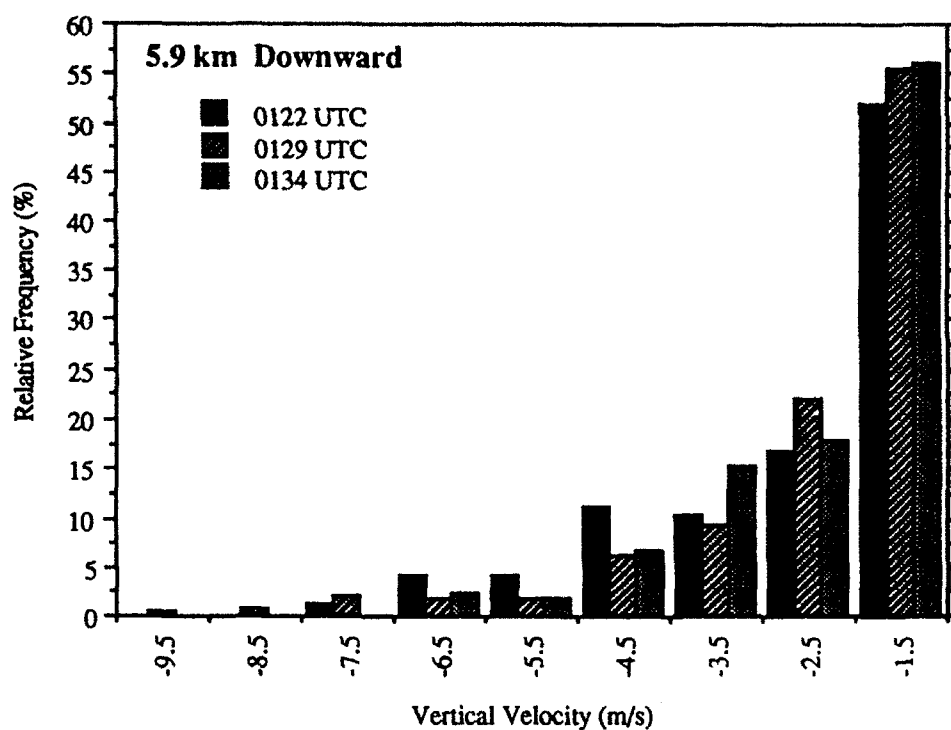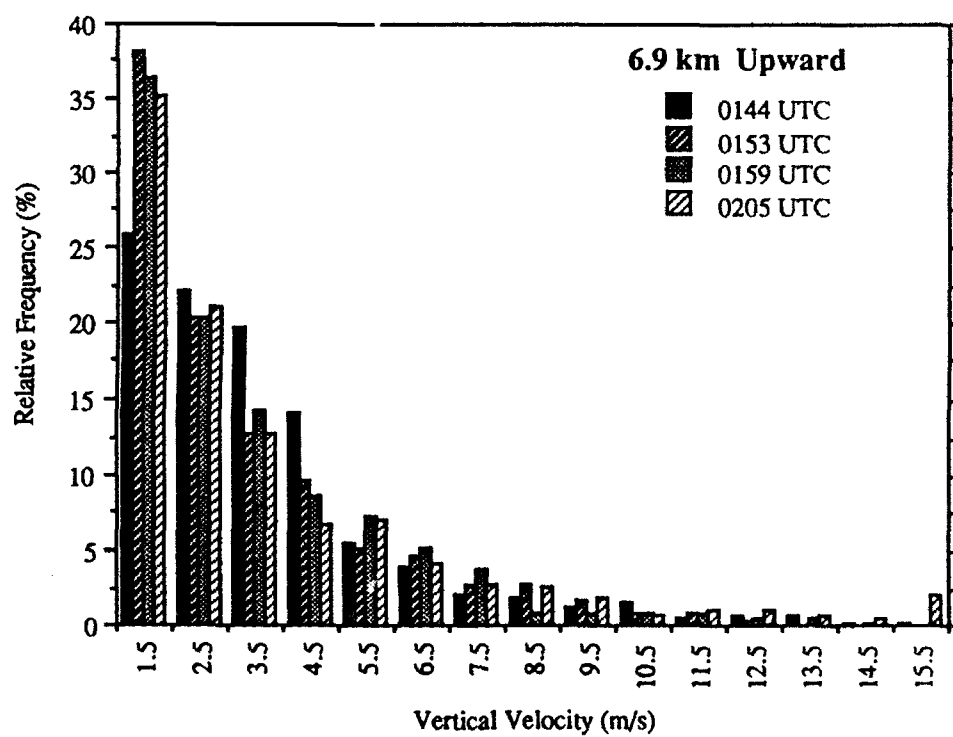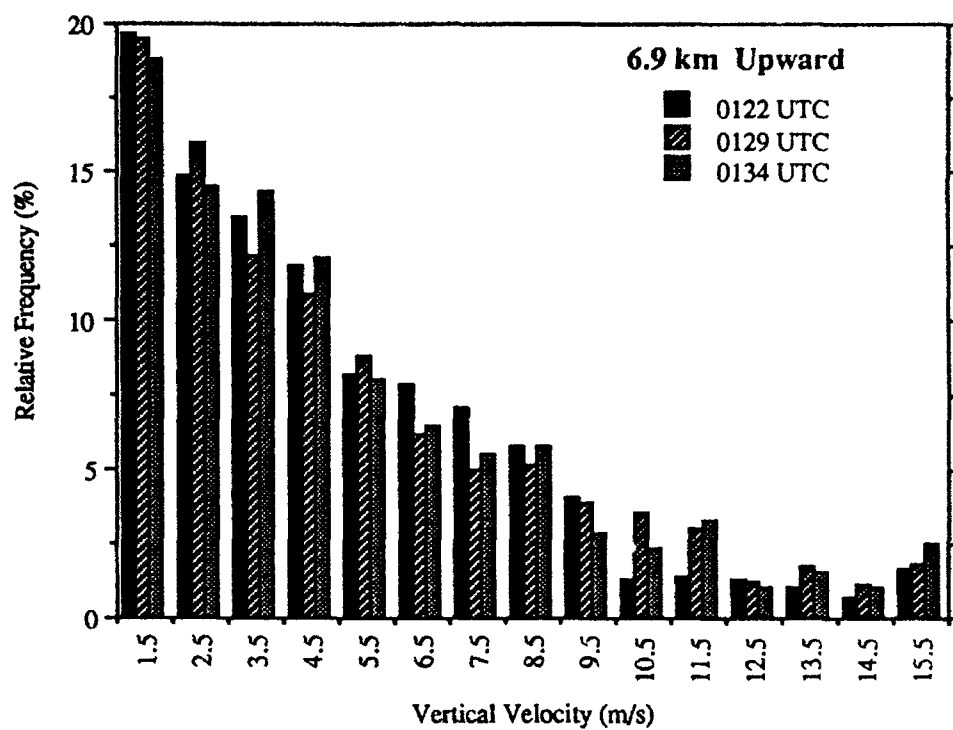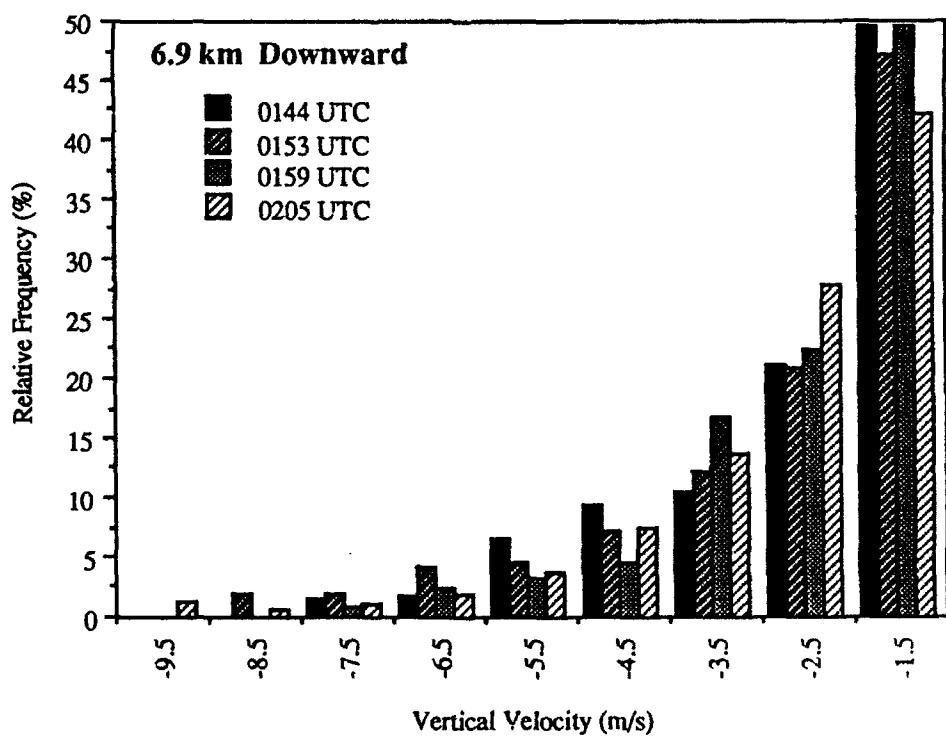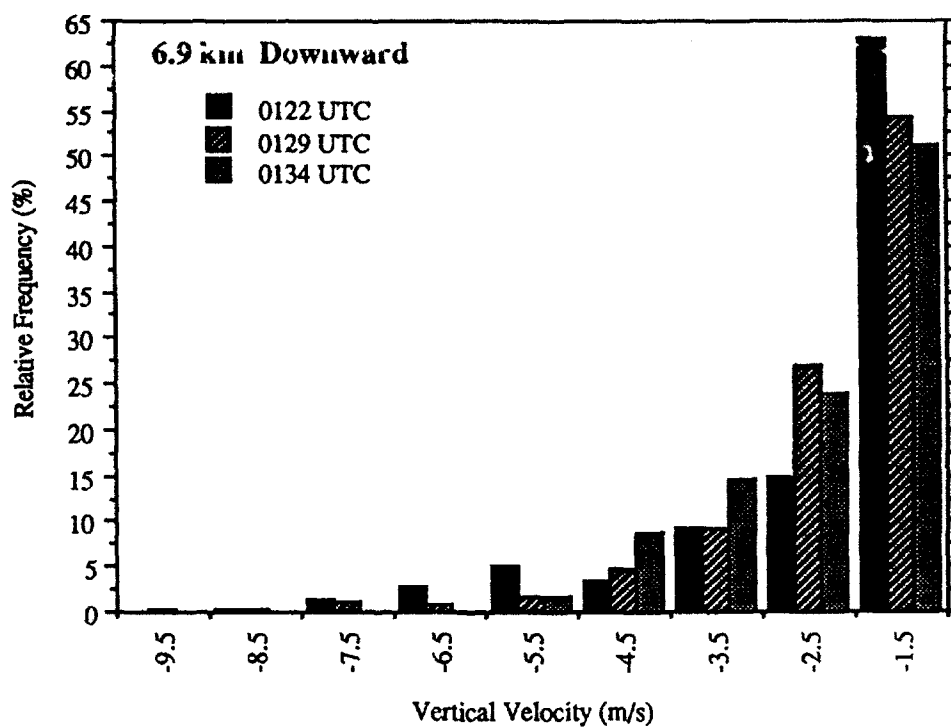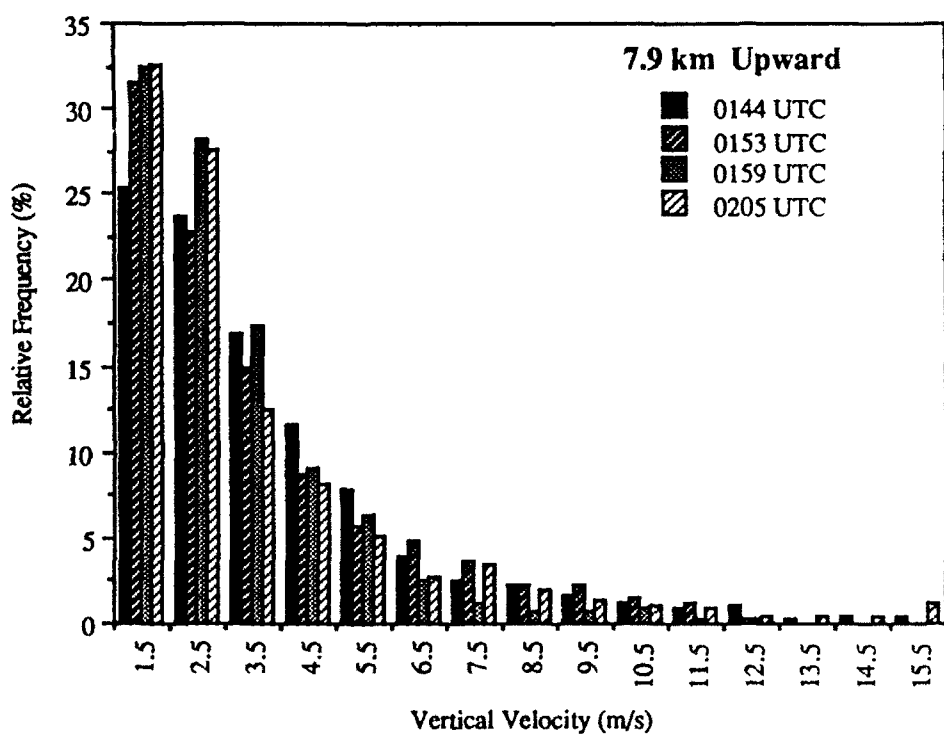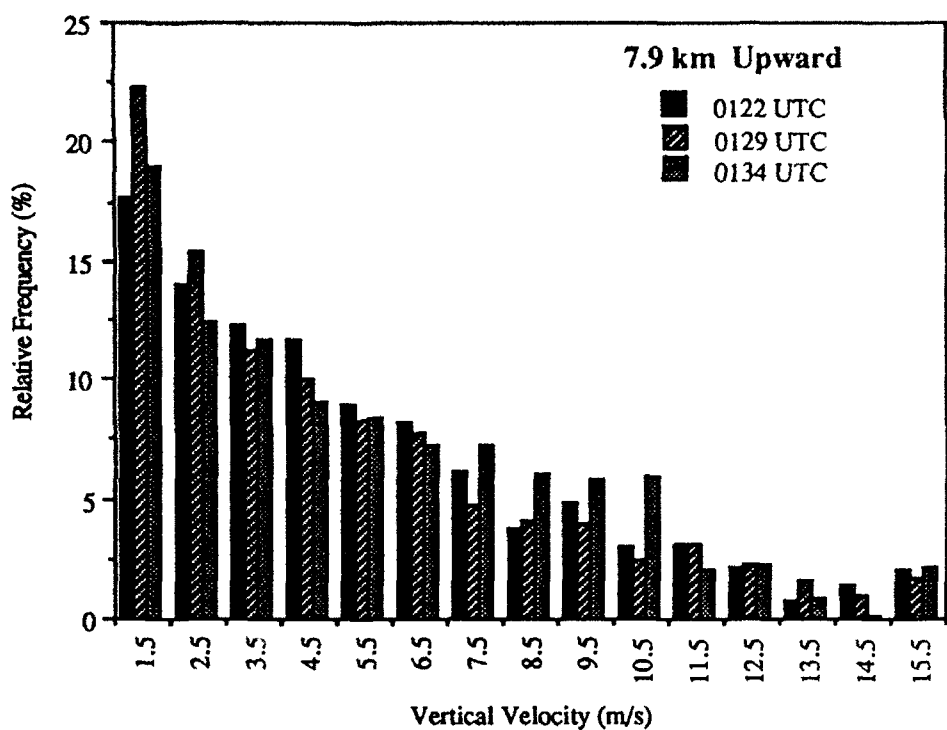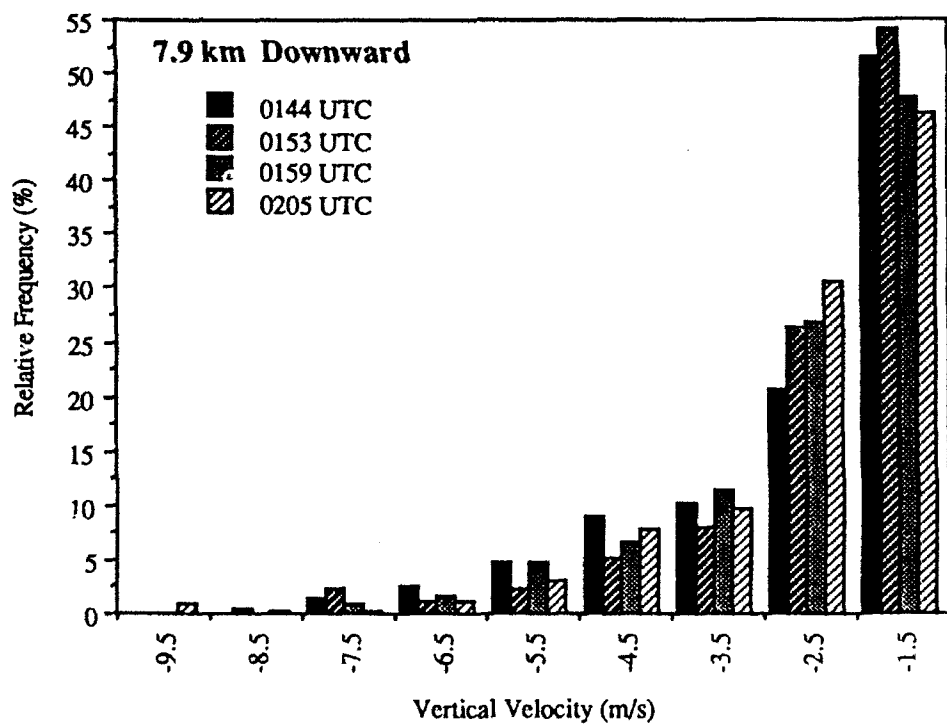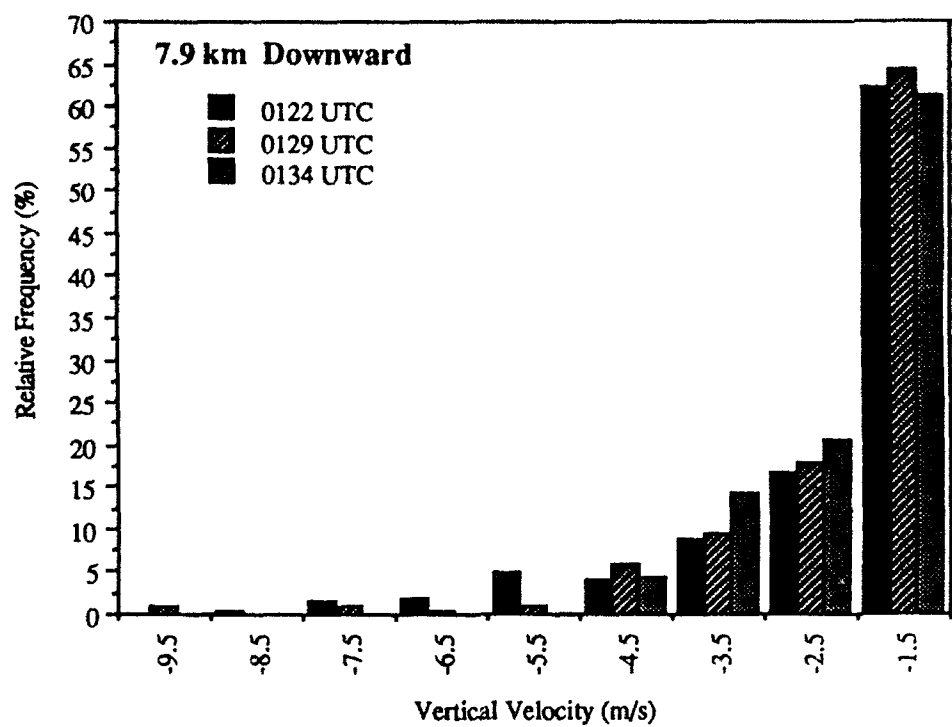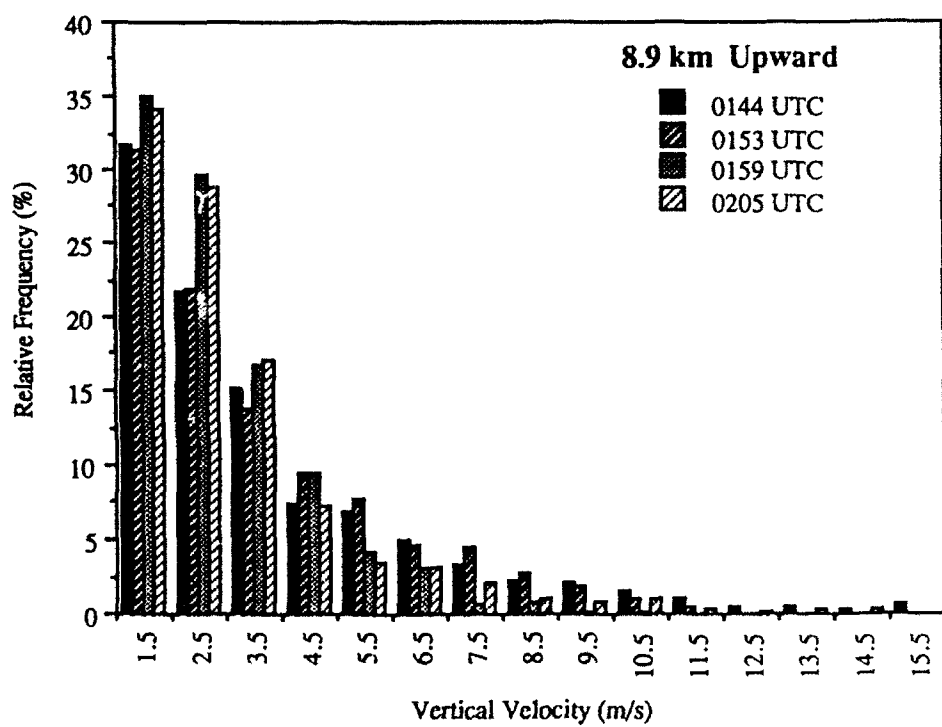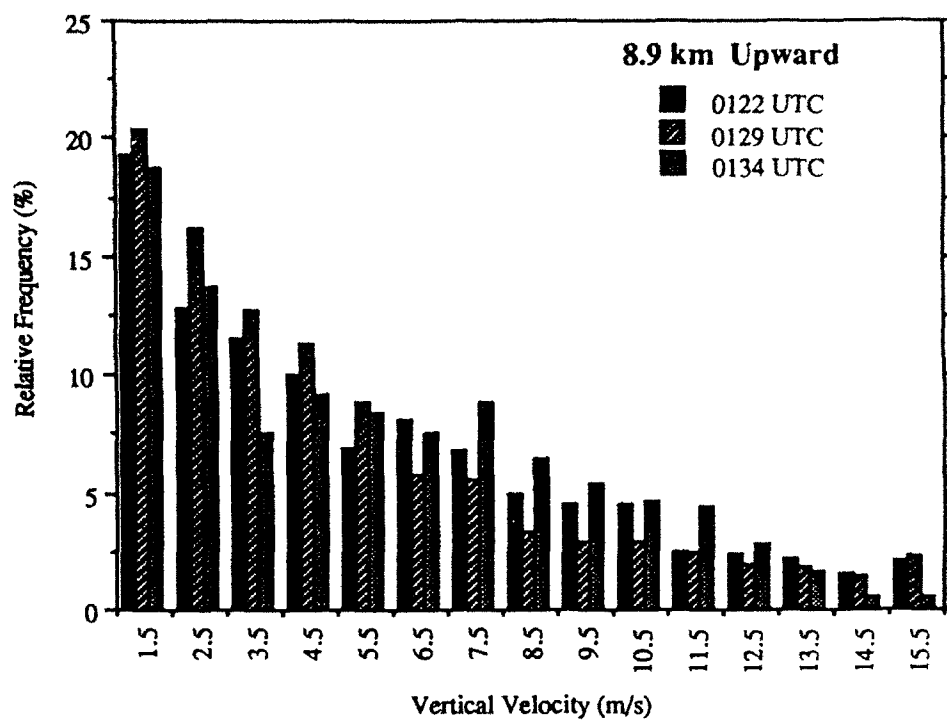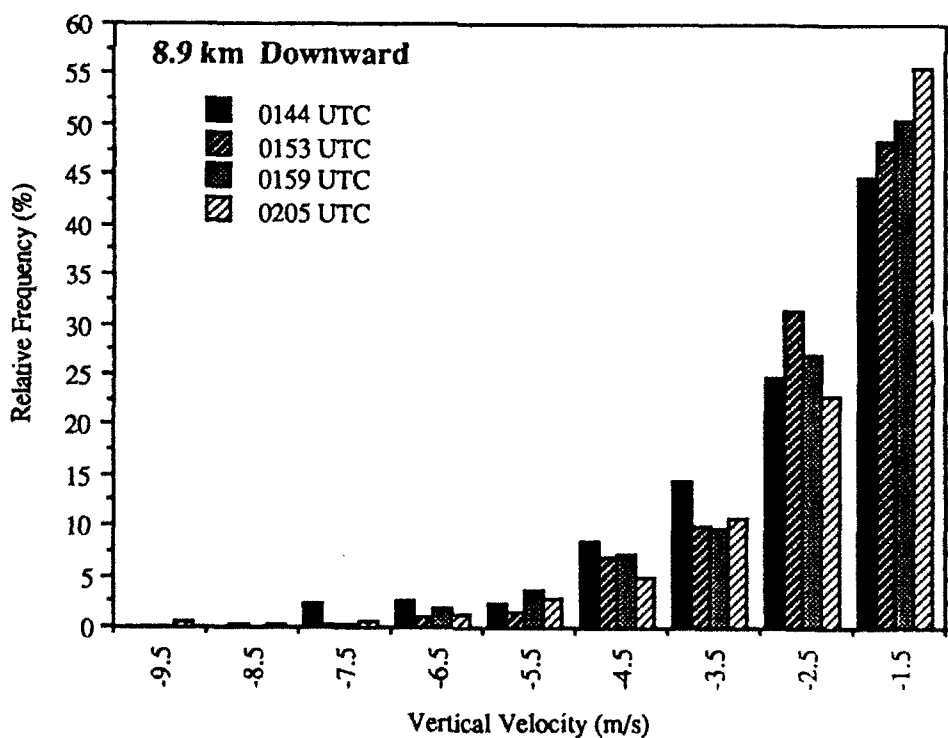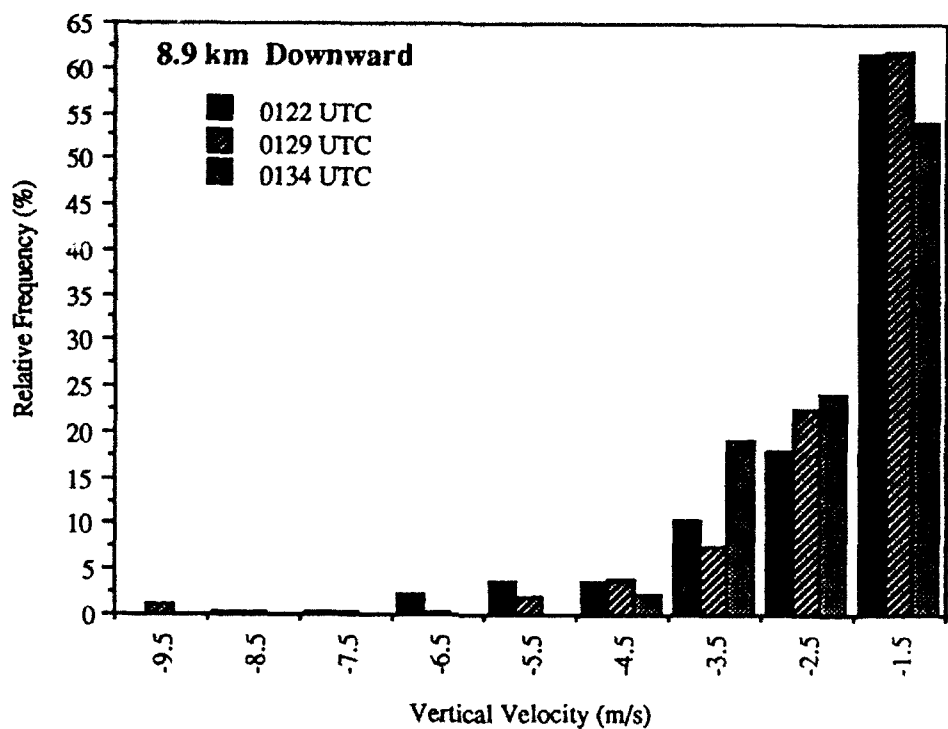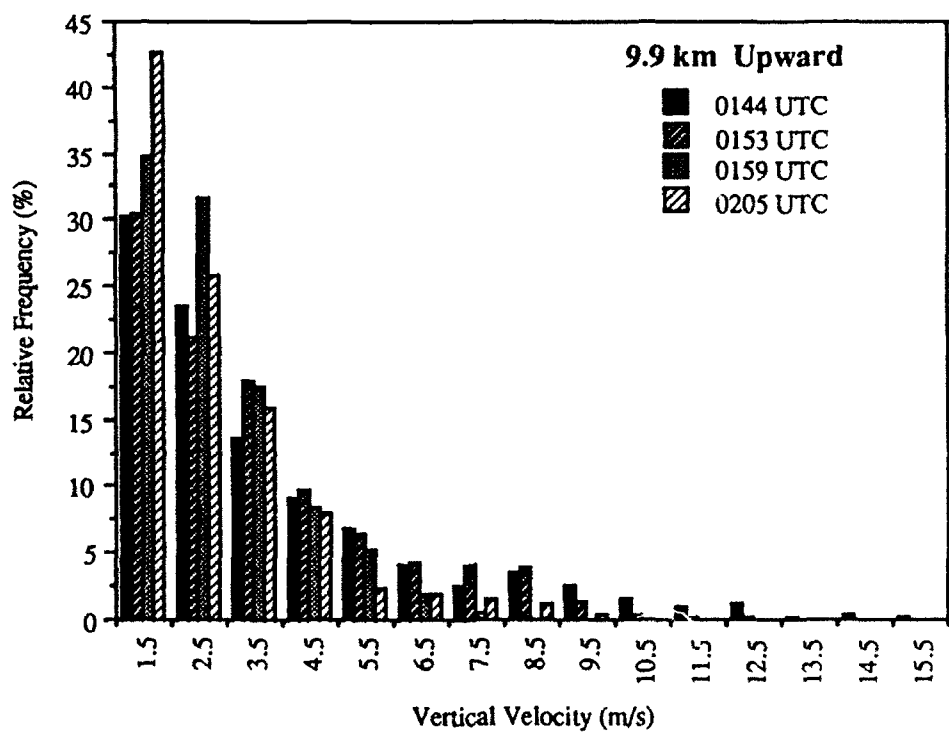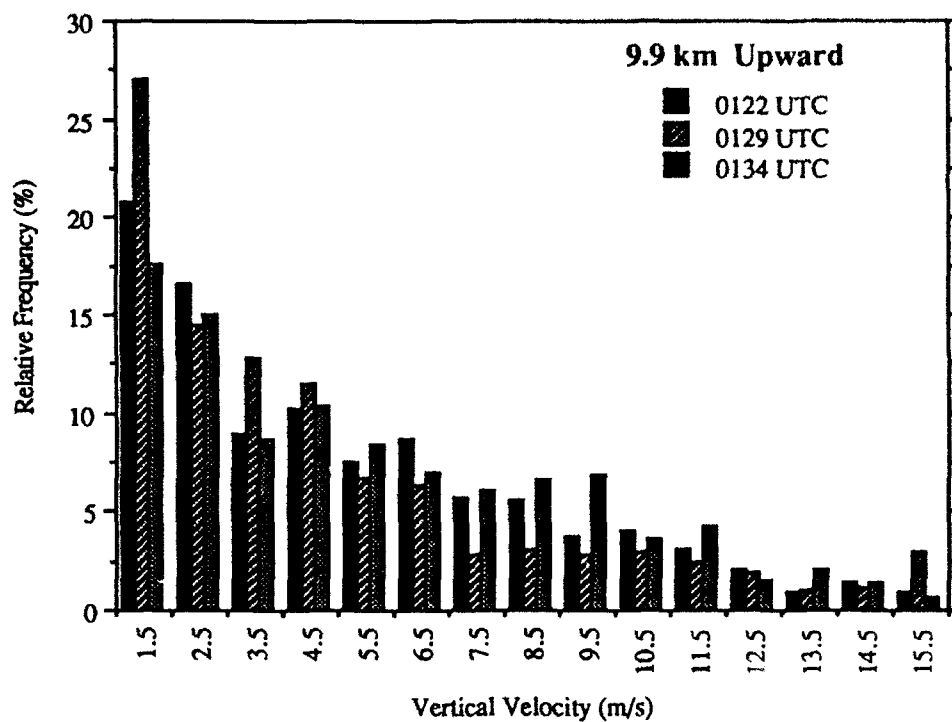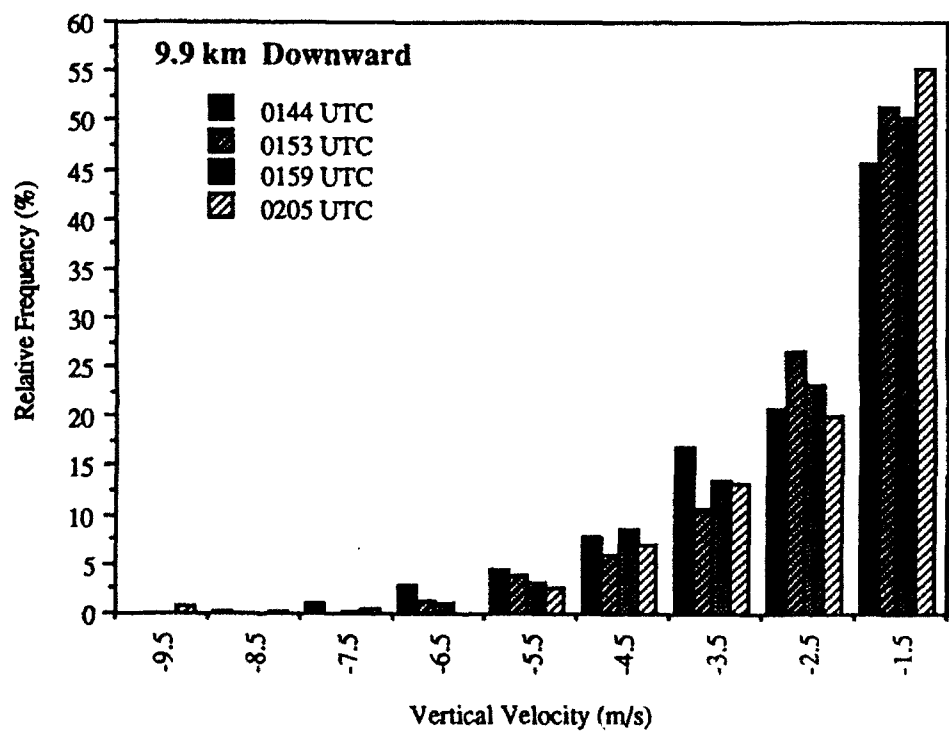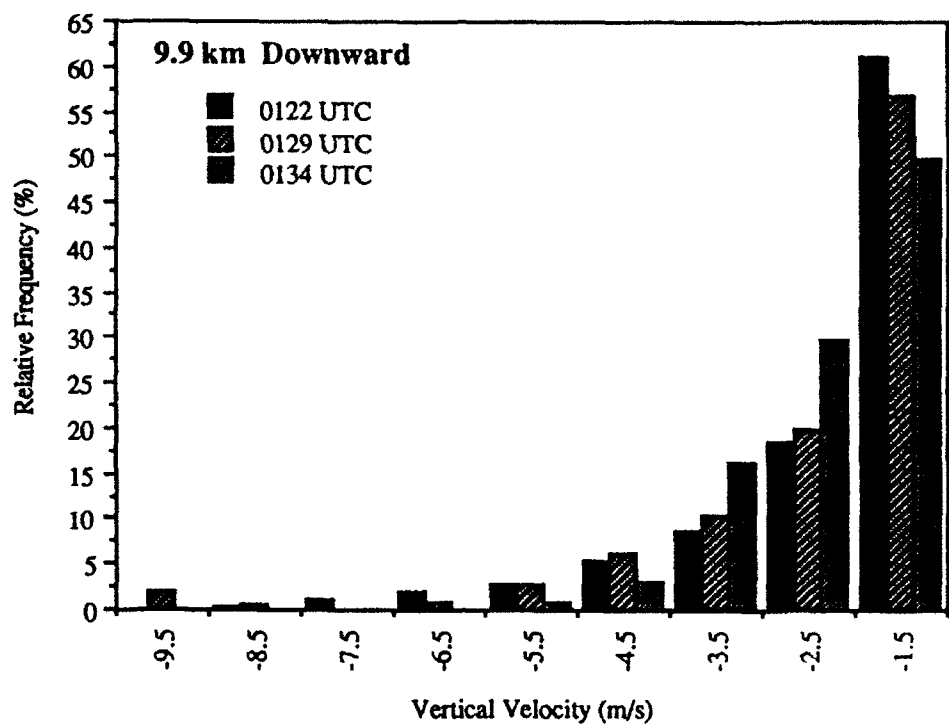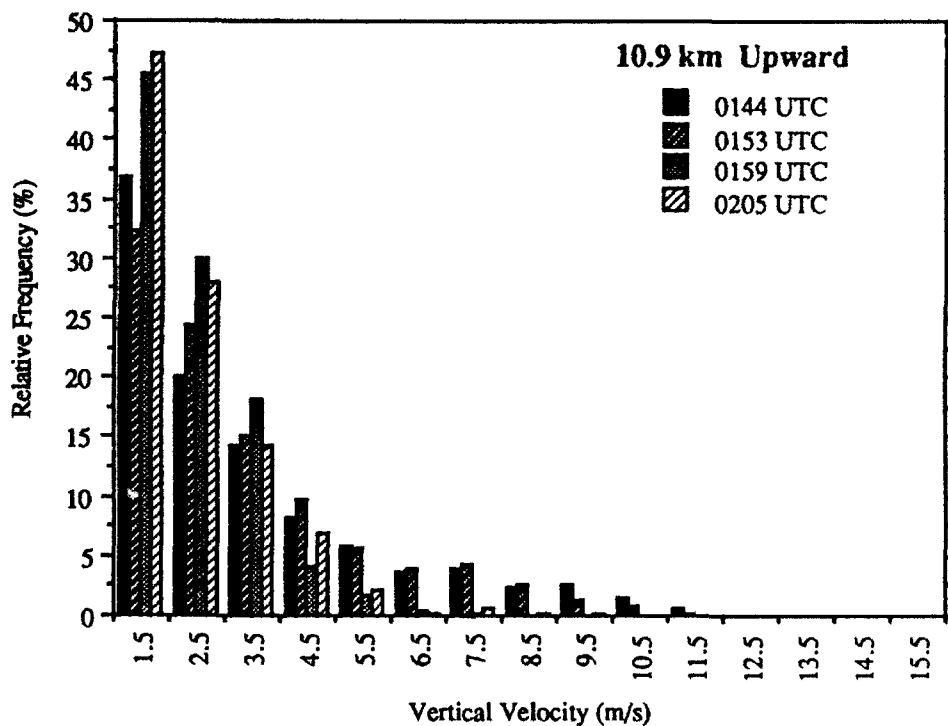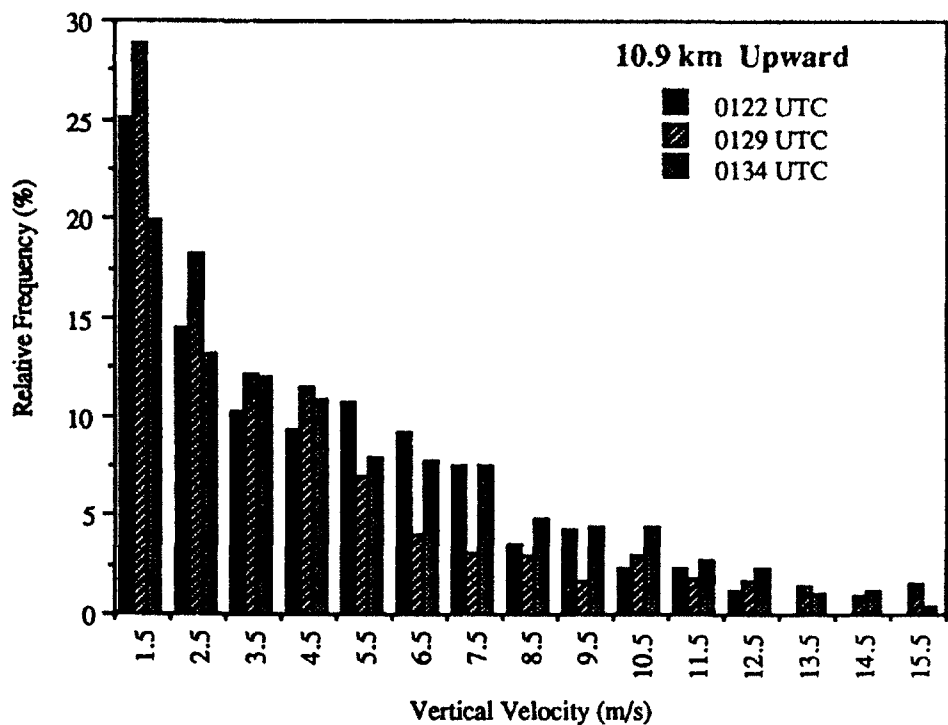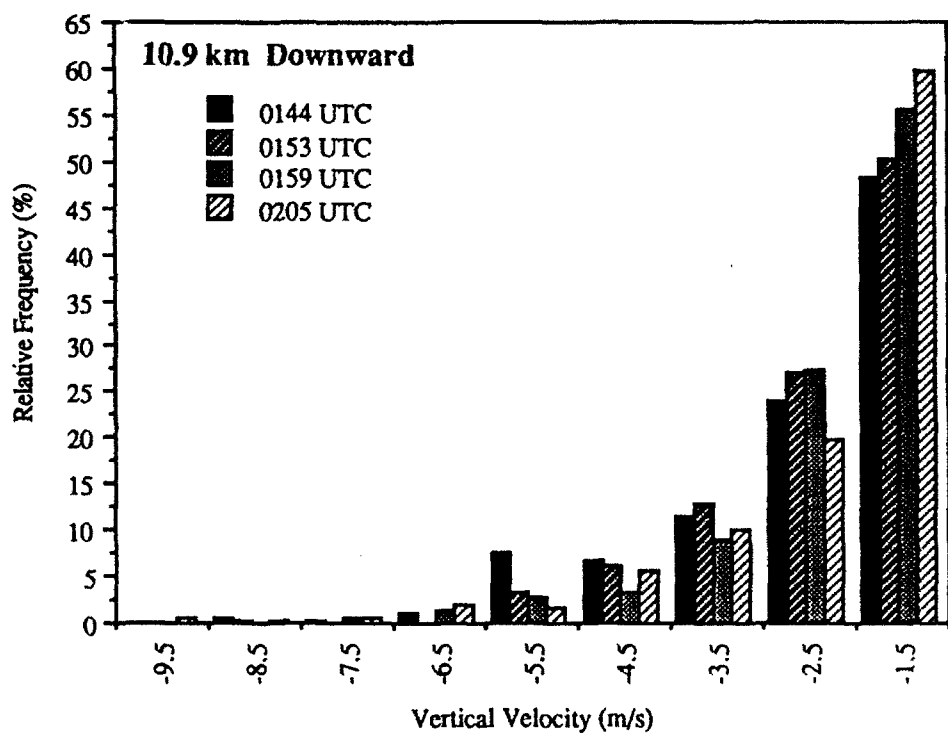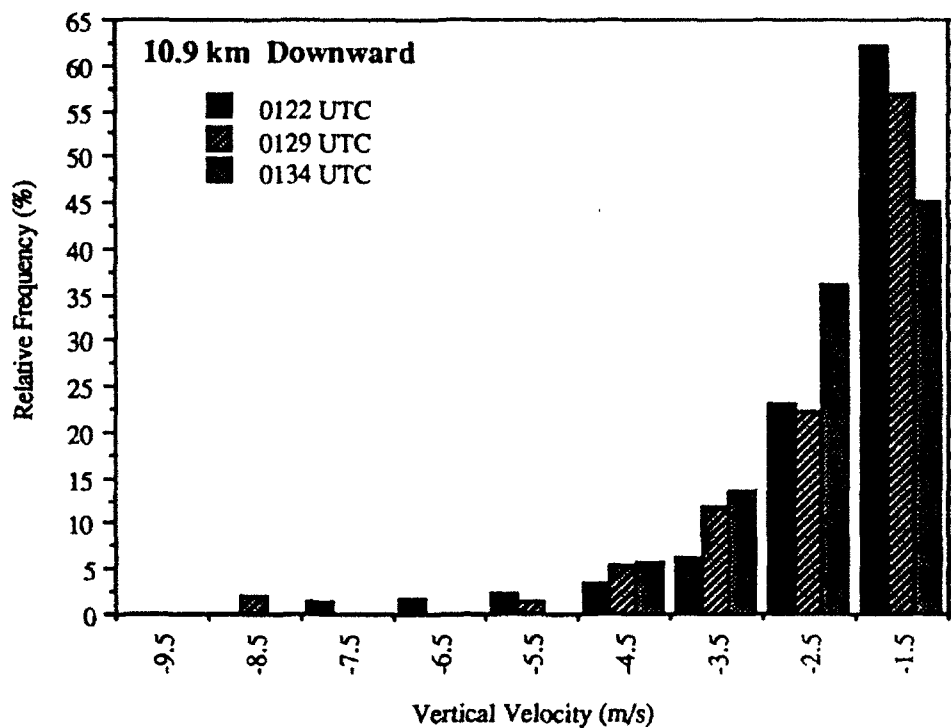
VITA

Dennis Allen Hobson was born to James and Dorothy Reames Hobson on September 23, 1959 in Cedar Rapids, Iowa. He grew up in nearby Palo, Iowa but graduated from John F. Kennedy High School in Cedar Rapids in June, 1978.

In July, 1978 he enlisted in the US Air Force and was assigned to Scott AFB, Illinois as a medical technician. Airman 1st Class Hobson was awarded an Air Force ROTC scholarship in August, 1980 and was released from active duty to attend the University of Iowa; where he graduated with a B.S. in chemistry in May, 1984. Upon graduation he received his commission in the US Air Force, and entered the Air Force Institute of Technology's Basic Meteorology Program at San Jose State University. 2nd Lieutenant Hobson was assigned to Grissom AFB, Indiana in May, 1985 as a Wing Weather Officer supporting the 305th Air Refueling Wing and the Department of Defense's National Emergency Airborne Command Post. 1st Lieutenant Hobson was reassigned in May, 1987 to Schofield Barracks, Hawaii as Officer-in-Charge of the 25th Infantry Division's Tactical Weather Team. His tenure there included various field deployments with the US Army in Hawaii, Arkansas, Japan, and the Republic of Korea. In April, 1989 Captain Hobson was transferred to Headquarters 1st Weather Wing at Hickam AFB, Hawaii as Chief of the Field Support Section, with oversight of general operations at 37 Air Weather Service field units throughout Alaska and the Pacific region. In August, 1990 he began his M.S. program in meteorology at Texas A&M University under the Air Force Institute of Technology's Advanced Academic Degree Program. In August, 1992 he was assigned to Air Force Global Weather Central at Offutt AFB, Nebraska as a Technical Staff Officer within the Meteorological Products Branch.

Captain Hobson is married to the former Amy Jo Langguth of Palo, Iowa. They have three children. His permanent address is 409 Vinton Street, Palo, Iowa 52324.